

---

# Infrared waveform synthesis for applications in attosecond science

Olga Razskazovskaya

---



München 2017



---

# **Infrared waveform synthesis for applications in attosecond science**

**Olga Razskazovskaya**

---

Dissertation  
an der Physik  
der Ludwig–Maximilians–Universität  
München

vorgelegt von  
Olga Razskazovskaya  
aus Moskau, Russland

München, den 30.10.2017

Erstgutachter: Prof. Dr. Ferenc Krausz

Zweitgutachter: Prof. Dr. Karl Unterrainer

Tag der mündlichen Prüfung: 11.12.2017

# Contents

<b>Zusammenfassung</b>	<b>ix</b>
<b>Abstract</b>	<b>xi</b>
<b>List of Publications</b>	<b>xiii</b>
<b>Introduction</b>	<b>xv</b>
<b>1 Theoretical background</b>	<b>1</b>
1.1 Introduction to nonlinear optics . . . . .	1
1.1.1 Optical parametric amplification . . . . .	2
1.1.2 Electro optic effect . . . . .	3
1.1.3 Four-wave mixing . . . . .	3
1.1.4 Self-phase modulation . . . . .	4
1.2 Multilayer thin-film coatings in a nutshell . . . . .	6
1.2.1 The Poynting vector . . . . .	8
1.2.2 Simple boundary . . . . .	8
1.2.3 Normal incidence . . . . .	9
1.2.4 Oblique incidence . . . . .	11
1.2.5 The reflectance of a thin film . . . . .	13
1.2.6 The reflectance of an assembly of thin films . . . . .	15
<b>2 Hybrid degenerate/nondegenerate phase-stable infrared optical parametric chirped pulse amplifier</b>	<b>17</b>
2.1 Introduction and motivation . . . . .	17
2.2 Concept and theoretical justification . . . . .	19
2.3 Experimental results . . . . .	20
2.3.1 State of affairs before the start of the current development . . . . .	20
2.3.2 1.3 mJ sub-two-cycle 2.1 $\mu\text{m}$ hybrid OPCPA . . . . .	21
2.4 Conclusion of Chapter 2 . . . . .	23
<b>3 Generation of a multi-octave phase-stable supercontinuum in ambient-air- or argon-filled hollow-core fiber</b>	<b>25</b>
3.1 Introduction to the topic . . . . .	25

3.2	Experimental set up and results . . . . .	26
3.2.1	The state of affairs before the start of the current work - 0.5 mJ OPCPA . . . . .	26
3.2.2	1.3 mJ OPCPA . . . . .	28
3.3	CEP-stability . . . . .	29
3.4	Conclusions and outlook of Chapter 3 . . . . .	30
<b>4</b>	<b>Advanced multilayer thin–film dielectric coatings for versatile dispersion management</b>	<b>31</b>
4.1	Introduction and historical overview . . . . .	31
4.2	Multi-octave group delay control . . . . .	33
4.3	Visible dispersive optics . . . . .	34
4.3.1	Phase compensation versus material compensation . . . . .	35
4.4	Ultraviolet dispersive optics . . . . .	37
4.4.1	Induced nonlinear effects: establishing control over induced nonlin- earities . . . . .	38
4.4.2	Experiment and Results . . . . .	39
4.4.3	The model . . . . .	44
4.4.4	Implications . . . . .	48
4.5	Infrared dispersive optics . . . . .	51
4.6	Conclusions of Chapter 4 . . . . .	53
<b>5</b>	<b>Multi–color multi-channel optical waveform synthesis</b>	<b>55</b>
5.1	Introduction . . . . .	55
5.2	Experimental set up . . . . .	56
5.2.1	Channel subdivision . . . . .	56
5.2.2	Spectral phase control in the individual channels . . . . .	58
5.3	Multi–color ultrafast source . . . . .	60
5.4	Conclusions of Chapter 5 . . . . .	63
<b>6</b>	<b>Electro–optic sampling of near–infrared and visible waveforms</b>	<b>65</b>
6.1	Introduction to the topic . . . . .	65
6.2	Experimental set up . . . . .	66
6.3	Experimental results . . . . .	68
6.4	Conclusions of the Chapter 6 . . . . .	71
	<b>Conclusions and outlook</b>	<b>72</b>
	<b>A Data archiving</b>	<b>75</b>
	<b>Danksagung</b>	<b>91</b>

# List of Figures

1	The energy density transfer. . . . .	xvii
2	Footprint of the Apparatus . . . . .	xxi
1.1	Energy-level description of the difference-frequency generation. . . . .	3
1.2	Energy-level description of the four-wave mixing processes. . . . .	4
1.3	Plane wavefront incident on a single surface. . . . .	9
1.4	Common definition conventions. . . . .	10
1.5	Convention defining the positive directions of the electric and magnetic vectors	11
1.6	The reflectance of a thin film. . . . .	13
2.1	Hybrid degenerate/nondegenerate OPCPA: simulations . . . . .	19
2.2	Hybrid degenerate/nondegenerate OPCPA: experiment . . . . .	22
2.3	OPCPA long-term stability: 30 min time slot, rms noise of $\leq 2\%$ . . . . .	22
2.4	Mode of the hybrid degenerate/nondegenerate OPCPA: oversaturated vs. nonsaturated case. . . . .	23
2.5	Spectral and temporal characterization of the novel hybrid OPCPA. . . . .	24
3.1	Generation of multi-octave supercontinua in the argon-filled HCF. . . . .	27
3.2	Supercontinuum in air. . . . .	29
3.3	Evaluation of the CEP stability of the generated supercontinuum. . . . .	30
4.1	Dichroic beam splitters for optical waveform synthesis. . . . .	33
4.2	Dispersion targets in visible range. . . . .	36
4.3	Hybrid dispersion target approach for the design of the visible and near infrared dispersive mirrors. . . . .	37
4.4	Dispersive multilayers in visible spectral range. . . . .	38
4.5	Intensity dependent reflectance of the series of the non-optimized DMs. . . . .	40
4.6	Reversibility of nonlinear response . . . . .	41
4.7	Electric field distribution at central wavelength of 400 nm, angle of incidence (AOI) = 45 deg, s-polarization in different types of the coatings . . . . .	42
4.8	Impact of different types of nonlinearities on dispersive performance of mirror M1. . . . .	43
4.9	Thermal tests of non-optimized designs. . . . .	44

4.10	Simulated intensity-dependent reflectance of the mirror M2 at different wavelengths. . . . .	46
4.11	Distributions of the induced extinction coefficient $\beta E ^2$ in the mirror M2 cross-section for wavelengths values: 390, 400, and 410 nm. . . . .	47
4.12	Optimization of 2PA in a dielectric coating. . . . .	49
4.13	TG FROG. . . . .	50
4.14	Thermal tests of 2PA-optimized design. . . . .	51
4.15	Dispersive multilayers in the infrared spectral range designed to compensate the material dispersion of 0.25 mm Si to lowest order. . . . .	52
5.1	Multi-color multi-channel ultrafast source for attosecond science. . . . .	57
5.2	Spectral coverage of the multi-color source. . . . .	58
5.3	Spectral and temporal characterization of the individual channels after the exit of the hollow-core fiber. . . . .	59
5.4	Dispersive optics of the multi-color source. . . . .	61
5.5	Spectral and temporal characterization of the CH0/EOS. . . . .	62
5.6	Spectral and temporal characterization of the individual channels after compression. . . . .	63
6.1	High-frequency broadband electro-optic sampling. . . . .	67
6.2	Electro-optic sampling of visible-near-infrared waveforms. . . . .	68
6.3	Electro-optic sampling of near-infrared waveforms. . . . .	69
6.4	Electro-optic sampling of visible-infrared waveforms. . . . .	70

# Zusammenfassung

Die optische Schaltungstechnik ist der lang erwartete Nachfolger unserer heutigen siliziumbasierten Elektronik. Das Forschungsinteresse hieran wurde durch das Aufkommen von ultrakurzen, kohärenten Lichtquellen, welche Lichtpulse aus lediglich einer einzigen Oszillation des elektrischen Feldes erzeugen können, enorm belebt. Ihre Nutzung zur Signalverarbeitung verspricht eine tausendfache Erhöhung der bisher möglichen Schaltfrequenzen. Hauptvoraussetzung für ihre Verwirklichung ist jedoch die Verfügbarkeit eines optisch aktiven Schalters oder Transistors.

Jüngste Forschungsergebnisse zeigen, dass intensive, ultrakurze Lichtfelder im Nahinfraroten die Polarisation eines Dielektrikums mit großer Bandlücke auf Zeitskalen unter einer Femtosekunde verändern können. Die zugrunde liegende optische Kopplung könnte als ultraschneller, optischer Schalter verwendet werden. Ähnliche Dynamiken in konventionellen, technologisch verwendeten Halbleitern wie InGaAs oder Silizium haben Potential die Entwicklung der optischen Schaltungstechnik maßgebend zu gestalten. Da technisch relevante Halbleiter kleine Bandlücken ( $\sim 1\text{eV}$ ) aufweisen, werden für ihre Untersuchung geringere Photonenergien, also Lichtquellen im infraroten Spektralbereich, benötigt. Um eine definierte Anregung zu erzeugen und eindeutig verfolgen zu können, werden desweiteren Lichtimpulse mit kontrollierbarer elektrischer Feldentwicklung sowie eine präzise, zur umfassenden Charakterisierung geeignete, Messtechnik benötigt.

Im Rahmen dieser Dissertation wurde eine intensive, kohärente Infrarot-Lichtquelle entwickelt, welche die benötigten kontrollierbaren Wellenformen mit konstanter Träger-Einhüllenden-Phase, sowie Pulsdauern von bis zu einer einzelnen Feldoszillation, erzeugen kann. Desweiteren wurde eine Messtechnik basierend auf elektrooptischer Abtastung, mit dessen Hilfe nunmehr die komplette Amplituden- und Phaseninformation der erzeugten optischen Feldtransienten festgestellt werden kann, etabliert.

Zur Verwirklichung einer derartigen *Lichtquelle* wurde die Impulsenergie eines existierenden optisch-parametrischen Nahinfrarotverstärkers, welcher Impulse mit weniger als zwei optischen Oszillationen bereitstellte, mittels einer neuartigen entarteten/nicht-entarteten Verstärkungsstufe bestehend aus zwei Bariumboratkristallen, von  $200\ \mu\text{J}$  auf über  $1\ \text{mJ}$  erhöht. Dieser Ansatz erlaubt eine signifikante Erhöhung der finalen Impulsenergie, ohne dabei die Verstärkungsbandbreite oder die Impulsdauer negativ zu beeinflussen. Das Spektrum der Lichtpulse wird anschließend in einer luftgefüllten Hohlkernfaser nichtlinear verbreitert um ein Superkontinuum mit kontrollierter Träger-Einhüllenden-Phase zu erzeugen. Dieses umfasst mehr als drei Oktaven, beginnend mit  $300\ \text{nm}$  und en-

dend bei über  $2.5 \mu\text{m}$ , und ermöglicht so die Generation von Feldtransienten mit Dauern unter einer optischen Oszillation. Zur vollständigen Kontrolle wird das erzeugte Spektrum in drei spektrale Kanäle aufgeteilt, welche individuell phasenkorrigiert, verzögert und kohärent rekombiniert werden.

Hochentwickelte Vielschicht-Dünnschicht-Optiken mit maßgefertigten spektralen Eigenschaften optimieren die Dispersion der Synthesizer-Kanäle. Neuartige Ansätze zum Aufbau der Dünnschicht-Optiken im ultravioletten Kanal ermöglichen die zeitliche Kompression der Impulse, welche maßgebend für die Realisation der *elektrooptischen Abtastung* ist.

Für die elektrooptische Abtastung wird eine optimierbare, aber unbekanntere Testwellenform erzeugt, welche durch die kohärente Addition des sichtbaren und des kurzwelligen Infrarot-Kanals, mit dem zuvor charakterisierten ultravioletten Hochfrequenz-Messkanal in einem elektrooptisch aktiven Kristall überlagert. Die nicht lineare Wechselwirkung rotiert die Polarisation des Messpulses proportional zur instantanen Feldstärke der Testwellenform. Durch relative Verzögerung der beiden Lichtpulse lässt sich so die gesamte Entwicklung der Testwellenform aufzeichnen. Im Rahmen dieser Arbeit wurde die Grenzfrequenz dieser Technik auf bis zu 430 THz erhöht, das entspricht einer sichtbaren Wellenlänge von 700 nm. Außerdem wurde der Weg für eine weitere Erhöhung auf 500 THz (500 nm) geebnet. Bei dieser Grenzfrequenz gilt die elektrooptische Abtastung als eine praktische Alternative zur Attosekunden-Streak-Kamera, da sie die direkte Beobachtung von nahinfraroten Wellenformen mithilfe eines kompakten Aufbaus unter Raumbedingungen ermöglicht.

Abschließend betrachtet stellt die hier vorgestellte Lichtquelle im Zusammenspiel mit der elektrooptischen Abtastung ein einzigartiges Werkzeug zur Untersuchung einer großen Zahl von potentiell relevanten Halbleitermaterialien für die zukünftige optische Schaltungstechnik dar.

# Abstract

Lightwave electronics has long been a highly anticipated rival to the conventional silicon-based electronics of our days. The interest was intensified by the advent of ultrafast coherent light sources with pulse duration lasting merely a cycle of oscillating electric field at optical frequencies. Their usage for signal processing promises a factor of 1000 increase of the processing clock rates. However, the major prerequisite for the viability of the novel concept is an existence of a light-governed switch or transistor.

A recent study showed, that an intense transient near-infrared light fields are capable of governing the polarization response of a wide band gap dielectric on a sub-femtosecond time scale, enabling optical-to-optical coupling that can be used as a switch. Observation of a similar dynamics in conventional and technologically well-developed silicon and InGaAs could be determining for the future of the light wave electronics. However, as both Si and InGaAs as well as a number of other technologically relevant semiconductors have rather modest electronic band gaps (around  $\sim 1\text{eV}$ ), sources with substantially lower photon energies - in the short-wavelength-infrared - are required for their investigations. Further more, in order to excite and study the electronic system in a well-controlled manner, we need sources with well-controlled temporal evolution of the electric field, henceforth called *waveform*, and measurement techniques that are able resolve the waveforms.

This dissertation aims at the development of the intense short-wavelength-infrared ( $\lambda_c \sim 1.8\mu\text{m}$ ) coherent light source delivering waveform-controlled carrier-phase stable nearly single cycle pulses and at the establishment of a high-frequency electro-optic sampling technique for complete amplitude and phase characterization of the produced optical waveforms.

For the development of the *light source*, an existent 200  $\mu\text{J}$  sub-two-cycle short-wavelength-infrared optical parametric amplifier is upgraded to 1 mJ pulse energy via an implementation of a novel degenerate/nondegenerate amplification scheme combined of two barium borate crystals. The approach allows to substantially scale the amplifier's pulse energy without sacrificing the amplification bandwidth and pulse duration. The amplified pulses are subsequently spectrally broadened in a hollow-core fiber filled with ambient air. Resulting carrier-phase stable supercontinuum spans over three optical octaves from 300 nm to 2.5  $\mu\text{m}$  and beyond ultimately supporting synthesis of sub-cycle optical transients. Following the concept of waveform synthesis the generated spectrum is subdivided into three spectral channels. The channels are corrected for spectral phase, temporally delayed and later coherently recombined. While the high-frequency channel is employed for the

electro-optic sampling diagnostics, the visible and short-wave-infrared channels are used for a synthesis of custom-tailored optical waveforms. Advanced multilayer thin-film dispersive optics is used for the dispersion control in the synthesizer's channels. New approach is developed for design of the thin-film components operating in the ultraviolet spectral range. Their implementation essentially allowed generation of a temporally-compressed pulse in the high-frequency channel that is vital for the operation of the electro-optic sampling diagnostics.

In *electro-optic sampling*, an unknown test waveform created by the coherent recombination of the visible and short-wavelength-infrared channels overlaps with well-characterized short sampling pulse (high frequency channel) in an electro-optic crystal. The nonlinear interaction induces a polarization rotation of the sampling pulse which is proportional to the instantaneous electric field of the test waveform. By scanning the temporal delay between the test waveform and the sampling pulse the complete evolution of the electric field of the test pulse is directly recorded. In the current work we have extended the spectral cutoff of the technique to an underrepresented 430 THz, corresponding to the wavelength of 700 nm, and potentially up to 500 THz (600 nm). With this spectral cut off, the electro-optic sampling becomes a viable alternative to the attosecond streak camera technique, enabling the direct recording of near-infrared optical waveforms in compact, ambient-air set up.

All in all, the presented light source together with the established high-frequency electro-optic sampling diagnostics is a unique tool for high-temporal resolution studies of a wide range of semiconductor materials that are potentially suitable for the future lightwave electronics.

# List of Author's publications

- **O. Razskazovskaya** and M. Ossiander, F. Siegrist, V. Pervak and M. Schultze, "Carrier frequency tuning of few-cycle light pulses by Broadband Attenuating Mirrors (BAM)", *Applied Optics*, accepted.

The author designed and produced the optical component described in the manuscript, analyzed the data and prepared the manuscript together with M.O. and M.S.

- T. Latka, V. Shirvanyan, M. Ossiander, **O. Razskazovskaya**, A. Guggenmos, M. Jobst, M. Fiess, S. Holzner, A. Sommer, M. Schultze, C. Jakubeit, J. Riemensberger, B. Bernhardt, W. Helml, F. Gatti, B. Lasorne, D. Lauvergnat, P. Decleva, G. J. Halasz, A. Vibok, R. Kienberger, "Few-Femtosecond Wave Packet Revivals in Ozone", *Nature Physics*, submitted.

The author designed and produced an optical component that enabled the experiment described in the manuscript, revised and discussed the manuscript.

- Rivas, D. E. and Borot, A., Cardenas, D. E., Marcus, G., Gu, X., Herrmann, D., Xu, J., Tan, J., Kormin, D., Ma, G., Dallari, W., Tsakiris, G. D., Földes, I. B., Chou, S.-w., Weidman, M., Bergues, B., Wittmann, T., Schröder, H., Tzallas, P., Charalambidis, D., **Razskazovskaya, O.**, Pervak, V., Krausz, F. and Veisz, L, "Next Generation Driver for Attosecond and Laser-plasma Physics", *Scientific Reports* 7, 1 (2017).

The author designed and produced optical components that were implemented in the experiment, revised and discussed the manuscript.

- **O. Razskazovskaya**, F. Krausz, and V. Pervak, "Multilayer coatings for femto- and attosecond technology," *Optica* 4, 129 (2017).

The author designed, produced and implemented the optical components described in the manuscript, analyzed the data and prepared the manuscript together with F.K. and V.P.

- **O. Razskazovskaya**, M. T. Hassan, T. Luu, E. Goulielmakis, and V. Pervak, "Efficient broadband highly dispersive HfO<sub>2</sub>/SiO<sub>2</sub> multilayer mirror for pulse compression in near ultraviolet," *Optics Express* 24, 13628 (2016).

The author designed and produced the optical components described in the manuscript, analyzed data and prepared the manuscript with M.H. and T.L.

- A. Sommer, E. M. Bothschafter, S. A. Sato, C. Jakubeit, T. Latka, **O. Razskazovskaya**, H. Fattahi, M. Jobst, W. Schweinberger, V. Shirvanyan, V. S. Yakovlev, R. Kienberger, K. Yabana, N. Karpowicz, M. Schultze, and F. Krausz, "Attosecond nonlinear polarization and light-matter energy transfer in solids," *Nature* 534, 86–90 (2016).

The author designed and produced optical components that enabled the experiment, revised and discussed the manuscript.

- M. T. Hassan, T. T. Luu, A. Moulet, **O. Razskazovskaya**, P. Zhokhov, M. Garg, N. Karpowicz, A. M. Zheltikov, V. Pervak, F. Krausz, and E. Goulielmakis, "Optical attosecond pulses and tracking the nonlinear response of bound electrons," *Nature* 530, 66–70 (2016).

The author designed and produced optical components that enabled the experiment, revised and discussed the manuscript.

- **O. Razskazovskaya** and T. T. Luu, M. Trubetskov, E. Goulielmakis, and V. Pervak, "Nonlinear absorbance in dielectric multilayers," *Optica* 2, 803 (2015).

The author designed, produced and implemented the optical components described in the manuscript, analyzed the data and prepared the manuscript together with T.T.L.

- **O. Razskazovskaya**, T. T. Luu, M. K. Trubetskov, E. Goulielmakis, and V. Pervak, "Nonlinear behavior and damage of dispersive multilayer optical coatings induced by two-photon absorption," (2014), SPIE Proceedings p. 92370L.

The author designed, produced and implemented the optical components described in the manuscript, analyzed the data and prepared the manuscript together with T.T.L.

- T. Paasch-Colberg, A. Schiffrin, N. Karpowicz, S. Kruchinin, Saglam, S. Keiber, **O. Razskazovskaya**, S. Mühlbrandt, A. Alnaser, M. Kübel, V. Apalkov, D. Gerster, J. Reichert, T. Wittmann, J. V. Barth, M. I. Stockman, R. Ernstorfer, V. S. Yakovlev, R. Kienberger, and F. Krausz, "Solid-state lightphase detector," *Nature Photonics* 8, 214–218 (2014).

The author designed and produced optical components that were implemented in the experiment, revised and discussed the manuscript.

- V. Pervak, **O. Razskazovskaya**, I. B. Angelov, K. L. Vodopyanov, and M. Trubetskov, "Dispersive mirror technology for ultrafast lasers in the range 220–4500 nm," *Advanced Optical Technologies* 3 (2014).

The author designed, produced and implemented the optical components described in the manuscript, analyzed the data and prepared the manuscript together with V.P.

- T. V. Amotchkina, M. K. Trubetskov, A. V. Tikhonravov, V. Janicki, J. Sancho-Parramon, **O. Razskazovskaya**, and V. Pervak, "Oscillations in spectral behavior of total losses ( $1 - R - T$ ) in thin dielectric films," *Optics express* 20, 16129–16144 (2012).

The author has performed the measurements used in the manuscript, revised and discussed the manuscript.

- Pervak, V., Pronin, O., **Razskazovskaya, O.**, Brons, J., Angelov, I. B., Trubetskov, M. K., Tikhonravov, A. V. and Krausz, F., "High-dispersive mirrors for high power applications," *Optics express* 20, 4503–4508 (2012).

The author has performed the measurements used in the manuscript, revised and discussed the manuscript.

# Introduction

Light is used throughout the living world to convey and transmit messages. Deep sea creatures communicate using particular light patterns [1] the same way, as humanity from the beginning of civilization used signaling towers and light houses to rapidly pass on vital information over vast distances. Light still remains our major means of communication, with optical fiber links crossing continents and ocean floor striving to keep the world connected. However, there is an ambitious dream to utilize the speed and the unique properties of light not only for a transport of information, but for a signal processing itself [2, 3]. Will it ever be possible?

Introduction of the first germanium- and then silicon-based integrated circuits in 1958 [4] was undoubtedly one of the major technological advances of the twentieth century leading to the invention of the microprocessor (microchip), and consequently, revolutionizing the world of electronics and propelling to a new level science, technology, industry and, no less important, our daily lives. For the past 50 years microchip performance was rapidly improving with processing power doubling approximately every 18 months. It became possible due to the steady decrease in size of the individual transistors (following the Moore's law [5], the amount of transistors per microchip doubles every two years for the last 40 years) and the transistors becoming faster.

Logically, the trend can not continue into infinity. Already in 2010 it was predicted that the growth would slow down and in 2015 Moore himself projected, that the law will reach saturation and eventually extinct by the end of the next decade. It is mostly connected to the major technological limitation to the transistor sizes that can be possibly manufactured and the microchip architecture used under current paradigm.

The invention of the deep ultraviolet photolithography in 1980 enabled the manufacturing of transistors with dimensions below the diffraction limit of the UV light. It allowed to shrink down the size of the individual transistor from 800 nm transverse width (the status quo as of 1990) to ultimately 10 nm width: in 2012 Intel has released a microchip featuring a 22 nm width; yet, in 2015 they reported on a deceleration of the advances from the projected two-year rule with 14 nm transistor to be released and 10 nm width to be reached by late 2017. The multi-core approach is used instead to boost the processing power.

A further decrease of the spatial dimensions of the devices below 10 nm is possible with a transfer to the extreme ultraviolet lithography ( $\lambda \approx 13$  nm). In 2015, IBM demonstrated first node chips with 7 nm silicon-germanium transistors produced using this method [4].

Later in 2016 Intel has also speculated of a transfer to 7 nm, and forecast the shift towards 5 nm technology and beyond in future. However, although the size of the individual transistor seemingly did not reach the final *technological* limit yet, there are major *fundamental physical* constraints in the current type of transistor and microchip architectures.

First of them is connected to the thermal stability of the circuit. With the size of the transistor scaling down, it became possible to put more and more transistors on the same microchip. The transistor's switching is engaged by the external voltage that creates a conductive channel and activates carriers flow across the transistor. Opening the gate creates heat. For the stable operation of the device this heat needs to be efficiently dissipated. It is possible by either putting fewer transistors per chip or by decreasing the required driving fields in order to emit less heat overall. For sub-5 nm feature widths at increased packing density, the switching energy should be so low that it becomes comparable to the thermal fluctuations at 300 K. Therefore, thermally induced leakages start to come into play, jeopardizing the circuits performance and stability.

The second major constraint is defined by quantum mechanical effects. The physical size of the silicon atoms - the building blocks of the contemporary electronics - is  $\approx 0.3$  nm, therefore the 5 nm wide transistor can be essentially composed of 17 atoms and in this case the whole arrangement should be also considered in a quantum-mechanical way. When doing so we have to acknowledge that there is a non-zero probability of tunneling either within the regions of the same transistor (leakage) as well as between the different transistors on the densely packed microchip (cross-talk). Both effects cause circuit instability.

Many current efforts to circumvent the known limitations concentrate on the development of alternative transistor architectures, including single-electron or single-atom transistors, as well as in implementation of alternative materials. InGaAs has slowly come into a spotlight for the transistor applications, while more exotic graphene-based components create some new excitement in the field. On the other hand there is another ambitious idea. If the fundamental limitations of the present paradigm are essentially set by the fact that the current electronics is "electronic" in heart, can we abandon the paradigm as whole?

The concept of a lightwave electronics comes as a rival to the silicon-based technology of our days. Its ultimate speed potentially makes light-based signal processing superior to the conventional electronic schemes. Yet, following the analogy with conventional electronics, a full-scale all-optical logics has to be developed in order to enable the all-optical computing and to fully exercise the benefits of light, meaning that the furthest prerequisite is the existence of the optical "transistor". There are several significant advances in the development of optical switches. Strong optical near infrared fields can be used for a direct generation and direction of photocurrents in semiconductors [6, 7, 8, 9] and, recently, dielectrics [10, 11], thus enabling a direct analogy to the conventional transistors. However, generation of the significant amount of free carriers equals to an appearance of the excess heat and eventually to a damage of the medium and, therefore, this optical-to-electronic coupling has very limited if any advantages.

An alternative mechanism is a pure optical-to-optical coupling. In this case, the strong

field causes the modification of the electronic structure of the medium postulating itself in the change of the nonlinear refractive index that will act as a switch. Along these lines, a recent work [12] showed that an intense near infrared field triggers a dual dynamics in silica, Fig. 1. The nonlinear response to the field comprises an ultrafast sub-femtosecond (fs) reversible contribution that can be used for signal processing and a much slower post-pulse dynamics that determines the amount of dissipated heat (red, purple and light blue lines). Below a certain field strength (dark blue), the slower dynamics becomes no longer detectable, indicating near dissipation-free operation and, thus, pure optical-to-optical coupling. This type of coupling gives an opportunity to make the full advantage of both: the ultimate speed of light and the ultrafast dynamics of the broad band gap dielectrics, thus, eventually enabling PHz clock rates.

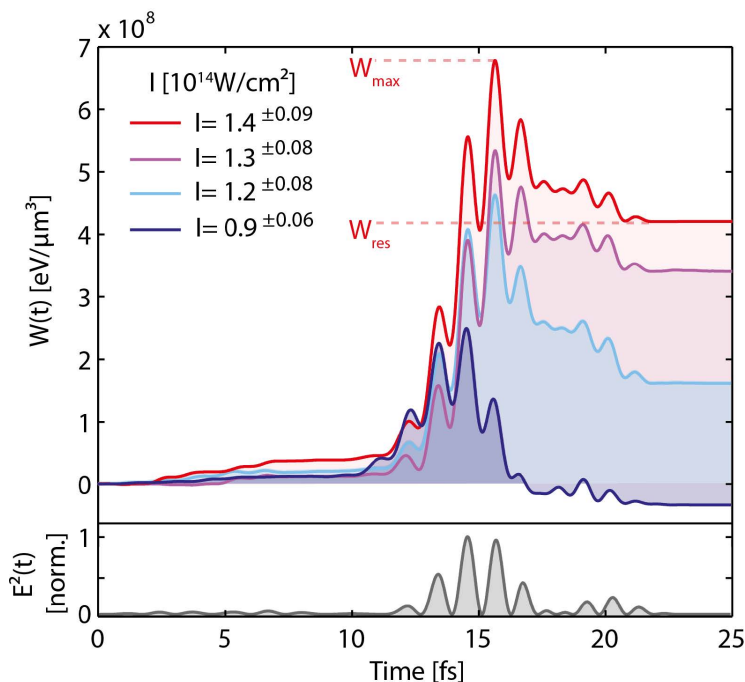


Figure 1: The energy density transferred between the material and the driving field for different peak intensities of the electric wave (increasing from dark blue, light blue, purple to red). The square of the electric field is indicated in the bottom panel (gray line), [13]

An observation of a similar dynamics in conventional semiconductors such as silicon and InGaAs could potentially deliver a new paradigm to the 335\$ billion semiconductor industry. However, as Si and InGaAs have rather modest band gaps (1.1 eV and 0.6 eV), there investigation with near infrared fields ( 1.55 eV) is problematic. Light sources with substantially lower photon energies corresponding to the lasing wavelengths in the infrared around  $\approx 2 \mu\text{m}$  are required. In addition, as the electronic dynamics in scope is expected to evolve on the sub-fs to few-fs timescales, the potential work horses have to be ultrafast.

Ultrafast optics and technology has rapidly evolved since the first 0.1 ps pulses were first achieved by colliding pulse mode-locking in dye lasers [14, 15, 16, 17, 18]. A decade

later, dyes were replaced by Kerr-lens-mode-locked Ti:Sapphire lasers that operate by finely balancing self-phase modulation, group-velocity dispersion, saturable absorption, and saturable gain [19, 20]. In another decade, the progress of the Ti:Sapphire-based systems [21, 22, 23, 24, 25, 26, 27, 28] complimented by the discovery of a nonlinear pulse compression [29, 30] and implementation of the broadband aperiodic dispersive multilayer mirrors [31, 32] has allowed to routinely generate intense near single-cycle few-fs pulses at a central wavelength of  $\approx 800$  nm [33, 34, 35]. In turn, those sources enabled generation of a train of and isolated attosecond pulses [36, 37, 38] that for the first time permitted a direct observation of electronic processes in gases [39], solids [40] and molecules [41], thus, marking the birth of an attosecond science [42, 3].

Meanwhile, a plethora of biological [43], environmental [44, 45], medical [43] and now solid-state physics applications actually demands ultrafast, preferably few-cycle, intense light sources with the emission central wavelengths in the infrared spectral range. Those are still non-trivial. In the lack of relatively-intense ultrafast infrared oscillators, the access to the emission wavelength in the infrared lies through the selection of difference frequency generation processes with subsequent amplification in one or several optical parametric amplification (OPA) stages [46]. Yet, due to the phase matching limitations of the OPA amplifying media, nearly one-cycle let alone sub-cycle pulses are challenging to achieve. A traditional way for a further spectral bandwidths expansion is a nonlinear pulse compression that was already mentioned above. Despite being pioneered for the near infrared pulses, the concept is transferable and successful at other wavelengths as well, allowing to generate multi-octave spectra spanning from the ultraviolet to the infrared [47, 48, 49].

In order to reach the ultimate pulse durations supported by these formidable spectra, their chromatic dispersion has to be carefully balanced (manipulated) that is, as well, a tremendous challenge. Over the last two decades several major techniques for a control of the spectral phase of broadband spectra were developed [50, 51, 52]. One of the most prominent and most used is the implementation of the broadband dispersive multilayer mirrors [31, 53]. Despite the enormous progress reached in the design [54, 55, 32], production, characterization and implementation of the dispersive mirrors over last twenty years, the technology is not almighty. Management of spectra exceeding 1,5 optical octaves is troublesome due to major physical and technological limitations.

An alternative pathway for a control over multi-octave spectra relies on the concept of multi-channel optical waveform synthesis [56, 57, 58, 59, 60, 61]. Under this mode, the generated ultra broadband spectrum is split into several narrower spectra - channels. The channels are individually treated for dispersion, carrier-envelope phase (CEP) control, as well as delay - and later coherently recombined. Apart from a synthesis of a sub-optical-cycle pulses, this concept enables genesis of non-sinusoidal electric field waveforms enabling a sub-cycle control over the evolution of a dynamics under examination. Meanwhile, channels can also be used independently, acting in this case, as a multi-color ultrafast pump-probe spectroscopic tool.

Aside from the synthesis of those waveforms, their temporal characterization is as well a demanding task. Several techniques for a temporal characterization of few-cycle pulses have

been developed [62, 63, 64]. Unfortunately, most of them are not without drawbacks. One of the major shortcomings is a necessity for a pulse reconstruction algorithm that often yields ambiguous results. In addition, those techniques enable recording and reconstruction of the envelope of the ultrafast pulse only leaving out the information about the exact shape of the electric field under the envelope, the information that is of a crucial importance in application to attosecond physics. The attosecond streak camera technique [65, 66] was specially designed to enable recording of the exact shape of the electric field under the envelope and is nowadays commonly in place. However, it requires an elaborate and spacious vacuum apparatus to operate. The electro-optic sampling technique [67, 68] is well known in the THz community and has recently been successfully adapted to probe the infrared waveforms [69]. Similar to the attosecond streak camera, it allows direct access to the information about the evolution of the electric field, while at the same time it doesn't need a vacuum beamline and has a maximum 20 cm x 20 cm footprint. On the down side, it requires a broadband dispersion compensated probe pulse covering the spectral range adjacent to the investigated spectral range on the shorter wavelength side. Visible few-fs probe pulses were used to sample a near infrared spectral range down to 1.2  $\mu\text{m}$  [69]. Hence, probing wavelengths in visible will require a usage of a broadband compressed few-fs pulse in near ultraviolet, which is a daunting venture on its own.

This work is devoted to the development and characterization of an intense ultrafast versatile three-channel, multi-color infrared waveform synthesizer covering spectral range from  $\sim 300$  nm to 2.7  $\mu\text{m}$  to be used in endeavor of having a new glimpse into a carrier dynamics of a broad class of dielectric and semiconductor materials potentially suitable for the future lightwave electronics.

Fig. 2 presents the footprint of the developed apparatus, visually matching the different elements of the set up to the chapters of the present thesis. Over the course of the work the reader will be guided step-by-step through the sections of the apparatus, (hopefully) coherently building the complete story.

Chapter 1 (not depicted in Fig. 2) provides a brief tour through the theoretical background covering the phenomena of nonlinear optics exploited in this work. Optical parametric amplification, nonlinear pulse compression of mJ-level pulses via self-phase modulation in noble-gas-filled hollow-core fibers (HCF) and electro-optic (EOS) sampling will be discussed. The chapter also introduces, in a nutshell, basic principles of thin-film multilayer coatings and in particular the concept of dispersive multilayer mirrors.

Chapter 2 discusses the development of the optical parametric amplification stage that became a source of intense sub-two-cycle pulses centered at a central wavelength of  $\sim 2.1$   $\mu\text{m}$  that were used to generate the synthesizer's spectrum. The subsection 2.3.1 describes the state of affairs before the start of the project.

Chapter 3 unwraps in fine details the generation and characterization of the multi-octave spectrum spanning from the ultraviolet to infrared that is consequently used for the waveform synthesis and diagnostics.

Chapter 4 introduces in thorough detail design, production and implementation of the advanced multilayer optics that essentially facilitates the operation of the whole apparatus. Subsection 4.5 is in particular devoted to the problems arising in the development of a

broadband ultraviolet optics that are a prerequisite for the electro-optic sampling tool.

Chapter 5 is devoted to the development of the synthesizer apparatus itself including but not limited to mechanical design, compression of the individual channels and their characterization.

Chapter 6 presents the concept and an experimental set up of an high-frequency broadband electro-optic sampling apparatus that for the first time enables to use this method, otherwise well-known in the THz community, for the direct access to the electric field of the visible and near infrared waveforms. The characterization of the combined synthesizer channels is presented.

Finally, the results are summarized up and examined in Conclusions.

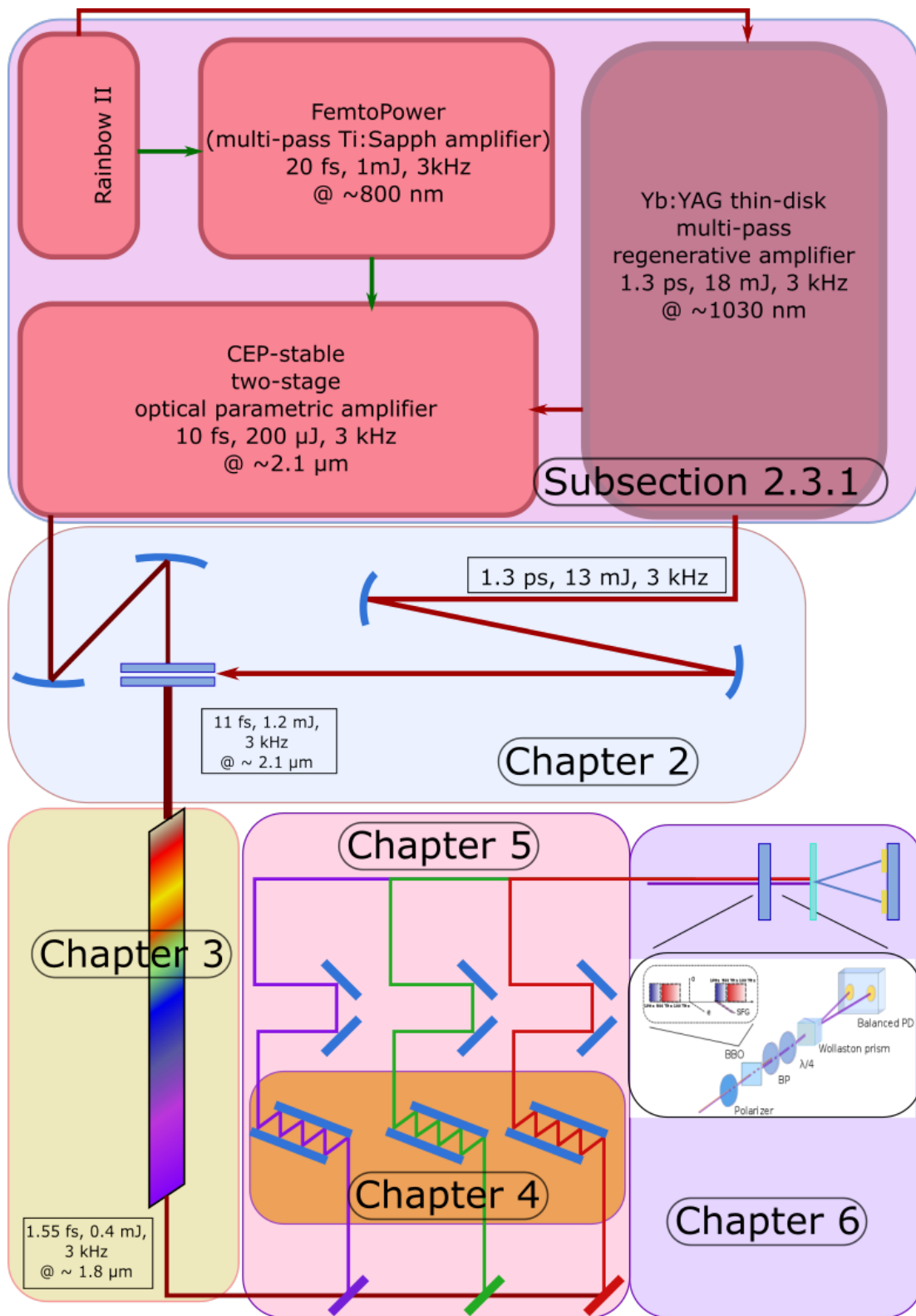


Figure 2: Schematic overview of the developed apparatus.



# Chapter 1

## Theoretical background

The present chapter briefly introduces theory underneath pivotal physical concepts exploited in the current thesis.

### 1.1 Introduction to nonlinear optics

Nonlinear optics studies interaction of intense light with matter. Typically only laser light is intense enough to trigger nonlinear phenomena. The field began shortly after T. Maiman's invention of the first laser [70] with observation of second-harmonic generation by P. Franken and co-workers [71]. And in 1962 a solid theoretical foundation underneath was first laid in the monogram of Nicholas Bloembergen [72]. For a thorough and insightful overview of the field please refer to an excellent classical textbook by Robert W. Boyd on nonlinear optics [73] or to no less excellent lectures of Dr. Vladislav Yakovlev of Ludwig-Maximilians-University, Munich. The following sections cover only in brief the basics of the processes in scope.

When applied intense light field is not too large to cross the border into strong-field phenomena [42], matter's response to the field is governed by the form of the dipole moment per unit volume, or polarization density  $\tilde{P}(t)$  at a time  $t$ . It can be expressed by a Taylor expansion in terms proportional to the applied electric field strength  $\tilde{E}(t)$ . For simplicity let's assume that  $\tilde{P}(t)$  and  $\tilde{E}(t)$  are scalar for the moment. Then the polarization density can be expressed as:

$$\tilde{P}(t) = \chi^{(1)}\tilde{E}(t) + \chi^{(2)}\tilde{E}^2(t) + \chi^{(3)}\tilde{E}^3(t) + \dots \equiv \tilde{P}^{(1)}(t) + \tilde{P}^{(2)}(t) + \tilde{P}^{(3)}(t) + \dots \quad (1.1)$$

where  $\chi^{(n)}$  is n-th order susceptibility of the medium representing both the polarization-dependent nature of the parametric interaction and the symmetries (or lack of) of the nonlinear material. In general  $\chi^{(n)}$  is a  $(n + 1)$ -rank tensor. Eq. 1.1 assumes that the response is instantaneous implying that the medium must be lossless and dispersionless.

The optical interactions of the most interest in the present work are the particular manifestations of the second- and third-order nonlinear processes described by the nonlinear

polarizations  $\tilde{P}^{(2)} = \chi^2 \tilde{E}^2(t)$  and  $\tilde{P}^{(3)} = \chi^3 \tilde{E}^3(t)$ . Electric field  $\tilde{E}(t)$  can be represented as:

$$\tilde{E}(t) = \widetilde{E}(t)e^{-i\omega t} + c.c. \quad (1.2)$$

where  $E$  is an amplitude of the electric field and *c.c.* is a complex conjugate.

### 1.1.1 Optical parametric amplification

Lets turn to the circumstances in which the electric field incident upon a nonlinear optical medium with a nonzero second-order nonlinear susceptibility  $\chi^{(2)}$  contains two distinct frequency components  $\tilde{E}_1(t)$  and  $\tilde{E}_2(t)$  each of which can be represented in the form of Eq. 1.2. The incident electric field takes the form of:

$$E(t) = \tilde{E}_1(t) + \tilde{E}_2(t) + c.c. \quad (1.3)$$

In this case the second-order nonlinear polarization  $\tilde{P}^{(2)} = \chi^2 \tilde{E}^2(t)$  can be re-written as:

$$P^{(2)}(t) = \chi^{(2)} [\widetilde{E}_1^2 e^{-2i\omega_1 t} + \widetilde{E}_2^2 e^{-2i\omega_2 t} + 2\widetilde{E}_1 \widetilde{E}_2 e^{-i(\omega_1 + \omega_2)t} + 2\widetilde{E}_1 \widetilde{E}_2^* e^{-i(\omega_1 - \omega_2)t} + c.c.] + 2\chi^{(2)} [\widetilde{E}_1 \widetilde{E}_1^* + \widetilde{E}_2 \widetilde{E}_2^*]. \quad (1.4)$$

The complex amplitude of the frequency component given by the

$$\tilde{P}(\omega_1 - \omega_2) = 2\chi^{(2)} \widetilde{E}_1 \widetilde{E}_2^* \quad (1.5)$$

describes a physical process called difference-frequency generation or DFG. Looking at the form of the complex amplitude it is rather intuitive to draw a photon energy-level diagram of the process, Fig. 1.1. From it it becomes clear that a conservation of energy requires that for each photon of the difference frequency  $\omega_3$  a photon at the higher input frequency  $\omega_1$  must be destroyed and the photon of the lower input frequency  $\omega_2$  must be created. In case when field  $\omega_2$  is already present, it will be amplified by the process. Consequently, the process of difference-frequency generation can also result in optical parametric amplification. Under this notation, the  $\omega_1$  is called pump wavelength, while  $\omega_2$  and  $\omega_3$  are accordingly signal and idler wavelengths.

In addition to the energy conservation, momentum has to be conserved as well, that is

$$\vec{k}_3 = \vec{k}_1 + \vec{k}_2 \quad (1.6)$$

where  $k$  is a quantity well known as a wave vector. However, the condition of Eq. 1.6 is in practice difficult to fulfill for a finite bandwidth, hence there is a residual momentum or phase mismatch

$$\vec{\Delta k} = \vec{k}_1 + \vec{k}_2 - \vec{k}_3. \quad (1.7)$$

Minimization of the phase mismatch is of major importance for achieving efficient and broadband amplification needed to support few-cycle optical pulses. Yet, the broadest

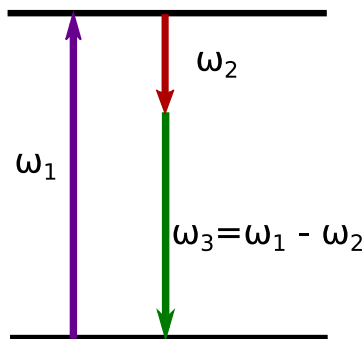


Figure 1.1: Energy-level description of the difference-frequency generation.

amplification bandwidths of an individual medium possible may barely reach an optical octave. In the following chapter we suggest a novel approach to extend the overall amplification bandwidth by combining several amplifying media pumped simultaneously by the common source.

### 1.1.2 Electro optic effect

In the case when one of the incident fields is a static or slowly varying, i.e.  $E(0)$ , the third and fourth terms on the right-hand side of the Eq. 1.4 reduce to:

$$P(w) = 2\chi^{(2)}E(w)E(0). \quad (1.8)$$

This term describes a contribution to the nonlinear polarization that appears in the presence of a static electric field, is at the frequency of the incident wave and is linearly proportional to the applied electric field. This contribution is known as the linear electrooptic, or Pockels, effect. It causes a change in the material refractive index that is linearly proportional to the field. If the change appears along one crystal axis or is unequal between the axes, the electrooptic effect induces birefringence causing phase retardation that can be expressed as

$$\Gamma = (n_x - n_y) \frac{wL}{c} \quad (1.9)$$

where  $n_x$  and  $n_y$  are the refractive indices along orthogonal crystal axes.

Phase retardation changes polarization state of the transmitted light that can be recorded in polarimeter.

### 1.1.3 Four-wave mixing

The next processes of interest in the current work are some of the third order nonlinear phenomena. The third order nonlinear response can generally be expressed as  $P^{(3)} = \chi^{(3)}E^3(t)$ . In the most general case the applied electric field should comprises three distinct frequency components, thus looking like:

$$E(t) = E_1(t) + E_2(t) + E_3(t) + c.c.. \quad (1.10)$$

If one wishes to calculate the  $\widetilde{P}^{(3)}$  through the  $\widetilde{E}^3(t)$ , it will contain 44 different frequency components. Explicitly some of these frequencies are  $3w_1, 3w_2, 3w_3, (w_1 + w_2 + w_3), (w_1 + w_2 - w_3), (w_1 - w_2 + w_3), (-w_1 + w_2 + w_3) \dots$  and so on (refer to the [73] for the full list). The complex amplitudes of the nonlinear polarization will take form :

$$\tilde{P}(3w_1) = \chi^{(3)} \tilde{E}_1^3, \tilde{P}(3w_2) = \chi^{(3)} \tilde{E}_2^3, P(3w_3) = \chi^{(3)} \tilde{E}_3^3,$$

and describe third harmonic generation at the frequencies  $w_1, w_2$  and  $w_3$ .

While the over frequency components of the nonlinear polarization will look like :

$$\begin{aligned} \tilde{P}(w_1 + w_2 + w_3) &= 6\chi^{(3)} \tilde{E}_2 \tilde{E}_3, & \tilde{P}(w_1 + w_2 - w_3) &= 6\chi^{(3)} \tilde{E}_2 \tilde{E}_3^*, \\ \tilde{P}(w_1 - w_2 + w_3) &= 6\chi^{(3)} \tilde{E}_1 \tilde{E}_2^* \tilde{E}_3, & \tilde{P}(-w_1 - w_2 + w_3) &= 6\chi^{(3)} \tilde{E}_1^* \tilde{E}_2 \tilde{E}_3, \dots \end{aligned}$$

Due to the fact that three frequencies are involved to create the fourth one, these processes are jointly called four-wave mixing. It is as well intuitive to draw the photon-energy level diagrams for third harmonic generation and four-wave mixing, Fig. 1.2 .

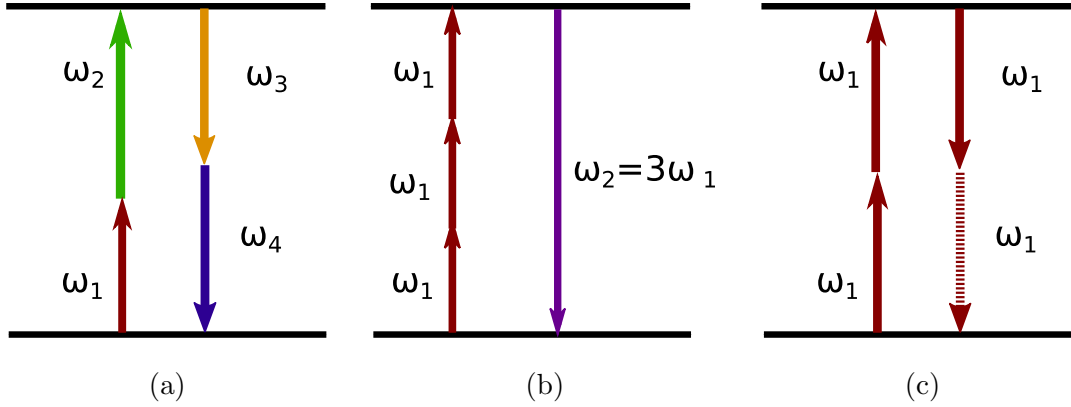


Figure 1.2: Energy-level description of the four-wave mixing processes. (a) General case of FWM; (b) third harmonic generation; (c) self-phase modulation.

### 1.1.4 Self-phase modulation

If the applied electric field consists of three fields of the same frequency  $w_0$ , the whole family of frequency mixings reduces to only two contributions to the third-order nonlinear polarization:

$$\tilde{P}(3w_0) \propto \chi^{(3)} \tilde{E}_0^3, \quad (1.11)$$

$$\tilde{P}(w_0) \propto \chi^{(3)} \tilde{E}_0 \tilde{E}_0^* \tilde{E}_0. \quad (1.12)$$

Eq. 1.12 describes a nonlinear contribution to the polarization at the frequency of the incident light and can be as well intuitively illustrated by the photon-energy level diagram, Fig. 1.2c. This term leads to an appearance of a nonlinear addition to the refractive index experienced by the wave at the frequency  $\omega_0$ .

In the presence of this kind of nonlinear response the refractive index can be described as

$$n = n_0 + n_2 I, \quad (1.13)$$

where  $n_0$  is a linear refractive index,  $I$  is a time-averaged intensity of the optical field given by

$$I = \frac{n_0 c}{2\pi} |E(\omega_0)|^2 \quad (1.14)$$

and  $n_2$  is an optical constant that gives a rate at which the refractive index increases with increasing optical intensity and can be related to  $\chi^{(3)}$  as

$$n_2 = \frac{12\pi^2}{n_0^2 c} \chi^{(3)}. \quad (1.15)$$

Using the well-known equation for the phase of the light field  $\phi = n\omega/c$  and introducing the time dependence into  $I$ , we find that the nonlinear component of the phase per unit length ( $L$ ) can be expressed as

$$\phi_{NL}(t) = -\frac{n_2 \omega_0 L}{c} I(t). \quad (1.16)$$

As a result of a time-varying phase, the spectrum will be modified and typically will get broader than that of the incident pulse. It is common to describe the spectral content of the transmitted light introducing the concept of instantaneous frequency  $\omega(t)$  of the pulse in the form of

$$\omega(t) = \omega_0 + \delta\omega(t) \quad (1.17)$$

where  $\delta\omega(t)$  is a variation of the instantaneous frequency describing the spectral broadening and can be then expressed as

$$\delta\omega(t) = \frac{d}{dt} \phi_{NL}(t) \quad (1.18)$$

When  $t$  approaches pulsed duration  $\tau_0$ , the shift of the instantaneous frequency reaches its maximum value

$$\delta\omega_{max} = \frac{\Delta\phi_{NL}^{max}}{\tau_0} \quad (1.19)$$

where

$$\Delta\phi_{NL}^{max} \simeq n_2 \frac{\omega_0}{c} I_0 L. \quad (1.20)$$

Spectral broadening due to self-phase modulation is considered to be significant whenever the change of instantaneous frequency  $\delta\omega_{max}$  is greater than the spectral width of the incident pulse, which is when  $\Delta\phi_{NL}^{max} \geq 2\pi$ .

Self-phase modulation and four-wave mixing are the major driving nonlinearities behind the spectral broadening of intense mJ-level few-cycle pulses in noble-gas-filled hollow core waveguides and filaments.

## 1.2 Multilayer thin–film coatings in a nutshell

The next section is an account of some basic theory that is necessary for understanding the principles of multilayer thin-film coatings. It is largely adopted from another classical textbook “Thin-film optical filters” by H. A. MacLeod [74].

As is commonly the case, the fundamental equations needed for calculation of thin-film properties are direct consequences of Maxwell’s equations. For an isotropic media those are:

$$\nabla \bullet \vec{D} = \rho \quad (1.21)$$

$$\nabla \bullet \vec{B} = 0 \quad (1.22)$$

$$\nabla \times \vec{H} = \vec{j} + \frac{\partial \vec{D}}{\partial t} \quad (1.23)$$

$$\nabla \times \vec{E} = -\frac{\partial \vec{B}}{\partial t} \quad (1.24)$$

$$\vec{j} = \sigma \vec{E} \quad (1.25)$$

$$\vec{D} = \varepsilon \vec{E} \quad (1.26)$$

$$\vec{B} = \mu \vec{H} \quad (1.27)$$

where  $\vec{E}$  - electric field strength,  $\vec{H}$  - magnetic field strength,  $\vec{D}$  - electric displacement,  $\vec{B}$  - magnetic induction - all are vector quantities.  $\rho$  - electric charge density,  $\sigma$  - electric conductivity,  $\mu$  - permeability,  $\varepsilon$  - permittivity.

Permittivity  $\varepsilon$  and permeability  $\mu$  can be expressed through those quantities for the vacuum.

$$\varepsilon = \varepsilon_r \varepsilon_0 \quad (1.28)$$

$$\mu = \mu_r \mu_0 \quad (1.29)$$

$$c^2 = 1/\varepsilon_0 \mu_0 \quad (1.30)$$

where  $\varepsilon_0, \mu_0$  - are permittivity and permeability of the free space,  $\varepsilon_r, \mu_r$  - are relative permittivity and permeability of the medium,  $c$  - speed of light in free space.

In the absence of free charge (meaning  $\rho = 0$ ) from the Eq. 1.22 we get that

$$\nabla \bullet \vec{D} = \varepsilon (\nabla \bullet \vec{E}) = 0. \quad (1.31)$$

Applying vector identity  $\nabla \times (\nabla \times V) = \nabla(\nabla \bullet V) - \nabla^2 V$  and solving Eqs. 1.24, 1.25 for  $\vec{E}$  we find

$$\nabla^2 \vec{E} = \varepsilon \mu \frac{\partial^2 \vec{E}}{\partial t^2} + \mu \sigma \frac{\partial \vec{E}}{\partial t} \quad (1.32)$$

that describes inhomogeneous wave equation. The similar holds for  $\vec{H}$ . In the lack of currents, meaning  $j = 0$ , we get the solution in the form of homogeneous wave equation:

$$\nabla^2 \vec{E} = \varepsilon \mu \frac{\partial^2 \vec{E}}{\partial t^2} \quad (1.33)$$

One of a particular solutions of the Eq. 1.32 is a linearly polarized harmonic wave that in complex form can be represented as:

$$\tilde{E} = \mathcal{E} \exp[i(w(t - z/v) + \phi_0)] \quad (1.34)$$

where  $z$  - is the distance traveled by the wave along the axis of propagation,  $v$  - speed of the wave,  $w$  - angular frequency and  $\phi_0$  - relative phase. If to denote  $\mathcal{E} \exp(i\phi)$  as a complex vector amplitude, then the Eq. 1.34 can be re-written as

$$\tilde{E} = \mathcal{E} \exp[iw(t - z/v)]. \quad (1.35)$$

In order the Eq. 1.35 to be the solution of the Eq. 1.32, it is necessary that

$$w^2/v^2 = w^2\varepsilon\mu - iw\mu\sigma. \quad (1.36)$$

Keeping in mind that  $c^2 = 1/\varepsilon_0\mu_0$ , multiplying by  $c^2$  and dividing by  $w^2$  we can re-write Eq. 1.36 as

$$\frac{c^2}{v^2} = \frac{\varepsilon\mu}{\varepsilon_0\mu_0} - i\frac{\mu\sigma}{w\varepsilon_0\mu_0}. \quad (1.37)$$

$c/v$  is a dimensionless parameter of the medium defying the major differences of the propagating medium to vacuum. We denote it as  $N$  - a complex refractive index. We represent it in the form  $N = n - ik$ , where  $n$  - is a real part of complex refractive index or simply refractive index and  $k$  - is an extinction coefficient. Consequently,

$$N^2 = \varepsilon_r\mu_r - i\frac{\mu_r\sigma}{w\varepsilon_0} = (n^2 - k^2) - i2nk. \quad (1.38)$$

With the new description of  $N$  we can re-write Eq. 1.35 as

$$\tilde{E} = \mathcal{E} \exp[i(wt - \frac{2\pi N}{\lambda}z)] = \mathcal{E} \exp[-\frac{2\pi k}{\lambda}z] \exp[i(wt - \frac{2\pi n}{\lambda}z)]. \quad (1.39)$$

The significance of  $k$  emerges as being a measure of absorption in the medium. The distance  $\lambda/(2\pi k)$  is that in which the amplitude of the wave falls by  $1/e$  of its original value. It is usually assumed that  $k$  is infinitely small in the transparency region of dielectric thin-film materials. However, in the following chapters we will see, that when the working spectral range approaches ultraviolet, the presence of absorption should not be ignored.

$2\pi n/\lambda = nw/c$  is a change in the phase of the wave produced by traveling distance  $z$  in the medium or distance  $nz$  in vacuum. The distance  $nz$  is known as optical distance and is of more importance for the thin-film design than the actual physical distance  $z$ . The exact calculation and control over this produced phase difference lies at the heart of the development of dispersive multilayer thin-film coatings that will be in details discussed in following chapters.

As it is not always comfortable to drag multiple constants from equation to equation, we introduce a parameter  $\mathcal{Y}$  that is a characteristic admittance of the free space. it is given by

$$\mathcal{Y} = (\varepsilon_0/\mu_0)^{\frac{1}{2}}. \quad (1.40)$$

Then the characteristic admittance of any media in the lack of magnetic interactions  $v$  can be represented as

$$y = N\mathcal{Y}. \quad (1.41)$$

### 1.2.1 The Poynting vector

An important feature of electromagnetic radiation is that it is a form of energy transport, and it is the energy associated with the wave, which is normally observed. The instantaneous rate of the flow of energy across unity area is given by the Poynting vector

$$S = E \times H, \quad (1.42)$$

where  $E$  and  $H$  are vectors. The direction of the vector is the direction of energy flow. The mean of this vector is of significance for us, as it is precisely what we measure. It is defined as irradiance  $I$ . Using the complex form of the wave we can derive it as

$$I = \frac{1}{2} \text{Re}(E \times H^*), \quad (1.43)$$

where  $*$  denotes complex conjugate. The irradiance in the Eq. 1.43 is a vector value and its direction points the direction of the energy flow. The more usual scalar irradiance is a magnitude of  $I$ . Since  $E$  and  $H$  are perpendicular, the Eq. 1.43 can be re-written as

$$I = \frac{1}{2} \text{Re}(EH^*), \quad (1.44)$$

where  $E$  and  $H$  are scalar magnitudes now. The total irradiance is preserved between all the interacting waves.

### 1.2.2 Simple boundary

Thin-film coatings usually consist of a number of boundaries between various homogeneous media, and it is the effect of these boundaries on the incident wave that defines the functionality of the coating. A single boundary is the simplest case. The most general arrangement is sketched in the Fig. 1.3. A linearly polarized harmonic wave is incident on a plane separating the incident medium with refractive index  $n_0$  from adjoining homogeneous medium of refractive index  $n_1$ . The vector indicates the direction of the energy flow (Poynting vector), belongs to the incidence plane and has an angle  $\theta_0$  with the direction that is normal to the plain of the boundary. Axis  $z$  is normal to the plane of the boundary, axes  $x$  and  $y$  are in the boundary plane and perpendicular to one another.

In order to understand in qualitative and quantitative ways the performance of thin-film optical coatings, it is necessary to accept several simple conventions:

- upon incidence on the boundary a part of the incident way is reflected back and a part is transmitted into the adjoining medium at an angle of  $\theta_1$ ; the incident, reflected and transmitted waves are belonging to the same plane - the plane of incidence - and  $n_0 \sin \theta_0 = n_1 \sin \theta_1$  - Snell's law;
- there is a phase shift of  $\pi$  when the reflectance takes place in the medium of lower refractive index than the adjoining medium and 0 if the medium has a higher refractive index than the adjoining medium;

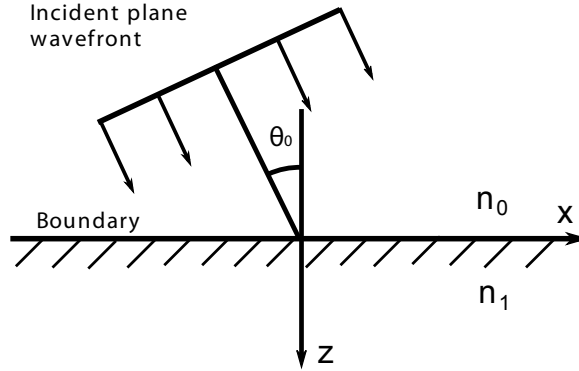


Figure 1.3: Plane wavefront incident on a single surface.

- beams interfere constructively if the relative phase difference between them is a multiple of  $2\pi$  and destructively if it is an odd multiple of  $\pi$ ;
- at a boundary, i.e.  $z = 0$ , the tangential components of  $\mathcal{E}$  and  $\mathcal{H}$  - that is, the components along the boundary - are continuous across it; this boundary condition is **fundamental** for the thin-film theory.

### 1.2.3 Normal incidence

Let's consider the case of normal incidence first, Fig. 1.4, angle  $\theta_0$  in this case is  $0^\circ$ . The positive direction of the vector  $\vec{E}$  is along the  $x$  axis and the positive direction of the vector  $\vec{H}$  is along  $y$  axis. After the incidence on the boundary, the wave is partially transmitted and partially reflected. As the reflected wave changed the direction of propagation and we decide to preserve the direction of the vector  $\vec{E}$  along the positive direction of the  $x$  axis, the  $\vec{H}$  vector of the reflected wave has now to be along the negative direction of the  $y$  axis in order to preserve the right-handed vector set.

After applying the boundary conditions we deduce following equations:

- (a) Electric vector is continuous across the boundary

$$\mathcal{E}_i + \mathcal{E}_r = \mathcal{E}_t. \quad (1.45)$$

- (b) Magnetic vector is continuous across the boundary

$$\mathcal{H}_i - \mathcal{H}_r = \mathcal{H}_t \quad (1.46)$$

Using the relationship between the electric and magnetic field via characteristic admittance, we can re-write Eq. 1.46 as

$$y_0 \mathcal{E}_i - y_0 \mathcal{E}_r = y_1 \mathcal{E}_t. \quad (1.47)$$

Eliminating  $\mathcal{E}_t$  we get

$$y_0(\mathcal{E}_i - \mathcal{E}_r) = y_1(\mathcal{E}_i + \mathcal{E}_r) \quad (1.48)$$

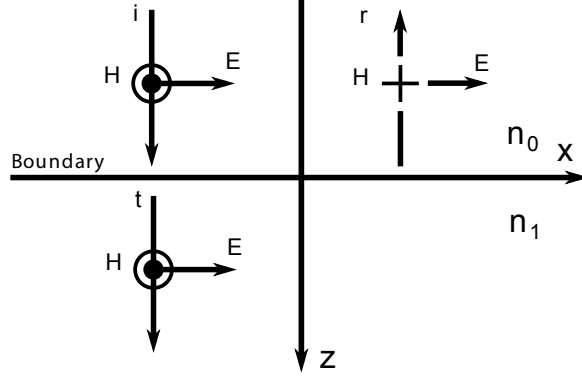


Figure 1.4: Convention defining positive directions of the electric and magnetic vectors for reflection and transmission at an interface at normal incidence.

and consequently

$$\frac{\mathcal{E}_r}{\mathcal{E}_i} = \frac{y_0 - y_1}{y_0 + y_1} = \frac{N_0 - N_1}{N_0 + N_1}. \quad (1.49)$$

For the spectral ranges where the materials are considered to be transparent, non-absorbing,  $N$  is reduced to  $n$ .

Similarly eliminating  $\mathcal{E}_r$  from the Eq. 1.45 and Eq. 1.46, we get

$$\frac{\mathcal{E}_t}{\mathcal{E}_i} = \frac{2y_0}{y_0 + y_1} = \frac{2N_0}{N_0 + N_1}. \quad (1.50)$$

The quantities in the Eqs. 1.49, 1.50 are called amplitude reflection and transmission coefficients and are denoted as  $\rho$  and  $\tau$  accordingly.

$$\rho = \frac{y_0 - y_1}{y_0 + y_1} = \frac{N_0 - N_1}{N_0 + N_1} \quad (1.51)$$

$$\tau = \frac{2y_0}{y_0 + y_1} = \frac{2N_0}{N_0 + N_1}. \quad (1.52)$$

As the boundary is of zero thickness it can neither supply nor extract energy, thus, the Poynting vector is as well continuous across the boundary. Therefore

$$I = \frac{1}{2} \text{Re}(EH^*) = \text{Re}\left[\frac{1}{2}(\mathcal{E}_i + \mathcal{E}_r)(y_0\mathcal{E}_i - y_0\mathcal{E}_r)^*\right] = \text{Re}\left[\frac{1}{2}\mathcal{E}_t(y_1\mathcal{E}_t)^*\right]. \quad (1.53)$$

Substituting  $\mathcal{E}_r = \rho\mathcal{E}_i$  and  $\mathcal{E}_t = \tau\mathcal{E}_i$ , we get

$$I = \frac{1}{2}y_0(1 - \rho^2)\mathcal{E}_i\mathcal{E}_i^* = \frac{1}{2}y_1\tau^2\mathcal{E}_i\mathcal{E}_i^*. \quad (1.54)$$

As  $\frac{1}{2}y_0\mathcal{E}_i\mathcal{E}_i^*$  is the incident irradiance  $I_i$ , we can reduce the equation to

$$(1 - \rho^2) = \frac{y_1}{y_0}\tau^2. \quad (1.55)$$

In the absence of absorption,  $k = 0$  this identity is commonly known as

$$1 - R = T \quad (1.56)$$

where  $R$  is reflectance and  $T$  is transmittance and

$$R = \frac{I_r}{I_i} = \rho^2 = \left(\frac{n_0 - n_1}{n_0 + n_1}\right)^2 \quad (1.57)$$

$$T = \frac{I_t}{I_i} = \frac{y_1}{y_0} \tau^2 = \frac{4n_0 n_1}{(n_0 + n_1)^2}. \quad (1.58)$$

Note, that in presence of absorption  $\rho$  and  $\tau$  are complex values, thus the expression 1.56 will not hold.

### 1.2.4 Oblique incidence

For a general direction of a vector amplitude of an incident wave, expressions for the vector amplitudes of reflected and transmitted waves quickly become complicated. Luckily, the endless possible variations of the incident direction can be represented as a superposition of only two major vector electrical amplitude orientations: a) vector electrical amplitudes are situated in the plane of incidence or (Fig. 1.5a ) b) vector electrical amplitudes are normal to the plain of incidence (Fig. 1.5b ). A wave with the electric vector located *in* the incident plane is called transverse magnetic (TM) or *p-polarised* and a wave with the electric vector *normal* to the plane of incidence – is transverse electric (TE) or *s-polarised*.

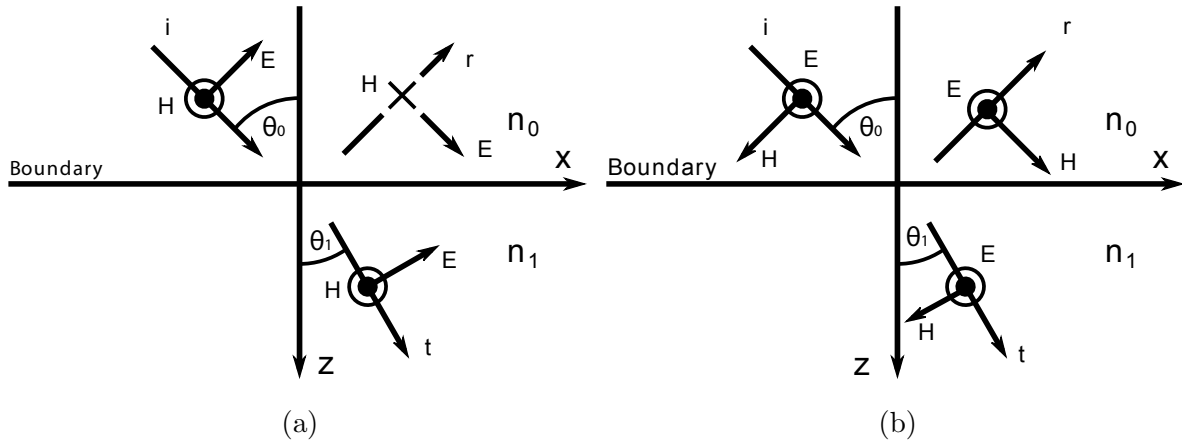


Figure 1.5: For p-polarised light (TM wave) (a) and for s-polarised light(TE wave)(b).

Similarly to the case of normal incidence, we choose to preserve the direction of the electric field vector along the positive directions of the relevant axes, i.e. for p-polarised wave – along  $x$ -axis, for s-polarised wave – along  $y$ -axis. We can now apply the boundary conditions Eqs. 1.45 - 1.46.

## P–polarised wave

(a) Electric component parallel to the boundary is continuous across it.

$$\mathcal{E}_i \cos(\theta_0) + \mathcal{E}_r \cos(\theta_0) = \mathcal{E}_t \cos(\theta_1). \quad (1.59)$$

(b) Magnetic component parallel to the boundary is continuous across it.

$$\mathcal{H}_i - \mathcal{H}_r = \mathcal{H}_t \quad (1.60)$$

$$y_0 \mathcal{E}_i - y_0 \mathcal{E}_r = y_1 \mathcal{E}_t. \quad (1.61)$$

In order to reduce the boundary conditions to the already discussed normal incidence case, we should, however, substitute the tangential components of  $E$  and  $H$  in the form of  $\mathcal{E} \cos(\theta) / \mathcal{H} \cos(\theta)$  by equivalent tangential amplitudes  $E$  and  $H$ . We can write

$$E_i = \mathcal{E}_i \cos(\theta_0) \quad H_i = \mathcal{H}_i = y_0 \mathcal{E}_i = \frac{y_0}{\cos(\theta_0)} E_i \quad (1.62)$$

$$E_r = \mathcal{E}_r \cos(\theta_0) \quad H_r = \frac{y_0}{\cos(\theta_0)} E_r \quad (1.63)$$

$$E_t = \mathcal{E}_t \cos(\theta_1) \quad H_t = \frac{y_1}{\cos(\theta_1)} E_t. \quad (1.64)$$

Preserving the analogy between the normal and oblique incidence, value

$$\gamma_p = y / \cos(\theta) = H/E \quad (1.65)$$

is denoted as optical admittance at oblique incidence for p-polarised light.

## S–polarised light

Similarly, in the case of s-polarised (Fig. 1.5b ) light the boundary conditions take shape of

(a) Electric component parallel to the boundary is continuous across it.

$$\mathcal{E}_i + \mathcal{E}_r = \mathcal{E}_t. \quad (1.66)$$

(b) Magnetic component parallel to the boundary is continuous across it.

$$\mathcal{H}_i \cos(\theta_0) - \mathcal{H}_r \cos(\theta_0) = \mathcal{H}_t \cos(\theta_1) \quad (1.67)$$

$$y_0 \mathcal{E}_i \cos(\theta_0) - y_0 \mathcal{E}_r \cos(\theta_0) = y_1 \mathcal{E}_t \cos(\theta_1). \quad (1.68)$$

Re–writing in the frame of tangential amplitudes:

$$E_i = \mathcal{E}_i \quad H_i = \mathcal{H}_i \cos(\theta_0) = y_0 \cos(\theta_0) \mathcal{E}_i = y_0 \cos(\theta_0) E_i \quad (1.69)$$

$$E_r = \mathcal{E}_r \quad H_r = y_0 \cos(\theta_0) E_r \quad (1.70)$$

$$E_t = \mathcal{E}_t \quad H_t = y_1 \cos(\theta_1) E_t. \quad (1.71)$$

Again, we can denote  $\gamma_s = y \cos(\theta)$  as optical admittance at oblique incidence for s-polarised light.

With the introduced notation, we can repeat the routine of the Sec. 1.2.3 and find that the established expressions hold for the new notation as well, i.e

$$\rho = \frac{\gamma_0 - \gamma_1}{\gamma_0 + \gamma_1}, \quad \tau = \frac{2\gamma_0}{\gamma_0 + \gamma_1} \quad (1.72)$$

$$R = \rho^2 = \left(\frac{\gamma_0 - \gamma_1}{\gamma_0 + \gamma_1}\right)^2, \quad T = \frac{\gamma_1}{\gamma_0} \tau^2 = \frac{4\gamma_0\gamma_1}{(\gamma_0 + \gamma_1)^2}. \quad (1.73)$$

### 1.2.5 The reflectance of a thin film

Let us consider now two boundaries, separated by a material of thickness  $d$ , Fig. 1.6a, - the film. Presence of two or more interfaces means that a number of reflected beams will be produced and the properties of the assembly will be defined by the summation of all the produced beams. The film is considered *thin* when interference effects between the produced beams can be detected in reflected or transmitted light. Whether the film is *thin* or *thick* naturally depends on the wavelength of the light source and its coherence length. The same film might appear thick or thin depending on illumination conditions.

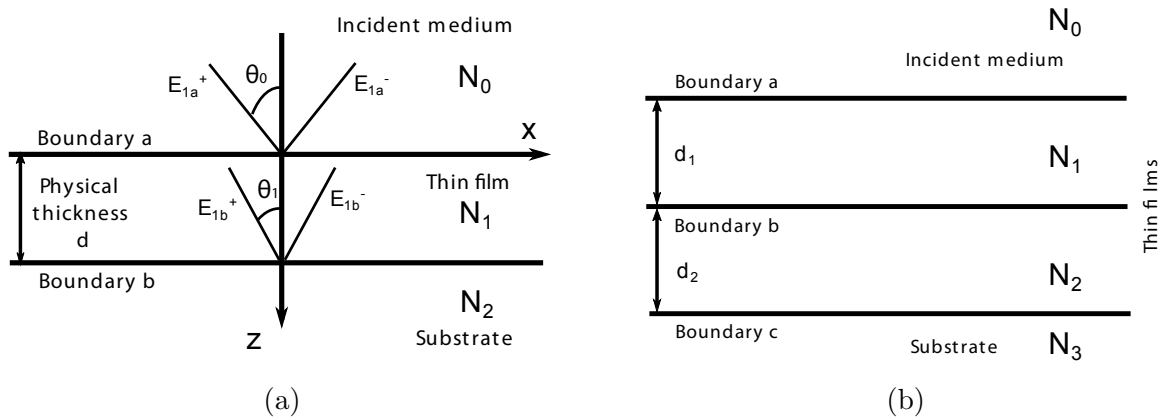


Figure 1.6: (a) Plane wave front incident on a thin film. (b) Assembly of thin films.

Let's consider a case of plane wave incident on a thin film, Fig. 1.6a. We denote waves traveling in direction of incidence as + and in opposite direction - -. The interface  $b$  between the film and the substrate can be treated in the exact same way as the simple boundary. We suppose, that there is no negative traveling wave in the substrate. We now consider the waves *in the film* only. In that case the resultant wave in the film is a sum of only two waves: positive going and negative going. At the boundary  $b$  the tangential components of the electric and magnetic field  $E$  and  $H$  are

$$E_{1b} = E_{1b}^+ + E_{1b}^- \quad (1.74)$$

$$H_{1b} = H_{1b}^+ - H_{1b}^- = \gamma_1 E_{1b}^+ - \gamma_1 E_{1b}^-. \quad (1.75)$$

Extracting  $E_{1b}^+$  and  $E_{1b}^-$ , we get

$$E_{1b}^+ = \frac{1}{2} \left( \frac{H_b}{\gamma_1} + E_b \right) \quad (1.76)$$

$$E_{1b}^- = \frac{1}{2} \left( -\frac{H_b}{\gamma_1} + E_b \right) \quad (1.77)$$

$$H_{1b}^+ = \gamma_1 E_{1b}^+ = \frac{1}{2} (H_b + \gamma_1 E_b) \quad (1.78)$$

$$H_{1b}^- = -\gamma_1 E_{1b}^- = \frac{1}{2} (H_b - \gamma_1 E_b). \quad (1.79)$$

The waves at the interface  $a$  at the same instant and at the point with the same  $x$  and  $y$  coordinates can be determined altering the phase factors of the traveling wave by the phase acquired via traveling the distance  $d$  along the  $z$  direction in the film. In case of oblique incidence, the  $d$  is corrected by the  $\cos(\theta_1)$ , i.e

$$\delta = 2\pi N_1 d \cos(\theta_1) / \lambda \quad (1.80)$$

where  $\delta$  is the additional phase. The phase factor of the positive going wave will be multiplied by  $\exp(i\delta)$ , while the phase factor of the negative going way will be multiplied by  $\exp(-i\delta)$ . It is implied in that definition, that the film is thin.

The values of  $E$  and  $H$  at the interface  $a$  are now

$$E_{1a}^+ = E_{1b}^+ e^{i\delta} = \frac{1}{2} \left( \frac{H_b}{\gamma_1} + E_b \right) e^{i\delta} \quad (1.81)$$

$$E_{1a}^- = E_{1b}^- e^{-i\delta} = \frac{1}{2} \left( -\frac{H_b}{\gamma_1} + E_b \right) e^{-i\delta} \quad (1.82)$$

$$H_{1a}^+ = H_{1b}^+ e^{i\delta} = \frac{1}{2} (H_b + \gamma_1 E_b) e^{i\delta} \quad (1.83)$$

$$H_{1a}^- = H_{1b}^- e^{-i\delta} = \frac{1}{2} (H_b - \gamma_1 E_b) e^{-i\delta} \quad (1.84)$$

so that

$$E_a = E_{1a}^+ + E_{1a}^- = E_b \left( \frac{e^{i\delta} + e^{-i\delta}}{2} \right) + H_b \left( \frac{e^{i\delta} - e^{-i\delta}}{2\gamma_1} \right) = E_b \cos(\delta) + H_b \frac{i \sin(\delta)}{\gamma_1} \quad (1.85)$$

$$H_a = H_{1a}^+ + H_{1a}^- = E_b \gamma_1 \left( \frac{e^{i\delta} - e^{-i\delta}}{2} \right) + H_b \left( \frac{e^{i\delta} + e^{-i\delta}}{2} \right) = E_b i \gamma_1 \sin(\delta) + H_b \cos(\delta). \quad (1.86)$$

This can be re-written in the matrix notation as

$$\begin{bmatrix} E_a \\ H_a \end{bmatrix} = \begin{bmatrix} \cos(\delta) & (i \sin(\delta))/\gamma_1 \\ i\gamma_1 \sin(\delta) & \cos(\delta) \end{bmatrix} \begin{bmatrix} E_b \\ H_b \end{bmatrix} \quad (1.87)$$

The  $2 \times 2$  matrix on the right-hand side of the Eq. 1.87 is called the characteristic matrix on the thin film. By analogy with the Eq. 1.65, we can define the input admittance of the thin film as

$$Y = H_a/E_a \quad (1.88)$$

The equation 1.87 turns into

$$E_a \begin{bmatrix} 1 \\ Y \end{bmatrix} = \begin{bmatrix} \cos(\delta) & (i \sin(\delta))/\gamma_1 \\ i\gamma_1 \sin(\delta) & \cos(\delta) \end{bmatrix} \begin{bmatrix} 1 \\ \gamma_2 \end{bmatrix} E_b \quad (1.89)$$

Then calculating a reflectance of the thin film reduces to a problem of calculating a reflectance from a simple boundary between media with admittances  $\gamma_0$  and  $Y$ , i.e. in general case when admittances are complex numbers

$$\rho = \frac{\gamma_0 - Y}{\gamma_0 + Y} \quad (1.90)$$

$$R = \rho\rho^* = \left(\frac{\gamma_0 - Y}{\gamma_0 + Y}\right)\left(\frac{\gamma_0 - Y}{\gamma_0 + Y}\right)^* \quad (1.91)$$

where from the Eq. 1.89  $Y$  can be calculated as

$$Y = \frac{\gamma_2 \cos(\delta) + i\gamma_1 \sin(\delta)}{\cos(\delta) + i(\gamma_2/\gamma_1) \sin(\delta)}. \quad (1.92)$$

### 1.2.6 The reflectance of an assembly of thin films

Let us now consider an assembly of two thin films, Fig. 1.6b.

In analogy with the Eq. 1.87, each added layer will be described by its characteristic matrix and the assembly of two will be fully described by the multiplication of the layer's individual matrices, i.e.

$$\begin{bmatrix} E_a \\ H_a \end{bmatrix} = \begin{bmatrix} \cos(\delta) & (i \sin(\delta))/\gamma_1 \\ i\gamma_1 \sin(\delta) & \cos(\delta) \end{bmatrix} \begin{bmatrix} \cos(\delta) & (i \sin(\delta))/\gamma_1 \\ i\gamma_1 \sin(\delta) & \cos(\delta) \end{bmatrix} \begin{bmatrix} E_b \\ H_b \end{bmatrix} \quad (1.93)$$

This can be immediately extended to the assembly of  $q$  layers, when the characteristic matrix of the whole assembly is a simply a product of the characteristic matrices of each individual layers multiplied in right order.

$$\begin{bmatrix} 1 \\ Y \end{bmatrix} = \prod_{r=1}^q \begin{bmatrix} \cos(\delta_r) & (i \sin(\delta_r))/\gamma_r \\ i\gamma_r \sin(\delta_r) & \cos(\delta_r) \end{bmatrix} \begin{bmatrix} 1 \\ \gamma_m \end{bmatrix} \quad (1.94)$$

It is interesting to examine the phase shift associated with the reflected beam. If represent  $Y = a + ib$ , then with  $\gamma_0$  being real

$$\rho = \frac{\gamma_0 - a - ib}{\gamma_0 + a + ib}, \quad (1.95)$$

$$\text{i.e. } \tan \phi = \frac{(-2b\gamma_0)}{(\gamma_0^2 - a^2 - b^2)}. \quad (1.96)$$

Control over this value is a pivotal idea behind the design and functionality of the thin-film multilayer dispersive optics, which will be described in finer details in the Chapter 4.

# Chapter 2

## Hybrid degenerate/nondegenerate phase-stable infrared optical parametric chirped pulse amplifier

The present chapter guides through a development of the intense one-and-a-half cycle phase-stable 1.3 mJ near-infrared optical parametric chirped pulse amplifier (OPCPA) that is later utilized for generation of an ultra broadband supercontinuum seeding the multi-channel, multi-color optical waveform synthesizer.

The chapter is prepared in the form of a journal letter and is planned for a later submission to a peer-reviewed journal.

### 2.1 Introduction and motivation

Observation [36, 75, 76] and theoretical justification [77, 78, 79] of the extreme ultraviolet generation via the high-harmonic up-conversion of intense near-infrared sources has marked the beginning of the attosecond science. Its rapid growth in the beginning of this century saw vast progress in the development of the high-energy ultrafast coherent light sources. Due to the large amplification bandwidth allowing the direct generation of pulses comprising only a few oscillations of the driving field, Ti:Sapphire-based systems held a decade long monopoly for being the attosecond driving lasers.

However, for advancing into the water window - a region between carbon K-edge (282 eV  $\sim$  4.40 nm) and oxygen K-edge (533 eV  $\sim$  2.33 nm) - that is vital for investigating carbon-based life, the Ti:Sapphire sources centered at a wavelength of  $\sim$  780 nm are not optimal. Following the cut-off rule for the maximum electron energy, the latter scales directly proportional to the squared wavelength of the driving electric field and linearly with intensity:

$$h\nu_{cut-off} = I_p + 3.17U_p \approx I_l \lambda_l^2, \quad (2.1)$$

where  $I_p$  is ionization potential,  $U_p$  - ponderomotive energy of the free electron acquired

## 2. Hybrid degenerate/nondegenerate phase-stable infrared optical parametric chirped pulse amplifier

in the electric field,  $I_l$  – field intensity,  $\lambda_l$  – carrier wavelength. Therefore, moving the cut-off further into soft x-rays requires either a substantial scaling of the near-infrared field intensity [80] or implementation of a driving source at lower photon energies. As the incident intensity is limited by the ionization rate of the gas species and can not be scaled infinitely due to a formation of a dense and dispersive plasma, using the driving sources with lower photon energies has been chosen by many as more technologically and practically feasible approach [81, 82, 83] and, consequently, stimulated extensive activities in the corresponding field.

Soon after it was realized that other branches of the attosecond physics, namely time-resolved attosecond polarization spectroscopy [12], may largely benefit from the availability of the sources with lower (in comparison to  $\sim 1.6$  eV (780 nm)) photon energies. The technique analyze the imprint that the carrier dynamics in scope leaves on the transmitted electric field. Several experiments have concentrated on scrutinizing the band gap dynamics of dielectric materials, including silicon oxide, that are of interest and importance for application to light-wave-governed signal processing. Performing similar investigations with the conventional semiconductor materials that have a much lower band gap, however, is less sensible due to the high photon energy of the excitation pulses that bleaches the material and hinders the unambiguous interpretation of the measurements along with damaging the sample. Few-cycle sources with the lower excitation energies are more beneficial in this respect. Apart from the central wavelength, another crucial requirement is, however, a phase-stability of the driver that is needed for the field-sensitive measurements.

In the lack of broadband infrared gain media, generation of few-cycle phase-stable pulses in the infrared is substantially more challenging than in case of Ti:Sapphire-based systems. The access to the wavelengths in the infrared is possible through difference frequency generation. This path in some cases also enables passive CEP-stabilization of the generated spectrum via phase cancellation in the DFG process – pivotal requirement for field-resolved measurements – and due to that this approach quickly became a method of choice [84, 85]. Subsequent amplification in one or more OPA stages [46, 86, 87, 60, 61] boosts the output energy by several orders of magnitude.

Nevertheless, a broadband amplification supporting potentially sub-two-cycle pulses is still difficult due to unavailability of broadband and robust amplification media. Periodically poled lithium niobate (PPLN) crystals support unprecedented amplification bandwidth, yet suffer from photorefractive damage at relatively low intensities and can not be produced in large apertures. Therefore, scaling the energies to mJ levels with PPLN is less plausible. For years, PPLN's non-poled counterpart – bulk lithium niobate  $\text{LiNbO}_3$  – was used for amplification of intense broadband pulses centered at  $\mu 2 \mu\text{m}$ . Bulk  $\text{LiNbO}_3$  has a inferior amplification bandwidth in comparison to PPLN, however its higher damage threshold and zero dispersion point (ZDP) at  $1.9 \mu\text{m}$  made it to a good alternative for degenerate broadband amplification at  $\sim 2 \mu\text{m}$ . Yet, it is far from perfect. It continues to suffer from photorefractive damage at fairly low intensities, and performs poorly under high power conditions as a result. More problematic is the low efficiency of  $\text{LiNbO}_3$  – based systems. Although it has broadband, degenerate phase-matching for  $\sim 2 \mu\text{m}$  range, this carries the necessary consequence that second harmonic generation (SHG) is also well

phase-matched in the crystal becoming a second loss channel and reducing the overall OPA efficiency.

Barium borate (BBO) crystals have much larger damage thresholds, but limited amplification bandwidths at  $\sim 2 \mu\text{m}$ , largely due to the fact that its ZDP lies at  $1.49 \mu\text{m}$ . However, an elegant combination of two types of BBO crystals suggested by Dr. Nicholas Karpowicz seemed to be able to circumvent the troublesome limitations allowing for development of a broadband, efficient, BBO-based OPCPA scheme.

Here we present our work on development of hybrid degenerate/nondegenerate BBO-based OPCPA that yielded generation of sub-two-cycle  $\sim 11 \text{ fs}$   $2 \text{ mJ}$  pulses at a central wavelength of  $\sim 2 \mu\text{m}$ .

## 2.2 Concept and theoretical justification

BBO is generally not an ideal amplification media for our combination of signal and pump wavelengths. Although it is a robust and readily available crystal, its shorter ZDP wavelength ( $1.49 \mu\text{m}$ ) means that it shows strong negative dispersion across the desired amplification window, making broadband, degenerate phase-matching impossible. Since the dispersion is negative, the bandwidth limitation can't be bent by noncollinear phase-matching, since the angle between pump and signal simply reduces the bandwidth further. Second harmonic generation is phase-matched in degenerate BBO OPAs as well, although with a reduction in bandwidth compared to  $\text{LiNbO}_3$ .

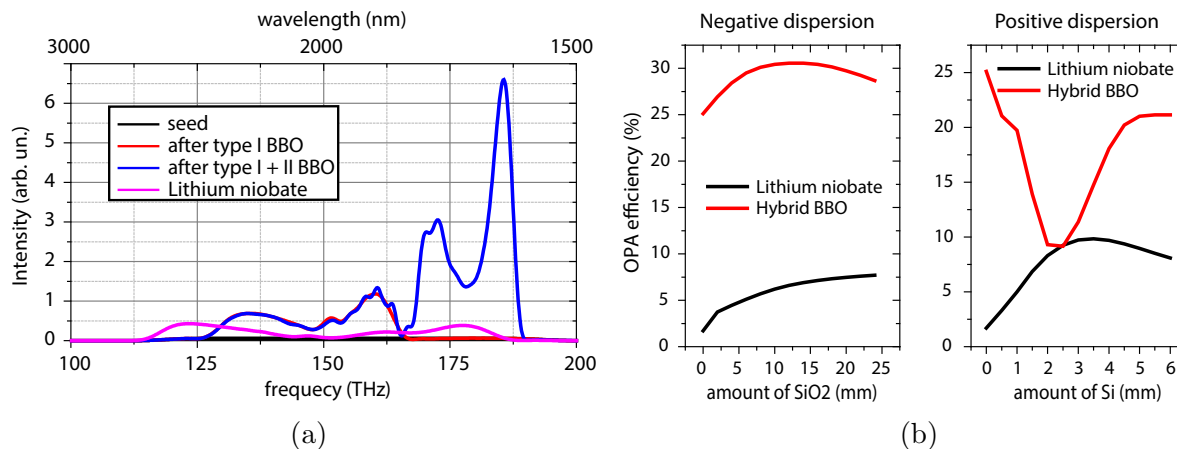


Figure 2.1: Hybrid degenerate/nondegenerate OPCPA. (a) Simulated amplification spectrum of the hybrid BBO assembly (blue) in comparison to bulk lithium niobate (magenta); (b) Dependence of the OPA efficiency from the stretching of the seeding pulse.

Degenerate phase-matching is not the only possibility, however. In type II OPAs, the signal and idler travel on different axes of the crystal, for example the signal on the slow axis and the idler on the fast axis. As a result, phase-matching will favor a shorter wavelength

on the slow axis of the crystal. The type II process tends to be more narrow band as the nondegeneracy leads to poor group-velocity matching.

This is not always the case, though. In the type II process in BBO, phase-matching near the ZDP can be surprisingly broadband. Due to the large birefringence of BBO, this broadband, nondegenerate gain window, when pumped at 1030 nm, is adjacent to, but not overlapping, the degenerate gain window. Additionally the type II process is not accompanied by phase matching of SHG and the absence of the two associated loss channels results in an increase in the achievable conversion efficiency. Simply taking the output of a type-I OPA and feeding it to a type-II crystal creates a hybrid system with more bandwidth than either, and higher efficiency than would be possible in a purely degenerate system.

Dr. Karpowicz simulated the spectra and efficiency of the systems using plane-wave propagation code, under our experimental pumping conditions of the third stage of the OPCPA (70 GW/cm<sup>2</sup>, 1.4 ps, 1030 nm pump with 40 W power, 1.5-2.7 nm seed with 300 mW power). The resulting spectra with LiNbO<sub>3</sub> and BBO are shown in Fig.2.1a. When the type II crystal is used, all outputs of the first crystal are included to watch for detrimental effects from parasitic processes. The LiNbO<sub>3</sub> OPA consists of a single, 2-mm-thick crystal with  $\theta = 45.30^\circ$ , and the BBO crystals are cut at  $\theta = 21.42^\circ$  for type I (4 mm), and  $\theta = 29.48^\circ$  for type II (5 mm).

The gain bandwidths of the LiNbO<sub>3</sub> and hybrid systems are comparable, but with a blue shift of the hybrid system due to the short-wavelength type-II OPA. Both of the degenerate spectra exhibit the characteristic dip in the center associated with SHG, but with a much narrower hole in BBO due to the worse SHG phase-matching and absence of SHG in the type II process.

The maximum achievable efficiency appears to be higher in the hybrid system. It can already be seen in Fig. 2.1b that the saturated energy conversion in the nondegenerate channel is higher (i.e. the higher peak at high frequencies) - this is shown quantitatively as a function of seed stretching in Fig. . The hybrid system achieves very high conversion efficiency. Due to the fact that the ZDP of the BBO lies at  $\sim 1.49 \mu\text{m}$  in comparison to  $1.9 \mu\text{m}$  for LiNbO<sub>3</sub>, the hybrid configuration prefers a positively-chirped seed. Such chirp might be introduced implementing bulk silicon, while the compression can be consequently performed with IR-grade fused silica, sapphire or similar materials. Avoiding the silicon and, thus, potentially problematic two-photon absorption in the output high-energy beam, should simplify compression and preserve beam quality.

## 2.3 Experimental results

### 2.3.1 State of affairs before the start of the current development

The present OPCPA in finer details is described in [87]. However, over the years a large number of modifications have been introduced and here we describe the latest state of the system.

A commercial Ti:Sapphire oscillator (Femtolasers, Rainbow II) seeds commercial multi-pass Ti:Sapphire amplifier (FemtoPower) yielding 20 fs 0.6 mJ pulses at a repetition rate of 3 kHz centered at a central wavelength of  $\sim 780$  nm. 100  $\mu$ J of the output is spectrally broadened in the 300 mm long hollow-core fiber filled with 3 bars of Krypton. The nonlinearly broadened spectrum covers spectral range from 600 nm to 1000 nm and is compressed to  $\sim 5$  fs pulse duration in the set of chirped mirrors. The output beam is focused into 500  $\mu$ m thick type-II BBO crystal for intrapulse DFG. Generated OPCPA seed spans from 1.2  $\mu$ m to 2.7  $\mu$ m and is passively CEP-stable. The spectral phase of the infrared seed pulses is shaped in an acousto-optic programmable dispersive filter (AOPDF) (DAZZLER, Fastlite). The seed is amplified via two OPCPA stages in noncollinear geometry in 5% MgO-doped PPLN crystals with 2 and 1 mm thicknesses for the first and second stage, respectively.

The pump of the OPCPA is a home-built multi-pass Yb:YAG 1030 nm thin-disk regenerative amplifier. For the "rough" temporal synchronization of the seed and pump, a spectral band around 1030 nm of the master Ti:Sapphire Rainbow II oscillator is selected with a band-pass filter and redirected away from the subsequent Ti:Sapphire amplifier. The pulses are pre-amplified in the fiber amplifier, stretched to ps pulse duration, the repetition rate is downgraded to 3 kHz and the resultant pulse train is used as a seed for the thin-disk regenerative amplifier. The "rough" synchronization is supported by active spectrally-resolved cross-correlation [88] stabilization technique that allows for as less as 24 fs RMS jitter between the seed and the pump.

The amplified pulses carrying up to 18 mJ of pulse energy are compressed to  $\sim 1.2$  ps and are used to pump three OPCPA stages. 0.4 mJ and 3 mJ pulse of energy are used to pump first and second amplification stage respectively. The remaining 14 mJ are used to pump the newly developed noncollinear hybrid degenerate/nondegenerate OPCPA.

### 2.3.2 1.3 mJ sub-two-cycle 2.1 $\mu$ m hybrid OPCPA

The schematic of the novel OPCPA is presented in Fig. 2.2a. The collimated output of the second PPLN-based amplification stage is expanded by the factor of three using the all reflective mirror-based telescope assembled of a concave  $f = 400$  mm and a convex  $f = 1200$  mm protected silver mirrors. The beam emerging after the telescope is maintained slightly diverging in order to avoid the collapse of the beam due to self-focusing in the media. The pulse is positively pre-chirped by passing through 6 mm of bulk silicon. Additional pre-chirp is introduced by the DAZZLER and is fine-tuned afterwards.

The collimated pump beam is squeezed by a factor of two in all-reflective dielectric-mirror-based telescope. The seed and the pump are recombined at a small angle in the two-crystal assembly. The phase-matching angles for both crystals of the assembly can be adjusted individually for the broadest possible amplification. Varying the temporal delay between the seed and the pump pulses, we achieved broadband amplification of the seeding spectrum. The output spectrum of the hybrid OPCPA together with the seeding second stage seeding spectrum is depicted in the Fig. 2.2b. The spectra are measured using InGaAs-based commercial grating spectrometer (Ocean Optics, NIRQuest256) with

## 2. Hybrid degenerate/nondegenerate phase-stable infrared optical parametric chirped pulse amplifier

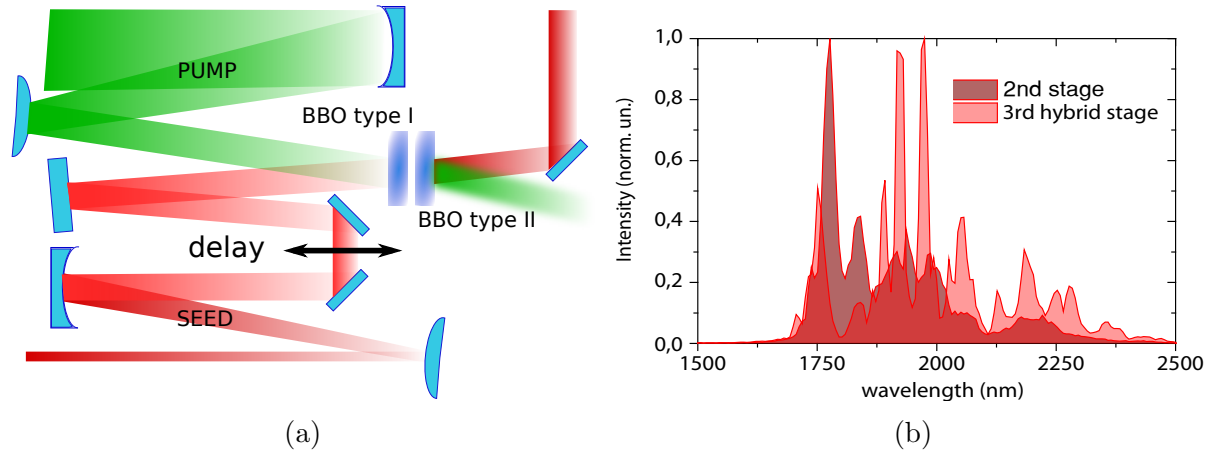


Figure 2.2: Hybrid degenerate/nondegenerate OPCPA. (a) Schematic of the OPCPA stage; (b) the seeding spectrum (light brown) and the amplified spectrum (light red) out of the novel hybrid degenerate/nondegenerate OPCPA.

implemented correction for the spectral sensitivity of the spectrometer.

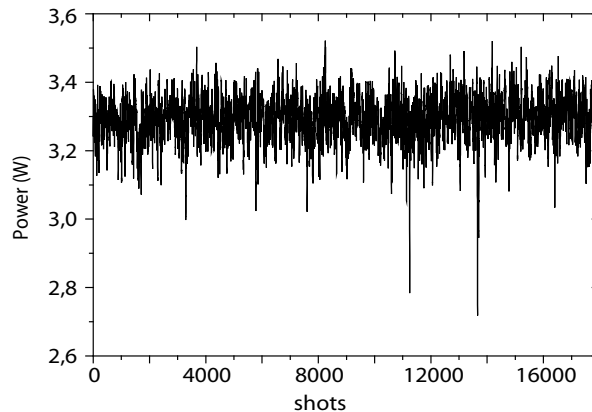


Figure 2.3: OPCPA long-term stability: 30 min time slot, rms noise of  $\leq 2\%$

At the full pump power of 14 mJ the amplified spectrum carries more than 2 mJ of pulse energy. However, due to a substantial thermal load in the lack of active cooling and possible oversaturation, the beam profile in far as well as in the near field noticeably deteriorates, Fig. 2.4a, 2.4b .

As the output beam must later be coupled into a hollow-core fiber, the beam profile quality is of major importance. Reducing the pump energy from 14 mJ to 10 mJ reduces the output pulse energy to 1.3 mJ with substantial improvement of the beam quality, Fig. 2.4c, 2.4d. Yet, the OPCPA remains saturated, thus, demonstrating low rms noise of  $\leq 2\%$  as confirmed by the measurement of the power stability over a 30 minute, Fig. 2.3.

The pulse compression is accomplished in 10 mm of bulk sapphire allowing to avoid two-photon absorption and consequent further deterioration of the beam quality. The

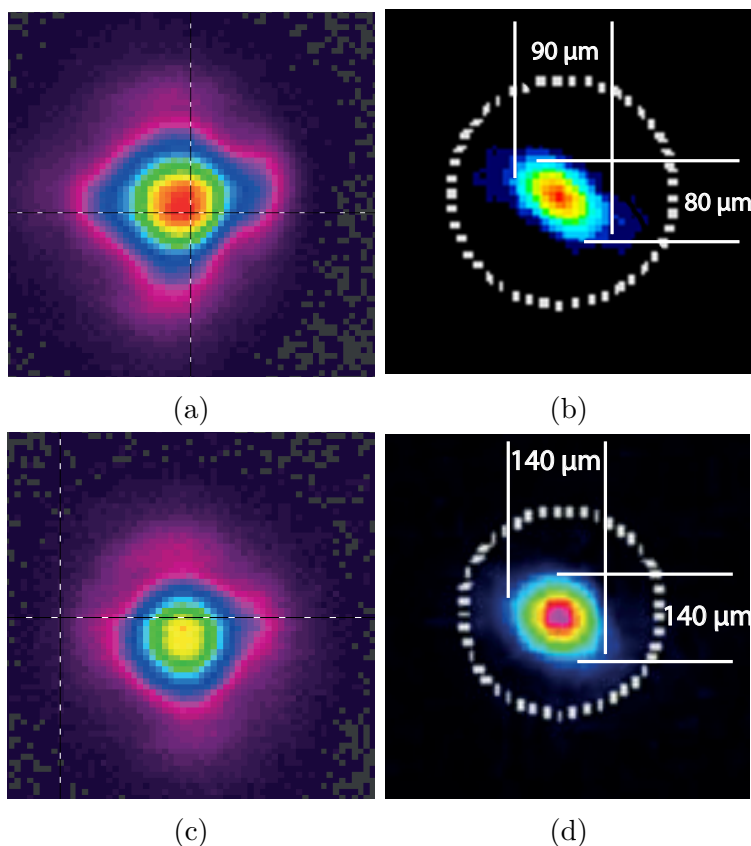


Figure 2.4: Hybrid degenerate/nondegenerate OPCPA mode. (a) Beam profile in the far field and (b) in the near field in case of over saturation; (c) beam profile in far and (d) near field in case of saturation.

fine tuning of the dispersion is performed with the assistance of DAZZLER. The temporal characterization of the pulses was performed using third-harmonic frequency-resolved optical gating (TH-FROG) apparatus [63]. Measured and reconstructed traces revealing compression to  $\sim 11$  fs are presented in Fig. 2.5. Good correspondence between the reconstructed, Fig. 2.5c, and measured, Fig. 2.2b, OPCPA spectra confirms consistency of the measurement.

## 2.4 Conclusion of Chapter 2

In conclusion, we have presented a novel approach for designing broadband, efficient high-energy BBO-based OPCPAs. The intrinsic bandwidth limitation set by the amplification bandwidths of the individual BBO crystals was mitigated implementing the hybrid crystal arrangement combining relatively broadband degenerate amplification in a type-I BBO with efficient, narrowband spectrally offset amplification in the type-II BBO. The combined bandwidths of both exceeds the amplification bandwidth of the individual crystals and is

## 2. Hybrid degenerate/nondegenerate phase-stable infrared optical parametric chirped pulse amplifier

24

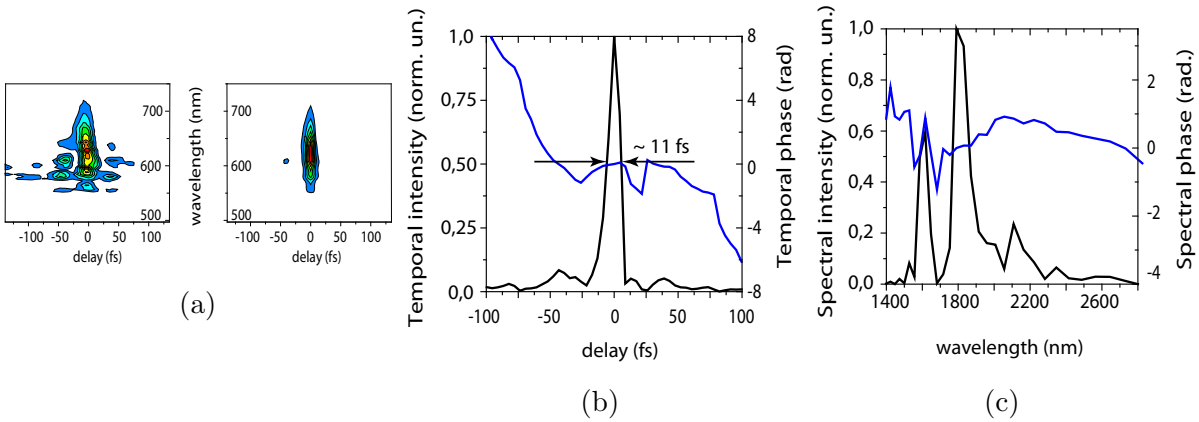


Figure 2.5: Spectra-temporal characterization of the novel hybrid OPCPA. (a) recorded and reconstructed TH-FROG spectrogram; (b) reconstructed temporal profile (black) and temporal phase (blue);(c) reconstructed spectral profile (black) and spectral phase (blue) of the OPCPA pulse.

comparable to the amplification bandwidth of a commonly used  $\text{LiNbO}_3$  crystals. The higher damage threshold of the BBO allows for demonstrated energy scalability into a multi-mJ levels without a danger of a photo refractive damages. Passive CEP-stability is insured by the mechanism of the seed generation and is confirmed in the Chapter 3. Unluckily, at the present state the OPCPA suffers from the over saturation that doesn't allow to explore its ultimate potential. However, future feasible improvements such as active cooling and minor re-designing should be able to defeat these flaws.

# Chapter 3

## Generation of a multi-octave phase-stable supercontinuum in ambient-air- or argon-filled hollow-core fiber

This chapter is largely adapted from the O. Razskazovskaya et. al "Generation of a multi-octave phase-stable supercontinuum in ambient-air- or argon-filled hollow-core fiber", in preparation.

This chapter presents generation of an ultra broadband CEP-stable supercontinuum via spectral broadening of a six-cycle and a sub-two-cycle mJ-level pulses centered at a central wavelength of  $\sim 2.1 \mu\text{m}$  in a hollow-core fiber filled with argon or ambient air. The supercontinua span over three optical octaves from  $\sim 280 \text{ nm}$  to  $2.7 \mu\text{m}$ , carrying a maximum of  $\sim 0.5 \text{ mJ}$  pulse energy. The unique combination of parameters makes the source readily suitable for exploitation in an infrared multi-color waveform synthesizer unraveling generation of energetic sub-cycle transients at  $\sim 1.9 \mu\text{m}$ .

### 3.1 Introduction to the topic

The rapid evolution of ultrafast pump-probe spectroscopy [89] and later of attosecond science [90, 3] over the last two decades stimulated tremendous progress in the generation, characterization and exploitation of the intense ultrashort light pulses. Discovery of nonlinear compression of mJ-level near-infrared pulses in noble-gas-filled hollow-core fibers (HCF) [91, 30, 29] pushed the frontier of the achievable pulse duration to merely a cycle of an oscillating electric field in early 2000s [92, 34, 35, 93].

Nowadays a number of applications [3, 12] demand those ultrashort light bursts to carry lower photon energies (in comparison to the Ti:Sapphire  $\sim 800 \text{ nm} \approx 1.5 \text{ eV}$ ) in order to avoid material damage and to control strong nonlinearities. Yet, the sources delivering CEP-stable near-single-cycle pulses with sufficient pulse energies in the infrared (IR)

spectral range are still rather unique. The essential prerequisite for their development is availability of an ultra broadband spectra, spanning preferably over several optical octaves, that are nontrivial to synthesize.

Due to the lack of the amplification media, the OPCPA approach is not able to support the spectra exceeding an optical octave, the up-to-date reported schemes for a generation of extreme broadband spectra in the infrared include: i) filamentation of the few-cycle mid-infrared pulses in bulk and gaseous media [49, 47, 94, 95, 48] and ii) nonlinear pulse compression in noble-gas-filled HCF [96, 97, 98] and photonic-crystal-fibers (PCF) [99].

Filamentation in bulk, as well as nonlinear pulse compression in PCFs, generates CEP-stable multi-octave spectra from the ultraviolet to infrared. However, the available pulse energy is limited to a tens of  $\mu\text{J}$  meaning that for many applications a consequent amplification is required. Filamentation in gaseous media yielded a spectacular mJ-level supercontinuum, though, the discussion of the CEP-stability was, unfortunately, avoided [47].

The use of noble-gas-filled HCF for spectral broadening of high-energy ( $\sim 1\text{--}2$  mJ scale) ultrashort pulses is well explored in near infrared and remains advantageous in the longer wavelength. Despite the lower nonlinear refractive indices of the noble gases in the infrared spectral range, scaling of the filamentation critical power  $P_{cr}$  as  $\sim \lambda^2$  and increased length of the light-matter interaction in the waveguide permit a dramatic spectral broadening of multi-mJ infrared pulses.

In this chapter I present a generation of multi-octave CEP-stable supercontinua via the nonlinear pulse compression of mJ-level few-cycle pulses centered at  $\sim 2.1$   $\mu\text{m}$  in argon- and ambient-air-filled hollow-core glass capillary. The maximum transmitted energy reaches  $\sim 0.5$  mJ with about 20% of the infrared energy transferred into the 280 nm – 1.4  $\mu\text{m}$  spectral range. The demonstrated spectra support 1.55 fs FTL (Fourier-transform-limited) sub-cycle transients and are well suited to enable sub-mJ multi-channel multi-color infrared waveform synthesis.

## **3.2 Experimental set up and results**

The input infrared pulses are produced by a CEP-stable multi-stage OPCPA reported in [ ] and described in additional details in Chapter 2. For the generation of the required supercontinuum we used two different OPCPA architectures.

### **3.2.1 The state of affairs before the start of the current work - 0.5 mJ OPCPA**

The proof of the principle experiment was first performed by Dr. Alex Schwarz and I am personally sincerely thankful to him for his work. The next two paragraphs reproduce the essence of the experiment.

In the first OPCPA architecture a 1.5 mm thick bulk lithium niobate  $\text{LiNbO}_3$  was used for the amplification in the second stage, due to an unavailability at the time of

a PPLN crystals in large apertures and with good poling quality. Lithium niobate was able to provide a required energy scalability allowing to reach  $350 \mu\text{J}$  pulse energy. As the phase-matching of the bulk crystal is inferior to its poled counterparts, the amplified bandwidth is limited, however, still sufficient to support sub-three-cycle 16 fs FTL pulses. In order to further push the pulse energy, the amplification bandwidth of the OPCPA was cut. The seed pulse was stretched to the duration exceeding the duration of the pump pulse. In that case the amplification bandwidth is defined by the overlap between pump and overstretched seed pulse and it is possible to tune the central wavelength by scanning the pump pulse through the seed pulse. Limiting the bandwidth additionally increases the efficiency of the AOPDF (DAZZLER), so both stages benefited from the enhanced seeding as well as less phase-mismatch and better temporal overlap of pump and seed pulses. It was possible to push the output of the second stage to over 0.5 mJ energy. DAZZLER-assisted compression in bulk Si yielded  $\sim 40$  fs (sub-six-cycles) 0.5 mJ pulses.

The entire beam was focused with a 750 mm  $\text{CaF}_2$  lens and coupled into a  $200 \mu\text{m}$  diameter 340 mm long HCF filled with argon. The capillary housing is sealed on each side with 1 mm thick  $\text{CaF}_2$  Brewster windows. The DAZZLER settings were adjusted to compensate for the dispersion introduced by the entrance window. Thankfully to a superior OPCPA beam quality, transmission of the capillary reached 66 %. The spectral broadening in the HCF was scanned over argon pressure, Fig. 3.1a. The spectrum of the emerging supercontinuum was monitored using two intensity-calibrated fiber-coupled spectrometers: the spectrum in the range 250 nm – 1100 nm was recorded with silicon charged-coupled device (CCD) spectrometer (Ocean Optics, Maya Pro); in the range 1200 nm –  $2.5 \mu\text{m}$  – with InGaAs CCD spectrometer (Ocean Optics, NIRQuest256). Around the spectrometer overlap region at  $1 \mu\text{m}$  (gray area in Fig. 3.1, both spectrometers are quite insensitive, therefore the exact spectral shape is less certain).

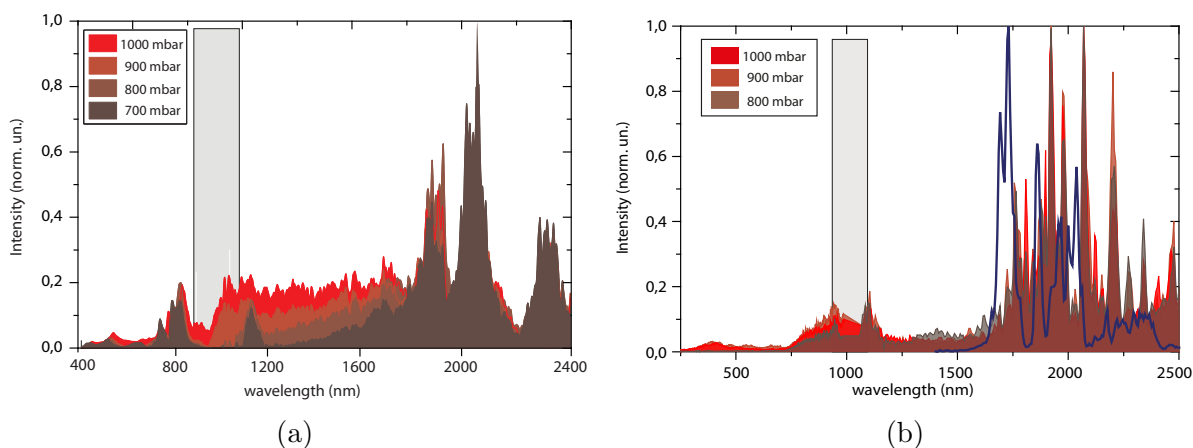


Figure 3.1: Pressure scan. (a) 0.5 mJ sub-six-cycle OPCPA in  $200 \mu\text{m}$  diameter HCF; (b) 1.1 mJ sub-two-cycle OPCPA in  $320 \mu\text{m}$  diameter HCF.

At the working pressure of 1000 mbar the supercontinuum spans from  $\sim 400$  nm to  $\sim 2.5 \mu\text{m}$  (and possibly beyond) with almost uniform intensity between  $1 \mu\text{m}$  and  $1.9 \mu\text{m}$ ,

thus, continuously covering nearly-three optical octaves.

Note how at low pressures self-phase modulation, 3rd and the 5th harmonic start building up. With increasing gas pressure, the fundamental and third harmonic are broadened and finally their spectral components will merge.

### **3.2.2 1.3 mJ OPCPA**

The promising initial results of spectral broadening provided an impulse to upgrade the driving source. The second architecture used for the consequent experiments is a three stage OPCPA described in the Chapter 2. The front end delivers  $\sim 1.3$  mJ  $\sim 11$  fs pulses.

After several reflections on gold and silver turning mirrors, the beam is focused with a  $f = 1500$  mm silver mirror and 1.1 mJ energy is launched into a  $320 \mu\text{m}$  diameter 340 mm long hollow-core fiber filled with argon. Identical to the previous experiment, the capillary housing is sealed on each side with 1 mm thick  $\text{CaF}_2$  Brewster windows. Regrettably, due to a slightly inferior beam quality of the three-stage architecture compared to the two-stage OPCPA, transmission of the capillary is only  $\sim 50$  %. In order to have a comparison with the results achieved with the first architecture, the spectral broadening at different gas pressures was recorded, Fig. 3.1b.

At the working pressure of 1000 mbar, the supercontinuum spans from  $\sim 280$  nm to  $2.5 \mu\text{m}$  and beyond (the detection is limited by the spectral coverage of the InGaAs spectrometer) – more than three optical octaves. About 5 % of the infrared energy is transferred into the 280 nm – 600 nm spectral region, while other 17 % are contained in the 600 nm –  $1.4 \mu\text{m}$  band. The spectral regions 280 nm – 750 nm and 750 nm –  $1.5 \mu\text{m}$  have almost uniform intensity, allowing the supercontinuum to be plotted on a linear scale.

In both cases of broadening in Ar, for the pressures beyond 1000 mbar - 1100 mbar the blue and ultraviolet components of the supercontinua become more pronounced. However, the output mode and stability deteriorates possibly due to the strong self-focusing and the rise of filamentation. The limitation could be circumvented by switching to a gas with higher ionization potential, for instance neon. Yet, achieving the similar or better broadening will require at least a factor of two higher gas pressure, thus jeopardizing the mechanical stability of the capillary. Changing the entrance windows to 2 mm thick  $\text{CaF}_2$  will introduce substantially more dispersion to the ultraviolet region of the spectra that is highly undesirable.

Considering that the nonlinear refractive index of ambient air is similar to the one of argon, we have endeavored to attempt the spectral broadening of the 1 mJ,  $\sim 11$  fs pulses in a HCF filled with the ambient air. The HCF remained in the housing, yet, the  $\text{CaF}_2$  Brewster windows were removed. After fine-tuning of the DAZZLER settings to compensate for the removed entrance Brewster window and adjustment of the fiber position along the focus, the generation of a spectacular ultra broadband supercontinuum similar to the one recorded in Ar was observed. However, inability to fine-tune the gas pressure substantially lowered the day-to-day reproducibility of the generated continuum. In order to stabilize the process,  $320 \mu\text{m}$  core diameter HCF used for the broadening in Ar was substituted with a  $270 \mu\text{m}$  HCF. That allowed to substantially improve the beam

pointing stability and increase the effective nonlinearity, combined action of both enabled generation of a supercontinuum in the Fig. 3.2. Yet, the capillary transmission fell to  $\sim 30\%$ . Implementation of an active beam pointing stabilization will resolve the issue.

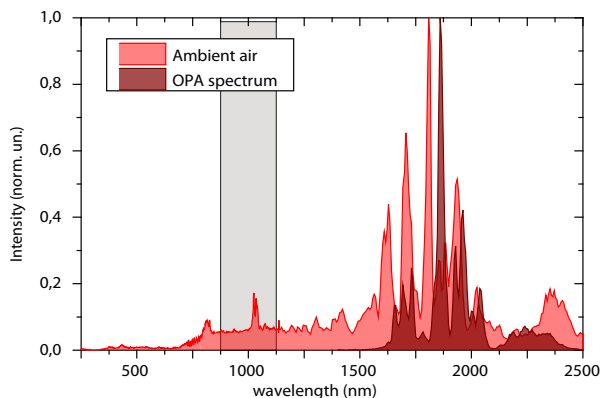


Figure 3.2: Generation of multi-octave supercontinuum in the ambient air-filled HCF.

The spectral shapes of the supercontinua generated in Ar and Air are strikingly similar, however, in the latter case less of the infrared energy is transferred into the ultraviolet, visible and near infrared regions of the supercontinuum. Only  $\sim 3\%$  of the energy is transferred into the ultraviolet-visible range, while still about 15% goes to the visible-near infrared. Nevertheless, both supercontinua support  $\sim 1.55$  fs FTL pulses – a sub-cycle transient at the central wavelength of  $\sim 1.9 \mu\text{m}$ .

Decomposition of such a broadband spectrum into individual bands with a subsequent compression with, for instance, dispersive mirrors [31, 100, 101] (possibly complemented by amplification) and re-combination is known as a parallel waveform synthesis [56, 61, 60, 58]. Seeded by the generated supercontinuum, the waveform synthesis scheme facilitates the production of sub-cycle transients at the central wavelength of  $\sim 1.9 \mu\text{m}$ .

### 3.3 CEP-stability

For the application to the ultrafast time-resolved field-sensitive measurements, CEP stability becomes even more critical than the number of cycles underneath the envelope. Therefore, inherently CEP-stable sources (like those derived from an intrapulse difference frequency generation) are a perfect light source for the spectral broadening. However, the phase needs to be preserved in the process. In order to evaluate the pulse-to-pulse CEP stability of the continuum generated we performed a standard collinear  $f - 2f$  interferometric measurement. A part of the spectrum was frequency doubled in a  $100 \mu\text{m}$  thick type-I BBO. The stability of the fringes was recorded over 1200 s, Fig. 3.3. The CEP jitter reconstructed from the measurement is  $\sim 200$  mrad. The CEP fluctuations are strongly coupled to the beam pointing. With the beam pointing stability deteriorating

### 3. Generation of a multi-octave phase-stable supercontinuum in ambient-air- or argon-filled hollow-core fiber

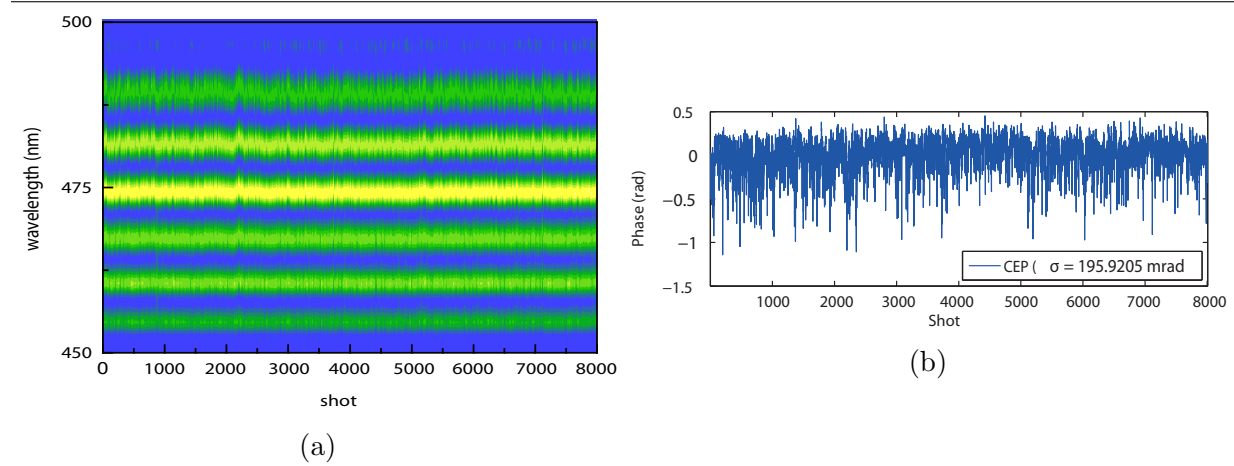


Figure 3.3: (a) Recorded  $f-2f$  fringe pattern over 1200 s; (b) recorded phase noise.

over time, the jitter surges to  $\sim 440$  mrad and beyond. As it was mentioned before, the implementation of an active beam pointing stabilization should improve the operation.

## 3.4 Conclusions and outlook of Chapter 3

We achieved the generation of an ultra broadband supercontinuum spanning over three optical octaves from  $\sim 280$  nm in the ultraviolet to  $2.5 \mu\text{m}$  and beyond in the infrared via nonlinear spectral broadening of mJ-level pulses in a argon- and ambient air-filled hollow-core fiber. The continuum is CEP stable and has a smooth, well behaved spectral phase, thus enabling its compression with assistance of, for instance, chirped multilayer mirrors. Well suited to seed a multi-channel waveform synthesizer, it facilitates generation of infrared sub-cycle sub-mJ transients, as well as development of a multi-color ultrafast source for a range of spectroscopic and imaging applications.

# Chapter 4

## Advanced multilayer thin–film dielectric coatings for versatile dispersion management

This chapter is largely adapted from O. Razskazovskaya, F. Krausz, V. Pervak ”Multilayer coatings for femto- and attosecond technology”, *Optica* 4, 2017, [101]. It introduces concept, design approaches and implementation specifics of the advanced dispersive thin–film multilayer optics that was developed for dispersion management of the ultra broadband supercontinuum generated in the Chapter 3 under the architecture of multi–channel waveform synthesizer described in details in Chapter 5.

### 4.1 Introduction and historical overview

Within the last two decades dispersive dielectric multilayer mirrors (DM) have played a significant role in the progress of ultrafast science. Their ability to manipulate the phase of a light pulse has advanced synthesis of intense femtosecond optical pulses followed by remarkable progress in the disciplines of nonlinear optics.

The quest for ever-shorter pulses started shortly after the first laser was demonstrated [70] and rapidly led to sub-100-fs pulses by passively mode-locked dye lasers [14, 15, 16, 17, 18]. After a reign of two decades, femtosecond dye lasers were replaced by Kerr-lens-mode-locked Ti:Sapphire lasers, in which self-phase modulation and group-delay dispersion (GDD) control by a pair of prisms allowed the pulse duration to approach [19, 20] and surpass the 10-fs regime for the first time [102]. Uncompensated higher-order dispersion was found to be the limiting factor in further pulse shortening [103, 102], while the delicacy of the prism arrangement challenged the reproducible operation. Replacing the prisms with aperiodic multilayer resonator mirrors with tailored group–delay dispersion [31], which became known as chirped mirrors, allowed these limitations to be overcome. With their use, Stingl and co-workers [21, 23] demonstrated the generation of highly stable sub-10-fs optical pulses from a Kerr-lens mode-locked Ti:Sapphire oscillators.

The main operational principle that defined the functionality of the first chirped mirrors and continues to have larger impact is so called "penetration effect" [31]. The layer stack of the conventional Bragg reflector is modified in such a way, that the thickness of the individual layers is gradually increasing through the stack with thinner layers being closer to the incident medium and thicker layers – closer to the substrate. Thus, the stack appears to be "chirped". This creates a wavelength-dependent penetration depth for the different frequency components of the incident radiation, with shorter wavelength being reflected in the top layers of the structure and ,thus, earlier and longer wavelengths being reflected deep in the structure, thus, later. This difference in the travel time creates a wavelength dependent group delay (GD).

Alternatively, group delay variation may be introduced with Fabry-Perot-like resonant structures – or Gires-Tournois interferometer (GTI) – creating a wavelength-dependent storage time of the incident radiation [104]. Both effects may coexist to improve the performance. As the modern dispersive optics commonly bears the features of both sub-groups, the general term for multilayer mirrors is dispersive mirrors.

In the next decade after their invention, the capability of chirped mirrors to reflect light over a broad range of wavelengths with controlled phase combined with simplicity and high efficiency had been instrumental in advancing Ti:Sapphire oscillators to the few-femtosecond, few-cycle regime [22, 24, 25, 26, 27, 28]. By the mid. 2000s, nonlinear pulse compression of amplified pulses along with progress of dispersive mirror technology [32] extended the frontiers of ultrashort pulse generation to what has been believed to be an ultimate border – one cycle of the optical carrier wave. Advanced chirped-mirror-based ultrafast systems nowadays routinely deliver powerful near-single-cycle pulses [33, 35].

With the advent of the passive (non-amplifying) [56] and later active (amplifying) [59, 61, 58, 60] optical waveform synthesis (OWS), the dispersive mirror technology had to stand to new challenges. As the OWS relies on utilization of multi-octave supercontinua, the spectral coverage of the novel dispersive optics had to be extended from the decade long status Quo of visible spectral range into adjacent ultraviolet and infrared. In addition, since the synthesis is enabled by coherent re-combination of several individual color channels, the challenge of careful decomposition of the seeding multi-octave spectrum and consequent re-combination of the individual wavepackets had to be undertaken.

Here I start by addressing the problem of dividing multi-octave radiation into different spectral channels while preserving the spectral phase and amplitude distribution of the light wave and then move on to discuss the broadband dispersive multilayer mirrors required for GDD control over the individual spectral ranges. I give an overview of multilayer optics for the VIS and NIR range of Ti:Sapphire lasers and then address the advances that extend precision GDD control into the UV and towards the mid IR, essentially facilitating the functionality of the infrared waveform synthesizer presented in the Chapter 5.

## 4.2 Multi-octave group delay control

Independent of the specific scheme, OWS relies on seed pulses with ultra-broad spectral coverage, spanning preferably a couple of octaves or more. The spectrum is separated into several channels, of which each is treated individually. In the case of the passive scheme, each channel is compressed to near its Fourier-transform-limit (FTL) in a dispersive delay line, before being recombined to synthesize the transients. In active schemes, each wavepacket remains temporally stretched while being amplified in one or more OPA stages. In [105] Chia and co-workers suggested to maintain the individual channels slightly chirped until after the final recombination in order to decrease the peak intensity and thus reduce the B-integral. The ultra broadband dispersive mirror pair meant to compensate the dispersion of the combined waveform afterward. The laser-induced damage threshold of the final mirror pair still remains a concern.

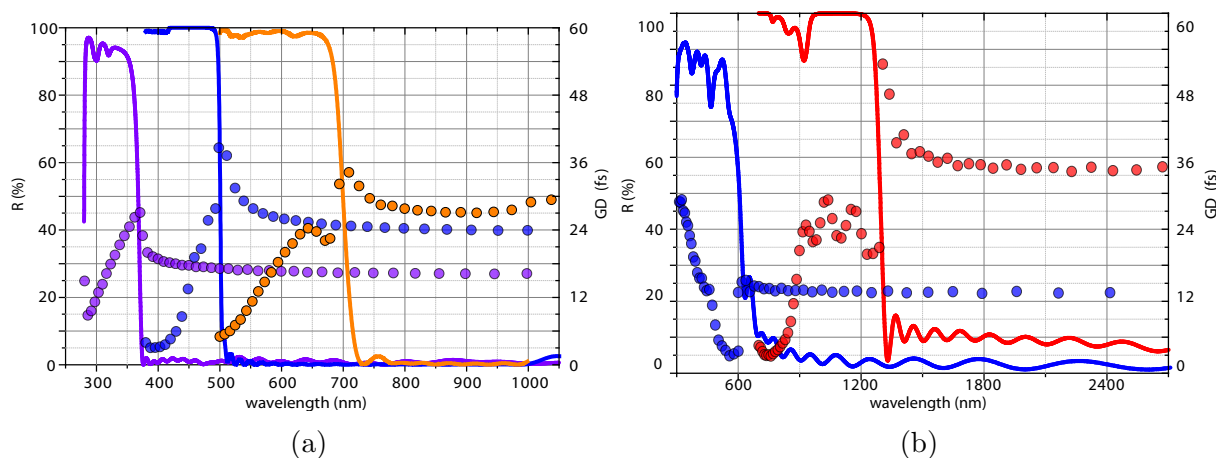


Figure 4.1: (a) A class of dichroic beam splitters for separation of ultraviolet, visible and near infrared bands in the passive synthesizer in [106]; (b) A class of dichroic beam splitters for separation of visible and near infrared bands in the passive and active synthesizers under development. Solid curves - designed reflectance, dotted curves - designed GD.

The channels of any OWS apparatus are initially separated with customized dichroic beam splitters (DBS). There are several major requirements to these key components: (1) a high contrast between reflected and transmitted light, (2) "cross-talk" region between channels, that is used for channel-to-channel synchronization and (3) smooth, well controlled (preferably flat) phase of *both* reflected *and* transmitted spectra in order to ensure compressibility of the individual channels. Fulfillment of all three requirements simultaneously is a formidable task [105]. Conventional DBSs are based on quarter-wave stacks of alternating high- and low-refractive-index dielectric layers. Their high-reflectance (HR) band is determined by the contrast between the refractive indices of the coating materials and is typically much narrower than the desired spectral span of the individual synthesizer channel. While exhibiting negligible GDD within the central region of their HR band, they are plagued by strong group delay (GD)/GDD ripples at the edges of the zone, intolerable

in applications for OWS. In order to extend the HR zone to the desired bandwidth and suppress dispersion ripples in the transition zones, the layer thicknesses are numerically optimized. The resultant slight detuning from a quarter-wave structure also creates the required "cross-talk" zones.

Beyond the above criteria, the DBSs of the OWS have to fulfill general requirements for mirrors used in demanding applications, such as the compensation for the tensile stress caused by the multilayer coating itself. In the case of an interferometric setup such as an OWS, this is particularly important in order to match the wavefronts of the individual channels and ensure their optimal superposition across the entire beam. This critical requirement is met by applying a compensatory coating on the back surface of the mirror substrate.

The designed reflectance and GD for the class of DBSs used for separating the UV, VIS-UV and VIS channels in OWS in [106] and VIS and NIR from IR in an OPA-based active OWS under development are presented in Fig. 4.1. The DBSs characterized by the curves in the Fig. 4.1 well fulfill the above mentioned major requirements demanded by OWS applications. (1) There is a high contrast between high reflectance and high transmittance zones yet (2) there are relatively narrow transition zones between the channels, and (3) the GD is smooth for both the high-reflectance and high-transmittance zones, even including the transition regions. These DBSs can be used for splitting as well as for recombining the beams.

### 4.3 Visible dispersive optics

Broadband dispersive multilayer mirrors in the VIS and NIR have matured over a couple of decades. In their first applications dispersive mirrors aimed at introducing constant negative GDD over a selected spectral range [107, 108]. Several design approaches have been applied to improve mirror performance [109, 110].

In the pursuit of near-single-cycle light, the required working bandwidth rapidly approached an optical octave [91, 30]. Under these conditions, control of GDD to the lowest order became insufficient for achieving transform-limited pulses and more sophisticated designs were needed. Double-chirped mirrors [54, 111, 112], complimentary mirror pairs [55] and double-angle mirrors [113] enabled significant extension of the bandwidth and simultaneous control over the higher-order dispersion. Evolution of the design tools and computational power have also been instrumental in the progress of the thin-film multilayer coatings for ultrafast optics [114, 115, 116].

As a result, the state-of-the-art chirped mirrors nowadays are able to operate over super-octave spectra and compensate the phase to an arbitrary dispersion order [117, 105]. However, the accurate initial definition of the dispersion target remains to be a major challenge for the development of broadband dispersive multilayers.

### 4.3.1 Phase compensation versus material compensation

The main goal of the dispersion management in the case of pulse compression is to compensate for spectral phase variations; therefore, precise control of it is of utmost importance. A major prerequisite is the accurate knowledge of the spectral phase to be compensated for. Several techniques have been developed for measuring this quantity, allowing – together with the spectral amplitude – complete characterization of the ultra short laser pulses [63, 62, 69]. Unfortunately, most of the techniques are not without shortcomings. These include the presence of ambiguities, insufficient temporal and/or spectral resolution and/or range, an inherent inability to measure the complete pulse intensity and/or phase, an inability to measure complex pulses, and artifacts due to multi-shot averaging over pulses with fluctuating characteristics [118]. As a result, the phase retrievals may be inconsistent and/or inaccurate and, thus, compromise the accuracy of the target for dispersive multilayer development (henceforth briefly: dispersion target).

Whenever the chirp carried by the laser pulse to be compressed is dominated by material dispersion, it may be more reliable to aim at canceling this material dispersion, which is well known. Therefore, in the material compensation approach, the dispersion target is chosen to compensate for the dispersion accumulated by the initially compressed pulse after propagation through known materials (incl. air). Since the optical constants of the commonly used optical materials and gases are well known, the resulting target can be calculated with a high accuracy, with the only remaining source of uncertainty being nonlinear effects.

Figure 4.2 presents two group-delay versus wavelength dispersion targets for mirrors to be used in the VIS spectral range. The material-based dispersion target (blue curve) in the Fig. 4.2 was designed to compensate for dispersion introduced by 2 mm of fused silica and 1 m of air with four bounces on double-angle dispersive mirrors. The phase-based target (red curve) was derived from a measured spectral phase. While the material-based target is clearly dominated by the second- and third-order dispersion, the phase-based target is noticeably influenced by the higher orders. These higher orders are likely inherited from the paternal nonlinear process, for example, broadening in a hollow-core fiber, or accumulated upon propagation due to induced nonlinearities.

In rare cases, when the accurate measurement of the spectral phase is hindered and compensation for material dispersion only does not yield the desired quality of compression, a hybrid approach may be helpful. In this case, the initial target is approximated by the known material dispersion. With the first set of dispersive optics produced in this way, the residual phase is either carefully measured or compensated for by a programmable dispersive filter [50, 119]. The new target is corrected for this residual phase. A dispersion target developed following the hybrid approach is presented in Fig. 4.3. The black curve in Fig. 4.3a is the initial dispersion target calculated to compensate for a particular amount of material dispersion in the optical system. After the first optics were produced and implemented, it was found that the blue edge of the spectrum (wavelength range 400 nm to 450 nm) required additional dispersion (red curve in Fig. 4.3a ). The new hybrid dispersion target was then designed to introduce the missing residual dispersion identified

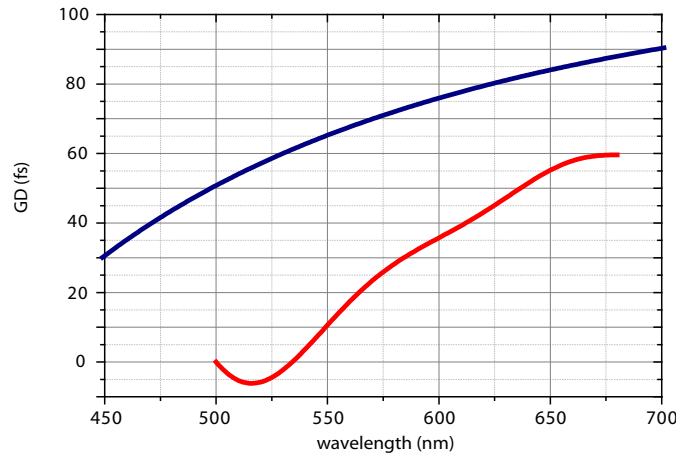


Figure 4.2: Dispersion targets developed based on phase compensation (red curve) and material compensation (dark blue curve) approach. The vertical offset is introduced for illustration purposes.

in the above procedure (blue curve). The reconstructed spectral phases of the ultrashort pulses achieved with material-only and hybrid approaches are presented in Fig. 4.3b. The spectral phase of the 6.1 fs pulse achieved via hybrid compression (blue curve) is noticeably flatter in the working spectral range than the spectral phase of the 15 fs pulse achieved with material compensation only, thus obviously yielding the better compression. The hybrid approach is powerful at the expense of increased time and material consumption.

The production of multilayers that precisely reproduce the dispersion target over the entire bandwidth is challenging. Dispersive multilayer coatings are very sensitive to deposition errors, as even slight changes in the layer thicknesses affect the spectral phase, so high-precision deposition techniques are required to ensure the reliable production. Magnetron and ion-beam sputtering are well-established processes for the production of dielectric multilayer optics for the VIS and NIR spectral ranges that offer higher accuracy and reproducibility than electron beam evaporation. Consequently, the coating materials are often chosen to be compatible with either of the methods.

The production of multilayers that precisely reproduce the dispersion target over the entire bandwidth is challenging. Dispersive multilayer coatings are very sensitive to deposition errors, as even slight changes in the layer thicknesses affect the spectral phase, so high-precision deposition techniques are required to ensure the reliable production. Magnetron and ion-beam sputtering are well-established processes for the production of dielectric multilayer optics for the VIS and NIR spectral ranges that offer higher accuracy and reproducibility than electron beam evaporation. Consequently, the coating materials are often chosen to be compatible with either of the methods.

The working spectral range of a thin film coating is defined by the transparency regions of the coating materials. A pair of layer materials with large contrast between their refractive indices is highly beneficial for broadband control of optical radiation. Currently,  $\text{Ta}_2\text{O}_5/\text{SiO}_2$  and  $\text{Nb}_2\text{O}_5/\text{SiO}_2$  are the two most commonly used material pairs for pro-

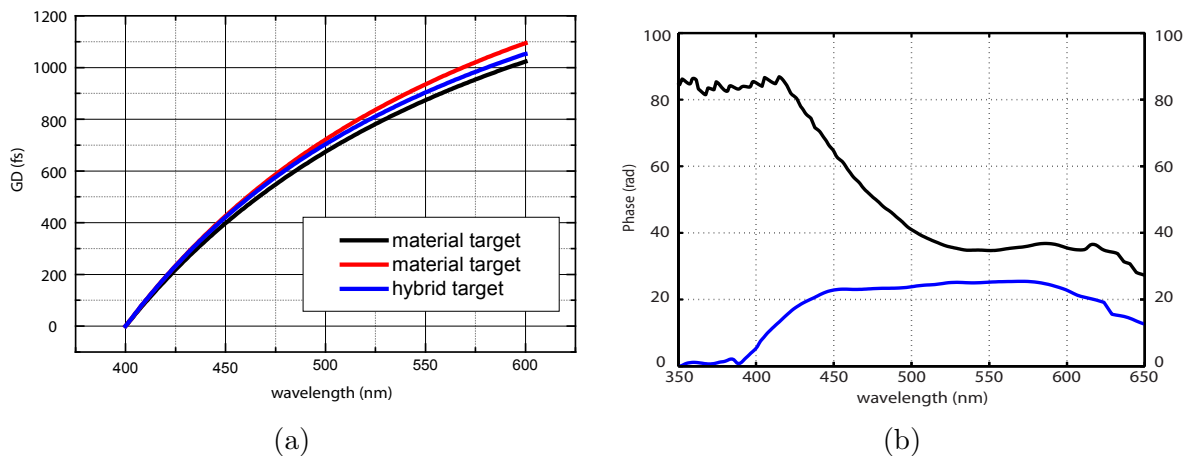


Figure 4.3: Hybrid dispersion target approach for the design of the visible and near infrared dispersive mirrors. (a) Hybrid dispersion target for the design of visible and near infrared dispersive mirrors; (b) pulse compression with hybrid target: black curve - spectral phase of the 15 fs pulse achieved with material compensation only, blue curve - spectral phase of the 6.1 fs pulse (FTL=6 fs) achieved with hybrid compensation.

duction of the dielectric thin-film coatings for VIS and NIR spectral ranges. Their low absorptance and high refractive index contrast (2.12/1.47 for  $\text{Ta}_2\text{O}_5/\text{SiO}_2$  and 2.28/1.47 for  $\text{Nb}_2\text{O}_5/\text{SiO}_2$  at 800 nm [120]) permit the production of multilayer structures with high-reflectance and low-loss in the VIS spectral range.

The multilayer mirrors following the dispersion targets in Fig. 4.2 were produced with the magnetron sputtering deposition process. The agreement between designed and measured characteristics demonstrates the reliability of the technology, Fig. 4.4. Upon implementation, both designs yielded well compressed nearly-transform-limited pulses. In the case of phase-based target – 6.5 fs (6.1 fs FTL), Fig. 4.4a, material-based target – 2.9 fs (2.7 fs FTL), Fig. 4.4b; therefore, validating the suitability of both approaches.

Overall, significant developments in the field of dispersive coatings stimulated by the demands of the ultrafast optics allow for a versatile and reliable dispersion management in the VIS and NIR spectral ranges.

## 4.4 Ultraviolet dispersive optics

For almost two decades after the first demonstration of dispersive multilayer mirrors [31], their evolution responded to the demands of Ti:Sapphire-based systems, with little effort being invested into the extension of the technology into UV spectral range [121]. Generation of the synthesizer's spectrum via broadening of the femtosecond Ti:Sapphire pulses in a gas-filled hollow-core fiber [56, 106] gives rise to a significant extension of the spectral range into the UV. Consequently, it is possible and – for many applications desirable – to extend the synthesizer's spectral coverage to the UV spectral range.

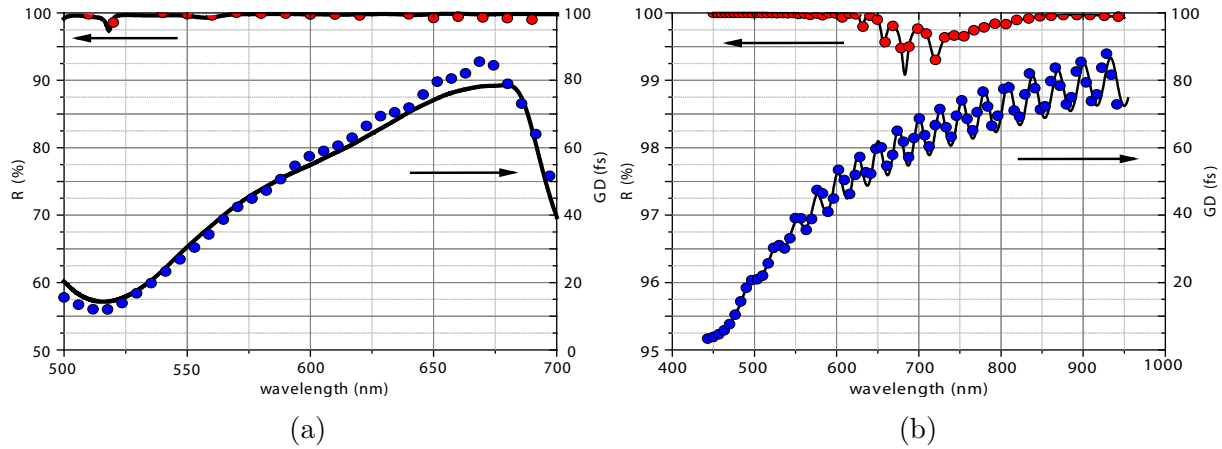


Figure 4.4: Dispersive multilayers in visible spectral range. (a) Dispersive multilayer developed upon phase compensation dispersion target; (b) dispersive multilayer developed upon material compensation dispersion target: black solid curves - designed reflectance/GD, dotted red curve - measured reflectance, dotted blue curve - measured GD.

UV is a notoriously difficult working range in terms of dispersion control for broadband radiation, because the refractive index and absorption rapidly increase as the frequency of the incident radiation approaches atomic resonances in the UV, resulting in strong dispersion and often non-negligible absorption over even relatively short propagation distances.

Manufacturing of precision dispersive multilayers in the UV is significantly more challenging. The physical thickness of the individual layers scales with the central wavelength, thus, it becomes smaller for shorter wavelengths, while the absolute deposition error remains approximately unchanged. Consequently, the relative error in layer deposition tends to be higher in the UV than in the VIS-IR range. As a result, electron-beam evaporation of the  $\text{HfO}_2/\text{SiO}_2$  material pair, the well-established standard technology for the production of high-reflectivity mirrors and filters in the UV, is unsuitable for manufacturing of dispersive optics for UV. The accuracy of this deposition technique entails intolerable errors for chirped multilayers in the UV. Fortunately, the deposition of this material pair has recently been adapted for magnetron sputtering [122] and ion-beam sputtering, enabling the deposition of layers with higher accuracy. This progress has been instrumental in extending broadband dispersive multilayers into the UV range. Another major challenge turned out to be the optical properties of the thin-film materials themselves.

#### 4.4.1 Induced nonlinear effects: establishing control over induced nonlinearities

This section of the thesis is largely adapted from O. Razskazovskaya et al. "Nonlinear absorbance in dielectric multilayers", *Optica* 2, 2015, [123].

Due to the extreme temporal and spatial confinement of the intense few-cycle pulses that are now commonly used for attosecond metrology, laser systems with moderate average

powers yield pulse peak intensities on the target in the order of petawatt ( $10^{15}$  W), thus allowing to enter the strong-field regime of nonlinear optics [124]. The ongoing development of broadband optical parametric amplifiers (OPAs) holds promise for further scaling of the achievable peak intensities [58, 61]. While the experiment is exposed to the petawatt level intensities, the optics of the delivering systems are driven in the terawatt ( $10^{12}$  W) regime, at which the response is dominated by low order bound electronic nonlinearities such as the second and third order processes, consequently making it a perturbative regime [124]. The appearance of the nonlinearities in bulk components such as lenses, windows etc. is well recognized and addressed in literature, however, the performance of the thin film coatings and DMs in particular, has hitherto been considered in linear domain only.

While developing the ultraviolet optics for the current project, we have observed for the first time a nonlinear response of the dielectric DMs. We have found that the complicated interference pattern within the DMs' multilayer stack causes certain distribution of the electric field inside the coating that gives rise to a very significant enhancement of the internal electric field. It is known, that multilayer structures like Bragg reflectors or resonant cavities and quantum wells are capable of enhancing the nonlinear response [125, 126, 127], however, even then the materials with relatively large nonlinear refractive indexes, mostly semiconductors and polymers [128, 129, 130, 131], are used in order to achieve reasonable scale of nonlinearity. In our case the enhancement becomes sufficient to trigger third order nonlinear optical processes in the dielectric materials of the multilayer that have orders of magnitude smaller nonlinear coefficients than common semiconductors/polymers, which indicates the significance of the enhancement factor.

We have also found that, in our case, two photon absorption (2PA) strongly dominates the observed nonlinearity, as the nonlinear response of the DMs emerges in the form of nonlinear absorbance, while the appearance of the optical Kerr effect – second manifestation of third order nonlinearity – is not evident.

Despite that at the first sight the observed nonlinearity appears to be unwanted only, as it impairs the performance of ultrafast system, authors see attractive and worthwhile applications, that will be discussed later.

Based on experimental data, we have developed a theoretical model that allows estimation of the coefficient of 2PA and consequently prediction and to some extent tuning of the intensity dependent absorbance of the coating. This gives an opportunity to not only re-establish the mirrors' operation, but a key for expanding the DM functionality into the nonlinear domain as well as for exploitation of DM as a new kind of nonlinear element suitable for advanced photonic applications.

#### 4.4.2 Experiment and Results

In our experiments we used intense sub-40 fs laser pulses, carried at central wavelength,  $\lambda_L$ , 400 nm to investigate the reflectance of a series of dispersive DMs, here and further denoted as Mx-series. The light source is an intense s-polarized frequency doubled output from a commercially available chirped pulse two-stage, multi-pass Ti:Sapphire amplifier. Second harmonic generation is realized in a thin BBO crystal yielding  $\sim 40$  fs up-chirped

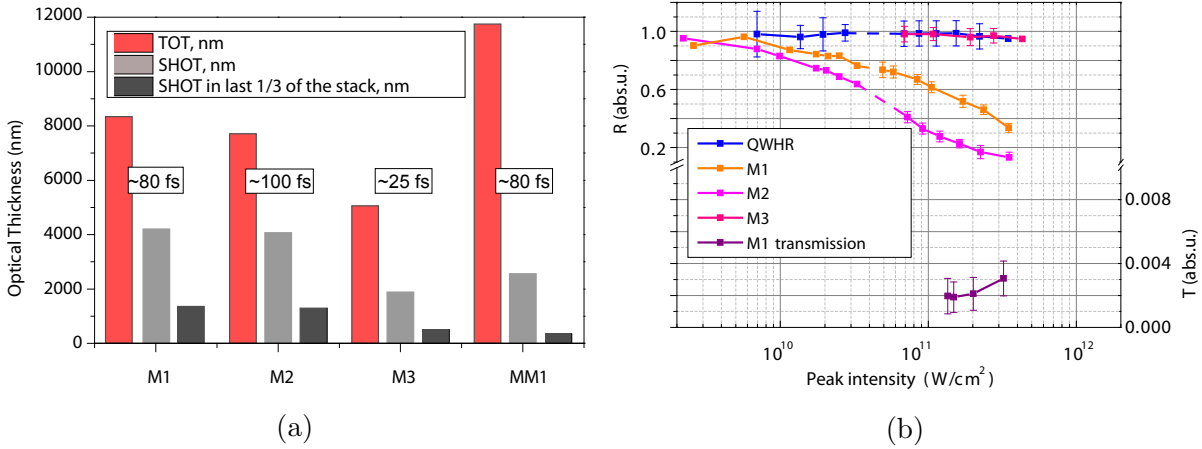


Figure 4.5: Intensity dependent reflectance of the series of the non-optimized DMs.(a)Relevant design data of the tested DMs. Mx refers to non-optimized DM, MMx-2PA-optimized design: red bar – total optical thickness of the multilayer stack in nm, light grey bar – sum optical thickness of H-index layers in nm, dark grey bar – sum optical thickness of H-index layers contained in upper 1/3 of the multilayer stack only; dispersive properties are represented by the value of introduced GD per reflection (in frame);(b) nonlinear response of the reflectance of the non-optimized D: solid lines are provided as a guidance to the eye, error bars represent instrumental error of the measurement.

pulses at the average power of 3 W at 3 kHz repetition rate. Step-wise attenuation of the light source power can be realized gradually down to 0.5 W without compromising temporal and spectral characteristics of the pulses by modulating the radio frequency signal power inside the Dazzler [50, 119]. With the implementation of the gentle focusing scheme, we were able to gradually adjust the incident peak intensity,  $I_p$ , in the range from  $\sim 3 \cdot 10^9$  W/cm<sup>2</sup> to  $\sim 2 \cdot 10^{12}$  W/cm<sup>2</sup>. This intensity range was chosen as it covers desired working range of the described mirrors which spans from 10<sup>10</sup> W/cm<sup>2</sup> to 10<sup>11</sup> W/cm<sup>2</sup>. Damage of the tested samples at intensities above  $3.5 \times 10^{11}$  W/cm<sup>2</sup> prevented data collection at higher intensities.

The mirrors of the Mx-series were designed for the wavelength range from 380 nm to 420 nm, though differed by the value of the introduced GD ranging from 25 fs (mirror M3) to 100 fs (mirror M2) (Fig. 4.5). The mirrors were produced out of the Ta<sub>2</sub>O<sub>5</sub>/SiO<sub>2</sub> material pair, Ta<sub>2</sub>O<sub>5</sub> was used as the high-index material whereas SiO<sub>2</sub> was the low-index material. Both materials are most commonly used for the production of coatings in the visible (VIS) spectral range, as the band gaps of Ta<sub>2</sub>O<sub>5</sub> and SiO<sub>2</sub> deposited by magnetron sputtering are  $\sim 4.2$  eV [132] and  $\sim 7.5$  eV [133, 74] respectively. Linear absorbance for Ta<sub>2</sub>O<sub>5</sub> single layer is estimated to  $\sim 0.8 \cdot 10^{-3}$ , for SiO<sub>2</sub>  $\sim 10^{-4}$ . The mirrors were coated on 25 mm diameter, 6.35 mm thick fused silica substrates transparent in VIS and near ultraviolet (NUV) spectral ranges by means of magnetron sputtering thin film deposition technology.

We observed that the DMs had an intensity dependent reflectance, i.e., the reflectance

of the DM decreased with an increase of the incident intensity (Fig. 4.5b). The observed effect was reversible, i.e., if the incident intensity was decreased, the reflectance instantly rolled back to previously recorded higher values (Fig. 4.6).

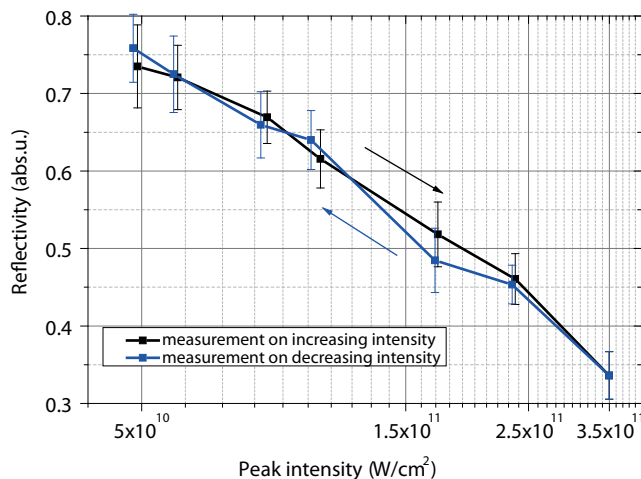


Figure 4.6: Reversibility of nonlinear response of the mirror M1. The error bars represent instrumental error of the measurement.

Obtained reflectance curves for the DMs of the series Mx are presented at Fig. 4.5b. The plots of the Fig. 4.5a, Fig. 4.5b show a clear dependence of the reflectance on the absolute value of the introduced GD. The less the absolute value of introduced GD per reflection is, the less pronounced the effect is. For instance, the nonlinear response of the mirror M3, introducing the least GD, is significantly weaker than responses of mirrors M1 and M2, introducing 80 fs and 100 fs GD respectively. Furthermore, we tested a quarter-wave high reflector (QWHR) mirror, produced out of the same material pair, that introduces virtually zero dispersion in the spectral range of interest, and did not observe any evidence of nonlinear behavior (Fig. 4.5b).

These observations can be interpreted if one considers the structure of the dielectric mirrors. As most DMs operate on the penetration effect [31] as a basic principle, a certain minimal optical thickness of the coating needs to be reached in order to introduce the desired value of GD [134]. The higher the desired value of GD, the thicker the coating is and thus the deeper the electric field penetrates into the multilayer, involving more of the coating material into the interaction. In addition to the penetration effect the presence of resonant cavities [104] creates “hot regions” inside the stack where electric field is strongly enhanced. Both effects together result in a complicated distribution of electric field within the stack (Fig. 4.7a) that is significantly different from the typical distributions in QWHR or single layers of identical optical thickness (Fig. 4.7b, 4.7c). Consequently, even relatively small nonlinearities get enhanced and become pronounced in DMs.

In general, nonlinearity of optical media can be described by intensity-dependent variations of the complex dielectric constant, or the complex refractive index. In particular,

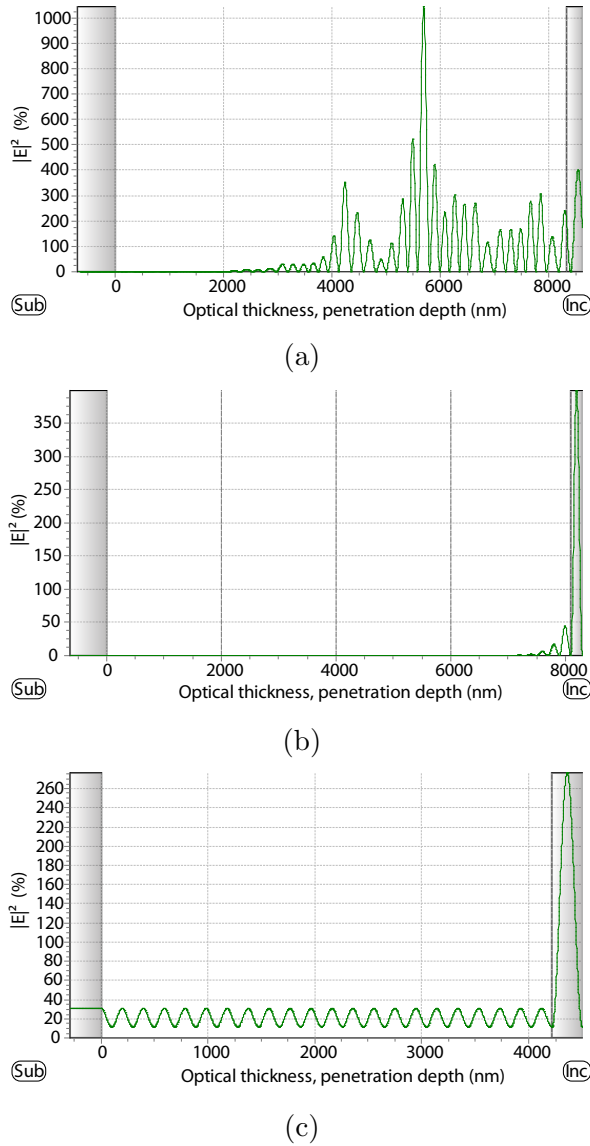


Figure 4.7: Values of the electric field are normalized to the amplitude of the incident electric field,  $E_a$ . (a) In DM M1. Due to the structure of the DM itself the electric field is enhanced; (b) in quarter-wave high reflector (QWHR); (c) in single layer of high-index coating material of identical optical thickness.

variations of the real part of the complex refractive index are related to Kerr-type non-linearity. Variations of the imaginary part of the complex refractive index (extinction coefficient) are related to the two-photon absorption (2PA) and can be described as an increase of the extinction coefficient proportionally to the electric field intensity. The appearance of 2PA absorption causes a noticeable increase of the losses, as the energy is converted to heat, while optical Kerr-effect induces change of the refractive index and thus modifies spectral phase. It is illustrated at Fig. 4.8 representing group delay dispersion

(GDD) characteristic of mirror M1 <sup>1</sup>.

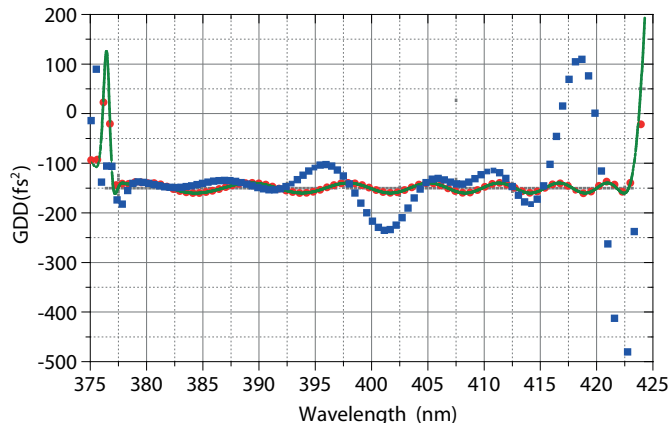


Figure 4.8: Impact of different types of nonlinearities on dispersive performance of mirror M1. Green bold line – simulated GDD curve in the range from 380 nm to 420 nm without impact of either changing nonlinear refractive index, or 2PA. Red dotted line – simulated GDD curve with the impact of 2PA, estimated spectrally averaged induced absorption is  $\Delta\alpha \approx 15.2 \cdot 10^2 \text{cm}^{-1}$ , blue dotted line – simulated GDD curve with impact of nonlinear refractive index  $\Delta n \approx 0.0025$  at corresponding intensity  $I_p = (3.5 \pm 0.7) \cdot 10^{11} \text{ W/cm}^2$ .

We performed thermal tests, where the surface temperature of the irradiated mirrors was directly measured by a thermal camera, and compared the data obtained for the DM M1 and the QWHR produced out of the same materials (Fig. 4.9). The measurements showed that the surface of the DM warmed up significantly more than that of the QWHR. This strongly indicated 2PA to be the leading cause of the reflectance change in our experiments.

As 2PA is believed to give the predominant contribution to appearance of the optical Kerr-effect [136], the appearance of strong 2PA should be accompanied by presence of non-zero nonlinear refractive index  $n_2$ . Still the transmittance of the coating has not evidently changed in all intensity range, staying well within the error of the measurements (Fig. 4.5b). This observation appears to be rather peculiar. However, the results of [136, 137, 138] demonstrate that there is a region in the range of photon energies,  $E_p$ , between direct band gap,  $E_g$ , and 2PA edge,  $0.5E_g$ , where nonlinear refractive index is nearly vanishing. This region corresponds to  $E_p \sim 0.75E_g$ . As the band gap of  $\text{Ta}_2\text{O}_5$  deposited by magnetron sputtering technique is an average in the range of 4.2 eV and our spectrum covers region from 380nm to 420 nm,  $E_p$  in our experiment fits quite well into the predicted range, where the  $n_2$  is nearly vanishing. That fully explains the lack of noticeable changes in  $n$ .

As we have concluded, that the nonlinear refractive index does not experience significant changes, the dispersive properties of the DM should not be affected, only the losses. Thus it

<sup>1</sup>For illustration purposes the change in GDD induced by Kerr-effect was simulated using nonlinear refractive index  $\Delta n$  at 800 nm [135].

is feasible to design a photonic device that demonstrates strong ultrafast nonlinear response to irradiance, while preserving its dispersive characteristics and thus the temporal profile of reflected pulse. For the realization of suggested device it is of main importance to be capable of predicting and possibly tuning the strength of the nonlinear response, in our case, the strength of 2PA. Following the conclusion that 2PA is the main cause of observed nonlinearity, we have developed a model that allows quantitative and qualitative simulation of the 2PA in thin film coatings and its subsequent applications.

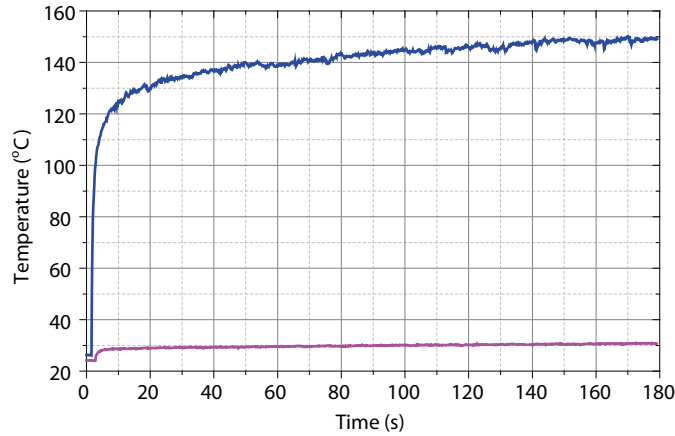


Figure 4.9: Blue bold line – surface temperature of irradiated mirror M1, pink bold line – surface temperature of QWHR. Incident intensity is  $I_p = (3.5 \pm 0.7) \cdot 10^{11} \text{ W/cm}^2$ .

### 4.4.3 The model

We simulated 2PA in multilayer mirrors as an induced extinction coefficient proportional to the squared electric field amplitude modulus:  $\chi(z) = \beta|E(z)|^2$ , where  $z$  is the coordinate along mirrors' cross-section. Due the fact that the band gap of  $\text{SiO}_2$  is significantly wider than the band gap of  $\text{Ta}_2\text{O}_5$ , we considered an induced extinction coefficient in the  $\text{Ta}_2\text{O}_5$  layers only. While ideally one has to perform this nonlinear interaction step in time domain, we found out that in the case of slowly varying pulses containing  $\geq 30$  full optical cycles, the pulses are long enough so that the treatment in frequency domain can be utilized. Our sub-40 fs pulses centered at 400 nm are ideal for implementation of such model. Moreover, consideration in frequency domain also provides substantial boost in computational efficiency inheriting successful software packages in multilayer design [?].

Although the values derived from our implementation, as a consequence of the above considerations, are restricted to our specific laser pulses, the approach to the treatment of 2PA in terms of induced extinction coefficient, that is suggested here, is universal and can be applied to virtually all possible cases.

Specifically, similar to [139], pp. 4-11 the initial system of Maxwell equations describing interaction of s-polarized light with the multilayer mirror can be reduced to a boundary-

value problem for a system of two nonlinear ordinary differential equations.

$$\frac{du}{dz} = ik\nu \quad (4.1a)$$

$$\frac{d\nu}{dz} = ik(\tilde{n}(z, u) - \alpha^2)u, \quad 0 < z < z_a, \quad (4.1b)$$

$$\tilde{n}(z, u) = n(z) - i\beta|u(z)|^2 \quad (4.1c)$$

$$(\nu - q_s u)|_{z=0} = 0 \quad (4.1d)$$

$$(\nu + q_a u)|_{z=z_a} = 2q_a E_a \quad (4.1e)$$

Here  $k = 2\pi/\lambda = \omega/c$  is the wavenumber,  $u(z)$  and  $\nu(z)$  are tangential amplitudes of the electric and magnetic fields, respectively,  $n(z)$  is the refractive index profile describing the mirror structure. The coordinate  $z=0$  corresponds to the boundary between the coating and the substrate, the coordinate  $z=z_a$  corresponds to the boundary between the coating and ambient medium. Parameters  $\alpha$  and  $q_s, q_a$  are defined as  $\alpha = n_a \sin\theta$ ,  $q_{s,a} = (n_{s,a}^2 - \alpha^2)^{1/2}$ , where  $n_s$  and  $n_a$  are refractive indices of the substrate and ambient medium,  $\theta$  is the angle of incidence and  $E_a$  is amplitude of the electric field. The reflectance can be determined as a ratio of reflected wave intensity to the intensity of the incident wave, that leads to

$$R(k, E_a) = \left| \frac{q_a u(z_a, k) - \nu(z_a, k)}{q_a u(z_a, k) + \nu(z_a, k)} \right|^2 \quad (4.2)$$

Note, that due to the nonlinearity of Eqs. 4.1 the reflectance is dependent on the incident wave amplitude. Since the Eq. 4.2 is invariant with respect to multiplication of  $u, \nu$ , and  $E_a$  by  $\exp(i\phi)$ , it is sufficient to study the dependence of  $R(k, E_a)$  on the real valued  $E_a$  parameter. The dependence of the simulated reflectance Eq. 4.2 for the mirror M2 versus the intensity of the incident light is shown in Fig. 4.10 for  $\beta = 10^{-6}$ . All dependencies are represented with respect to arbitrary intensity. The solid blue curve in Fig. 4.10 represents the reflectance at the wavelength 400 nm. The reflectance drop is noticeably dependent on the wavelength: the dashed–magenta and the dashed–green curves represent the reflectance at 410 and 390 nm, respectively.

We consider irradiating pulses with spectral distribution having full width at half maximum (FWHM) of 14 nm around the central wavelength 400 nm. For relatively long or/and significantly chirped pulses with slowly varying amplitude the model Eq. 4.1-4.2 remains valid with sufficient accuracy. In order to take into account the fact that different spectral components of the pulse have different intensities, and as a result have different reflectance due to 2PA non–linearity, we introduce effective reflectance corresponding to the specified pulse. As the drop of input intensity for wavelengths deviating from the central wavelength of 400 nm obviously leads to the corresponding increase of the reflectance, the effective reflectance is higher than reflectance at the central wavelength, where the intensity of

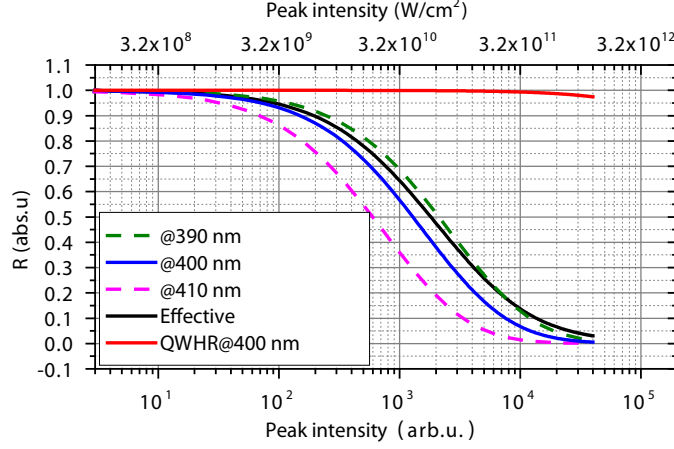


Figure 4.10: Blue curve, dashed-magenta and dashed-green curves are reflectance at 400, 410, and 390 nm, respectively. Black curve is the effective reflectance integrated with respect to Gaussian spectrum with the center at 400 nm. For comparison the effective reflectance of a 35-layer quarter-wave mirror with central wavelength 400 nm is also shown (red curve). Top x-scale is relevant peak intensity in SI units calculated via multiplication of peak intensity in arb.u. by  $G^2 = (3.2 \pm 0.3) \cdot 10^7$  fitting factor.

the incident light possesses a maximum value. For simplicity we assumed the spectral distribution of intensity having a Gaussian shape

$$I_a(k) = \frac{I_0}{\Delta\sqrt{2\pi}} \exp\left(-\frac{(k - k_0)^2}{2\Delta^2}\right) \quad (4.3)$$

where  $\Delta$  in Eq. 4.3 is defined by the FWHM of the pulse spectrum and for  $k_0 = 2\pi \cdot 25000 \text{ cm}^{-1}$ , corresponding to the central wavelength of 400 nm, is equal to  $2\pi \cdot 371 \text{ cm}^{-1}$ . The resulting effective reflectance can be obtained as

$$R(I_0) = \frac{1}{\Delta\sqrt{2\pi}} \int R(k, E_a) \exp\left(-\frac{(k - k_0)^2}{2\Delta^2}\right) dk, \quad (4.4)$$

where we additionally assumed that the  $E_a$  is equal to the square root of the dimensionless incident light intensity:  $E_a = \sqrt{I_a(k)}$ . The black curve in Fig. 4.10 corresponds to the effective reflectance Eq. 4.4. Due to the essentially non-linear origin of 2PA, the effective reflectance does not belong to the area between reflectance curves for 390 nm and 410 nm. Even more, because of spectral integration the decrease of the reflectance is less pronounced and it occurs at higher values of the incident light intensities comparing to monochromatic cases. Note that at Fig. 4.10 integrated reflectance is higher than reflectance at 390, 400 or 410 nm when arbitrary light intensity is higher than  $10^4$ . For comparison we also presented effective reflectance of a 35-layer quarter-wave mirror for the central wavelength 400 nm. This quarter-wave mirror exhibits nearly no noticeable decrease of the reflectance at the same levels of the incident light. To better illustrate the physical mechanism of the induced extinction coefficient influence on the resulting reflectance values we calculated its profiles

for the wavelengths 390, 400, and 410 nm (Fig. 4.11). The profile for the wavelength 400 nm was calculated for the intensity providing 20% reflectance. This intensity is equal to  $\approx 4.2 \cdot 10^3$  arb.u. (Fig. 4.10). Two other profiles for the wavelengths 390 and 410 nm were calculated for the same intensity level that resulted in reflectance values equal to 0.314 and 0.071, respectively. One can clearly see the correlation between penetration depth of the induced extinction coefficient and the value of the reflectance.

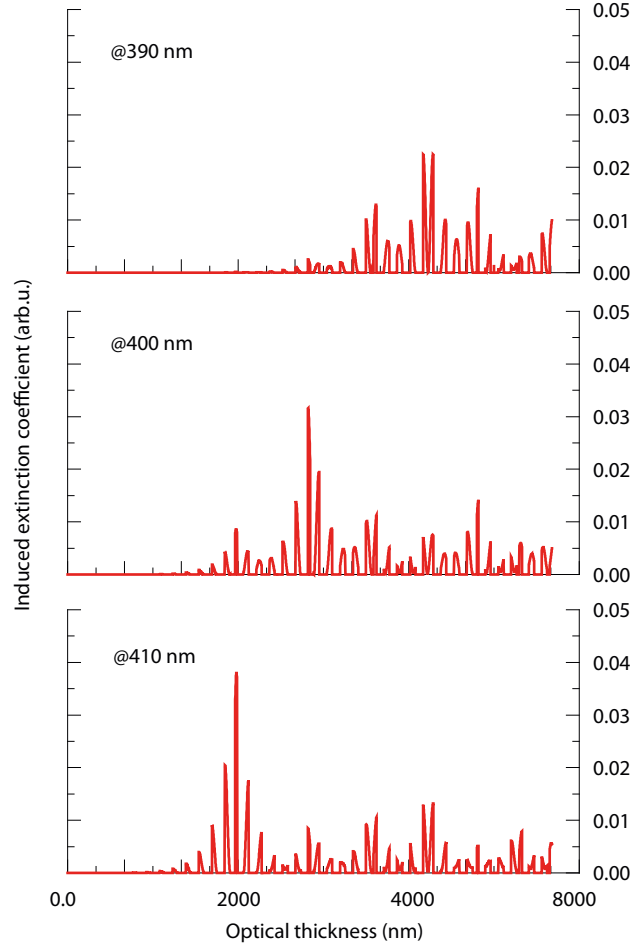


Figure 4.11: Distributions of the induced extinction coefficient  $\beta|E|^2$  in the mirror M2 cross-section for wavelengths values: 390, 400, and 410 nm.

Since the reflectance  $R(k, E_a)$  Eq. 4.2 is obviously independent with respect to scaling of  $u$  and  $\nu$  by a factor  $G$  and simultaneous decrease of  $\beta$  by the factor of  $G^2$ , the obtained results can help to estimate the value of  $\beta$  by fitting the experimental data. At low intensities mirrors are illuminated with a collimated beam, while at high intensities, where the focusing scheme is implemented, the iris is used to select the most intense part of the beam; therefore it is possible to assume flat-top spatial distribution across the beam spot. In this case the electric field  $E_a$  [V/m] is connected with incident light intensity

$I$  [W/cm<sup>2</sup>] with the relation  $E_a = 10^2 \sqrt{2I\eta_0}$ , where  $\eta_0 \approx 376.7$  Ohm is the impedance of vacuum. A good fit of the experimental data related to the mirror M2 is obtained with  $G^2 = (3.2 \pm 0.3) \cdot 10^7$  (Fig. 4.12a) and as a result the estimate of  $\beta$  in SI units is  $\beta_{si} \approx \beta / (20000\eta_0 G^2) = (4.1 \pm 0.4) \cdot 10^{-21}$  [m<sup>2</sup>/V<sup>2</sup>]. The obtained value of 2PA coefficient seems to be rather high, but no numerical values of the 2PA coefficient were found in the literature. We can compare 2PA value with other oxides. For this purpose it is necessary to convert obtained value to one more appropriate for 2PA measurement:

$$\alpha_2 = 8\pi\eta_0\beta_{si}/(n_{Ta_2O_5}\lambda). \quad (4.5)$$

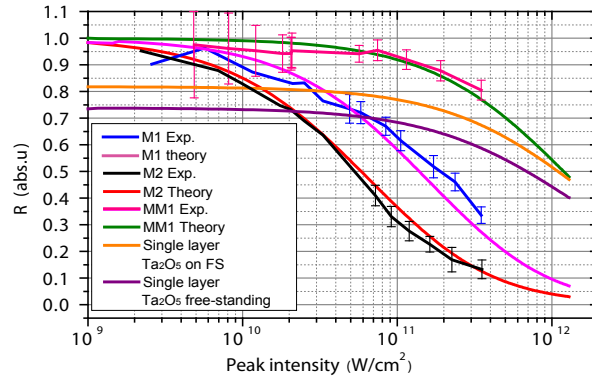
The estimation of the corresponding  $\alpha_2$  value results in  $\alpha_2 = (4.35 \pm 0.5) \cdot 10^{-9}$  [cm/W]. It is noticeably higher than similar values for Al<sub>2</sub>O<sub>3</sub> ( $\approx 0.09 \cdot 10^{-9}$  [cm/W] [140]) measured at 264 nm. On the other hand the corresponding value for TiO<sub>2</sub> is significantly higher [141]:  $\alpha_2 = (15 \div 19) \cdot 10^{-9}$  [cm/W]. It is also necessary to take into account that literature data is mainly related to bulk materials, while the optical properties of thin film materials may significantly differ from the bulk ones. To cross-check the obtained value, we compared the theoretical reflectance of the mirror M1, predicted with the same value of  $\beta$  taken into account, to the experimental data (magenta and blue curves in Fig. 4.12a). The results demonstrated a convincing correspondence.

In order to confirm, that it is the enhancement that plays the major role in the observed nonlinearity, we additionally estimated the theoretical transmittance of a single layer of Ta<sub>2</sub>O<sub>5</sub>. The single layer has an optical thickness equal to the sum optical thickness of all H-index layers (SHOT) contained in M2 mirror stack Fig. 4.5a, and is either free standing or deposited on the fused silica substrate, identical to mirrors' substrates. The obtained curve (Fig. 4.12a) indicates that enhancement of the internal field reached in DM is indeed of major importance, as the reflectance drop of the single layer is significantly less than those simulated and measured for DMs M1 and M2.

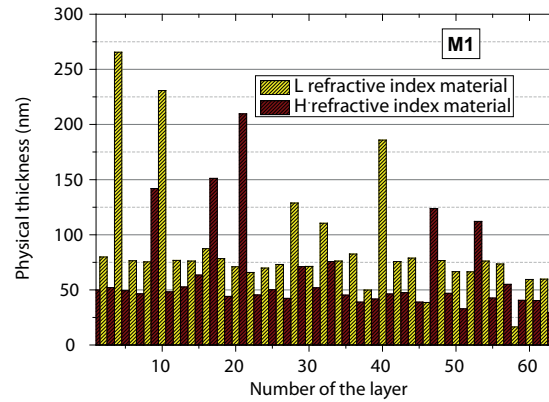
#### 4.4.4 Implications

The nonlinear absorbance of the coating can be tailored, if along with the coefficient of the linear absorbance,  $\alpha$ , the nonlinear extinction coefficient  $\beta$  is taken into account and implemented into the already adopted DM design approaches [116, 114, 115]. However, design optimization will require multiple solutions of non-linear problems and is rather time-consuming for conventional calculations. As a simpler approach, we have estimated effective induced nonlinear absorption at the highest level of working intensity and introduced linear absorbance of the similar value in high-index layers. It allowed us to develop a new series of 2PA-optimized DMs using conventional multilayer design techniques.

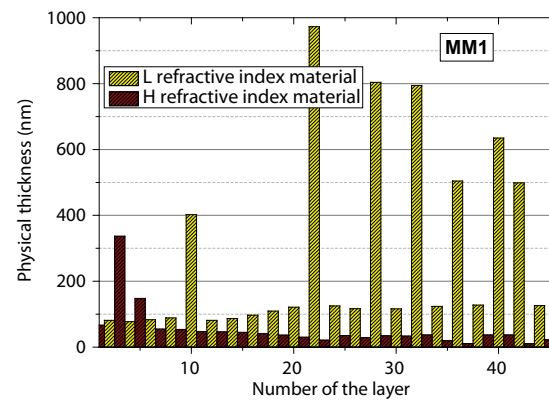
As in this particular case, we were interested in developing device with the dispersion characteristic similar to M1, while achieving the highest possible reflectance, the new 2PA-optimized design targeted minimization of the 2PA. The detailed data of the new mirror, MM1, are summarized in Fig. 4.5a. Comparison of the non-optimized and 2PA-optimized design reveals major differences. The 2PA-optimized design not only contains less high-



(a)



(b)



(c)

Figure 4.12: Optimization of 2PA in dielectric coating. (a) The 2PA parameter  $\beta$  has been estimated by fitting to the experimental curve for the mirror M2. Theoretical curves related to the single layer of  $\text{Ta}_2\text{O}_5$ , M1 and MM1 have been calculated with the same 2PA parameter  $\beta$  without additional fitting. Solid lines connecting actual measured data points are provided as a guide to the eye. Error bars represent the instrumental error of the measurement. (b) The designed stack of non-optimized M1. The coating contains approx. equal amounts of high-index and low-index material, and the materials are distributed homogeneously. (c) Designed stack of 2PA-optimized MM1. The presence of high-index material is decreased in favor of low-index material, and the high-index material is concentrated farther from the top layers of the stack.

index material, but the material is distributed differently. While in the non-optimized designs high-index material is distributed homogeneously, with significant part of it concentrated in the upper layers of the structure where electric field is strong (Fig. 4.5a, Fig. 4.7a and Fig. 4.12b), in the 2PA-optimized design only a small fraction of high-index material is localized in the upper layers (Fig. 4.5a and Fig. 4.12c). Therefore less high-index material is involved into interaction and, consequently, the influence of the 2PA becomes less pronounced.

Measured reflectance data of the modified design MM1 (Fig. 4.12a) revealed a significant improvement of the performance of the new DM in comparison to mirror M1. Its effective reflectance is higher and it is less dependent on incident intensity in the working range of interest. We have also performed Transient Grating Frequency Resolved Optical Gating (TG FROG) [142] measurement confirming preservation of the dispersive properties of the MM1 mirror.

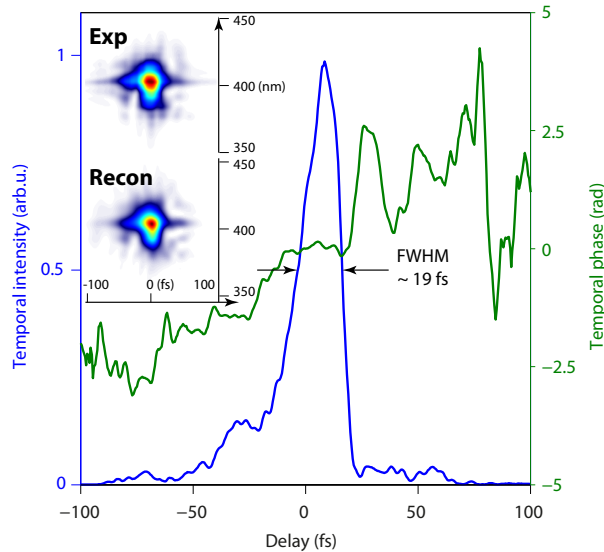


Figure 4.13: TG FROG. Reconstruction yields  $19 \pm 1$  fs pulse duration at peak intensities in order of  $\sim 10^{11}$  W/cm<sup>2</sup>; inset: actual and reconstructed TG FROG traces.

As the reconstructed pulse duration stayed constant even at the highest incident intensities (Fig. 4.13), we can conclude, that dispersion properties of the MM1 device are unaffected throughout the working range.

The thermal performance has been also verified and as well showed noticeable improvement (Fig. 4.14).

The modified design warms up less. Overall, the measured data is in close agreement with the theoretical prediction (Fig. 4.12a), indicating the validity of the developed model and reliability of the obtained value of  $\beta$ .

Overall, we have explored the nonlinear response of dielectric DMs. It was found that the cause of discovered effect is the appearance of third order nonlinear processes,

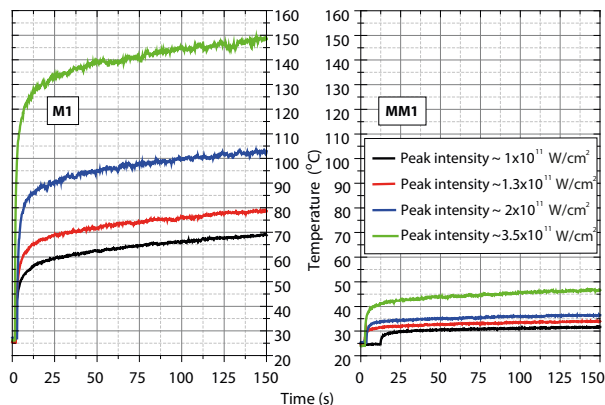


Figure 4.14: Thermal tests of 2PA-optimized design.

triggered by very strong enhancement of the internal electric field, that occurs due to the complicated interference in the dispersive multilayer coating. 2PA dominates the response, as the nonlinearity manifests itself in the form of nonlinear absorptance. Despite the strong 2PA, there were no noticeable changes of refractive index of the layer materials, due to correspondence of the  $E_p$  to  $\sim(0.72 \div 0.74)E_g$ , the region where the nonlinear refractive index is in vicinity of zero. A theoretical model that allows the estimation of the 2PA coefficient and thus prediction and to some extent engineering of the intensity dependent behavior of any multilayer coating has been developed.

We used the developed approach for the design of efficient octave-spanning ultraviolet mirrors that will be later implemented in our OWS apparatus, described in detail in Chapter 5.

## 4.5 Infrared dispersive optics

Just as in the UV, the development of dispersive optics for IR was lagging behind, but for a different reason: the lack of scientific interest. Starting from the wavelength of  $1.5 \mu\text{m}$ , most of the commonly used optical materials change from positive to negative group-velocity dispersion (GVD), while Si and Ge maintain positive GVD through the mid IR range. Consequently, it becomes possible to perform compression in bulk by carefully balancing the materials with opposite GVD in the beam path [143, 144, 86]. Unfortunately, the approach works well only for dispersion compensation to lowest order (GDD), with high-order contributions to dispersion, which are essential for few-cycle pulses, left uncompensated [143]. That becomes essential for few-cycle laser pulses. In addition, with its band gap of 1.11 eV (at 300 K), Si is susceptible to two-photon absorption, restricting the maximum incident intensity. Implementation of dispersive multilayer mirrors offers an elegant solution for circumventing these shortcomings.

Two alternative chirped mirror designs covering the IR range spanning from  $1.6 \mu\text{m}$  to

2.7  $\mu\text{m}$  are presented in Fig. 4.15 . The design illustrated in Fig. 4.15a imitates dispersion introduced by 0.25 mm of Si, design in the Fig. 4.15b follows alternative target. While it introduces the GDD equivalent of 0.25 mm Si at the central wavelength, the sign of third-order dispersion is changed to negative.

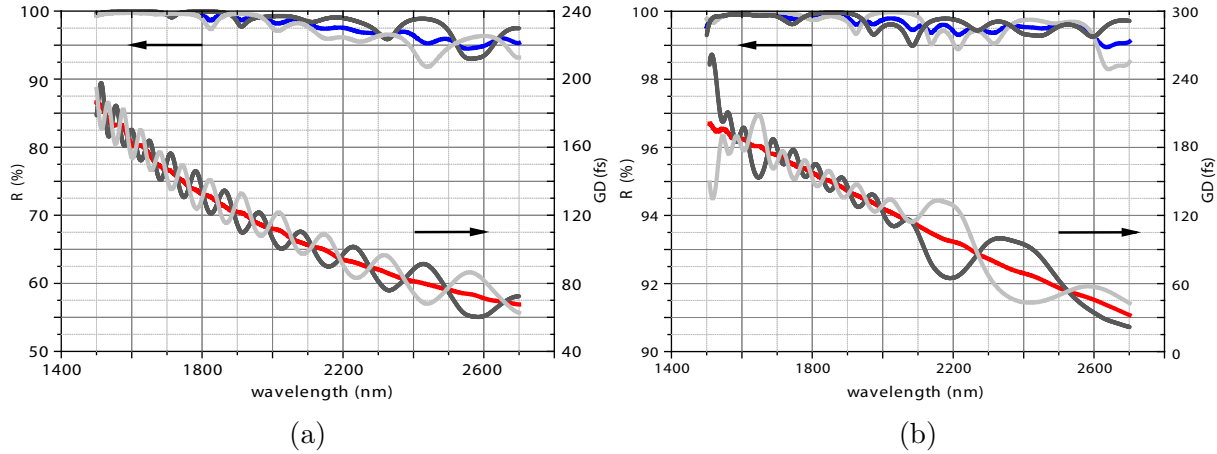


Figure 4.15: (a) Dispersion target and design imitating 0.25 mm Si. (b) Dispersion target and design introducing second order identical to 0.25 mm Si, yet with negative third-order dispersion. Gray, dark gray curves - the designed GD curves of an individual mirror of the mirror pair, red curve - resulting designed averaged GD; gray, dark gray curves - reflectance of the individual mirror of the mirror pair, blue curve - resulting averaged reflectance.

As the thickness of the individual layers of the multilayer design scales with the central wavelength of the incident spectrum, multilayer structures in the IR tend to be substantially thicker than their counterparts designed for VIS or UV wavelengths. For example, the physical thickness of the coatings in Fig. 4.15 approaches  $20\mu\text{m}$ . The risk of excessive tensile stress, which might affect the mechanical properties of the deposited structure and make it peel off from the substrate, increases. The overall physical thickness must therefore be traded off against bandwidth, dispersion and reflectance of the dispersive mirror, all of which tend to increase with increasing number of layers and hence structure thickness. For instance, the design in Fig. 4.15b was allowed to be slightly thicker and contain more layers than the design in Fig. 4.15a, resulting in higher reflectance and improved pulse compression efficiency.

Fortunately, the limitation to the maximum physical thickness is not a fundamental one. The mechanical stress may be reduced by tuning the parameters of the deposition process at the expense of changes in the optical properties of the layers. These changes must be well understood and controlled, before the approach can be used for the production of thicker structures.

Unlike in the UV, there are several layer materials excellently suited for multilayer development in the infrared range. The already mentioned material pair exploited in VIS/NIR,  $\text{Nb}_2\text{O}_5/\text{SiO}_2$ , is transparent until  $8\mu\text{m}$ . For the spectral region beyond  $2\mu\text{m}$

- Si is an excellent high-index material, while  $\text{SiO}_2$  and  $\text{Al}_2\text{O}_3$  are used as low-index counterparts and are transparent until  $7 \mu\text{m}$  [145]. The large electronic band gaps of  $\text{Nb}_2\text{O}_5$  and  $\text{SiO}_2$ : 4 eV and 7.5 eV respectively, allow nonlinear effects to be avoided in the infrared range, permitting developing and production of a broad class of efficient, precise and flexible multilayer designs, essential for broadband pulse manipulation.

## 4.6 Conclusions of Chapter 4

Over the last two decades dispersive multilayer optics have become standard components of ultrashort-pulse laser systems. Next-generation sources based on optical waveform synthesis call for versatile control of the electromagnetic force of light within a half cycle of its oscillation. This calls for multi-octave superposition of optical fields with adjustable phase and amplitude. Again, aperiodic dielectric multilayers constitute an enabling technology for this latest frontier of ultrafast science.

State-of-the-art multilayer deposition technology had to rise to several challenges to be able to produce dispersive mirrors with the required precision in previously inaccessible wavelength ranges. Extension of the dispersive multilayer technology into the UV spectral range required both improved precision in depositing the nanometer-thick layers and new design paradigms to avoid undesirable nonlinear effects coming into play. On the other hand, pushing the opposite spectral frontier of dispersive multilayer optics to ever longer wavelengths calls for new parameter optimization of coating algorithms for providing optimal balance between robust mechanical and best possible optical properties of ever broader multilayer structures.

At present, precision dispersive multilayer designs span over the working range of three octaves, allowing precise and efficient dispersion control of light waveforms composed of signals all the way from ultraviolet ( $0.29 \mu\text{m}$ ) to mid infrared ( $2.7 \mu\text{m}$ ) wavelengths. The acquired experience facilitated the design and production of the advanced multilayer optics implemented in the multi-channel multi-color waveform synthesizer presented in Chapter 5.



# Chapter 5

## Multi-color multi-channel optical waveform synthesis

This chapter is largely adapted from O. Razskazovskaya et al. "Ultra broadband multi-color source for attosecond science", in preparation.

In this chapter we demonstrate a transfer of the optical multi-channel waveform synthesis concept into the infrared spectral range. The apparatus covers a bandwidth spreading over three optical octaves from  $\sim 300$  nm to above  $2.5 \mu\text{m}$  that is subdivided into three channels, each of which delivers sub-two-cycle pulses at the central wavelengths of 450 nm,  $1.2 \mu\text{m}$  and  $2.1 \mu\text{m}$ . If combined, the source supports synthesis of sub-cycle transients at the central wavelength of  $\sim 1.8 \mu\text{m}$ . The developed system is intended to power high-time-resolution studies of the electron dynamics in a broad range of semiconductor materials that are potentially suitable for application in the lightwave electronics.

### 5.1 Introduction

Twenty years of progress in ultrafast optics has gradually pushed the technology to a level that was unimaginable in the 1960, reaching the seemingly fundamental physical limit, – light pulses lasting a single cycle of the oscillating electric field. Those in turn enabled the generation and measurement of isolated attosecond pulses and led to the birth of attosecond metrology, consequently, opening the door for observation and control of electronic motion.

To this end, and – more generally – for the control of electronic phenomena with the electric force of light, precise control and shaping of the electric field evolution (henceforth briefly: optical field) is of crucial importance [146, 147]. Shifting the phase of the carrier wave with respect to the pulse envelope, referred to as the carrier-envelope phase, constitutes the simplest means of modifying the temporal evolution of the optical field. This modification preserves the sinusoidal field evolution and introduces a sub-cycle change in the amplitude evolution for pulse duration comparable to the carrier wave cycle.

More versatile control of atomic-scale electronic motion requires sculpting of the field evolution on an attosecond time scale, *i.e. within the wave cycle of light*. This calls for

super-octave bandwidth and control schemes more sophisticated than simple adjustment of the CEP. Sub-cycle tailoring of optical fields can be implemented by changing the relative time delays between several coherently recombined CEP-stable wavepackets carried at different wavelengths. This generic approach constitutes the basis of optical waveform synthesis. The first successful implementations of OWS concept were based on stimulated Raman scattering [148], the synchronization of independent ultrafast sources [149], or fiber amplifiers jointly seeded with a spectral continuum [59].

More recently, multi-octave phase-stable supercontinua produced by self-phase modulation of millijoule femtosecond pulses in gas-filled hollow-fibers have been spectrally subdivided and – after precision GDD and CEP control as well as delay of the separated wavepackets – coherently recombined. The approach has yielded optical field transients with non-sinusoidal waveforms [56] including ones with durations shorter than 1 fs [106].

However, until now these incredible transients have been synthesized at the central wavelength of the conventional Ti:Sapphire-based ultrafast source, meaning that the wavepacket carries an excitation energy of  $\sim 1.55$  eV. Such a source is well suited for investigating carrier dynamics of the wide class of dielectric materials via the newly developed attosecond polarization spectroscopy [12]. Yet, a class of potentially valuable materials – semiconductors – remains out of reach.

Here we develop an ultra broadband multi-channel multi-colored ultrafast source at a central wavelength of  $\sim 1.8$   $\mu\text{m}$  supporting synthesis of a sub-cycle field transients at an excitation energy of  $\sim 0.6$  eV. Following the concept of the waveform synthesis, the ultra broadband input spectrum spanning over three optical octaves (Chapter 3) generated by intense sub-two-cycle infrared OPCPA (Chapter 2) is treated in three independent dispersive delay lines. After GDD correction with the advanced multilayer dispersive optics (Chapter 4), the channels deliver sub-two cycle pulses at the central wavelength of 450 nm, 1.2  $\mu\text{m}$  and 2.1  $\mu\text{m}$ . A coherent re-combination of the three channels supports  $\sim 1.55$  fs pulse, while the coherently combined near infrared and infrared channels support  $\sim 3.3$  fs pulse, both are the sub-cycle transients at a central wavelength of  $\sim 1.8$   $\mu\text{m}$ . The source is to become driving force for the next studies of the ultrafast electronic processes in large class of dielectric and semiconductor materials, that are potentially suitable for the future light wave electronics.

## 5.2 Experimental set up

The CEP-stable supercontinuum, generated in the Chapter 3, Fig. 5.1a, is seeded into passive (non-amplifying) three-channel optical multi-color source depicted in Fig. 5.1b.

### 5.2.1 Channel subdivision

The first step in the development of the multi-color apparatus is a subdivision of the seeding ultra broadband spectrum into several dispersive delay lines (henceforth: channels). This is usually done with specially designed dichroic beam splitters (DBS).

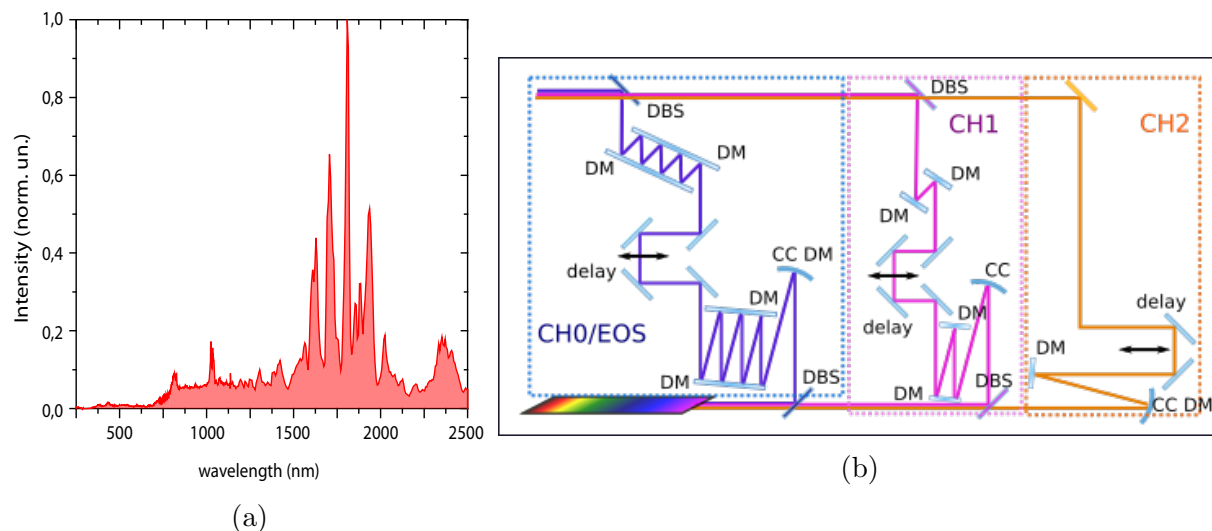


Figure 5.1: Multi-color multi-channel ultrafast source for attosecond science. (a) Spectral coverage of the multi-color source; (b) the set up: DBS- dichroic beam splitter, DM - dispersive mirror, CC DM - concave dispersive mirror, CC - concave mirror, otherwise non-marked plane-plane aluminum (CH0/EOS), silver (CH1) and gold (CH2) mirrors.

As was mentioned in Chapter 4, there are several major requirements to the design of these components: (1) a high contrast between reflected and transmitted light, (2) “cross-talk” region between channels, that is used for channel-to-channel synchronization, (3) smooth, well controlled (preferably flat) phase of both reflected and transmitted spectra in order to ensure compressibility of the individual channels. Requirements (1) and (3) are rather challenging. Most commonly used DBSs are based on the multilayer stacks built of several alternating quarter-wave thick layers. However, the natural high reflectance bandwidths of such DBSs is defined by the contrast between the refractive indices of implemented coating materials and is typically much narrower than the desired bandwidth of the individual synthesizer channels. In addition, there are strong group-delay ripples on the edges of the high reflectance band, that are undesirable from the perspective of spectral phase control. In order to extend the high reflectance band and suppress the GD oscillations, the layer thickness of the DBS multilayer coating are de-tuned, or “chirped”, from the quarter-wave values. The chirping also creates the required “cross-talks” zones.

The designed reflectance and GD for the set of DBSs implemented for spectral division of the generated ultra broadband spectrum is presented in the Fig. 5.2a.

The spectrum is subdivided into three channels: (1) 300 nm – 600 nm , (2) 700 nm – 1400 nm and (3) 1400 nm – 2700 nm. In the present system the channel spanning over 300 nm – 600 nm is intended for the diagnostic purposes. It will deliver a sampling pulse for the electro-optic sampling apparatus that is currently under development and henceforth is denominated as CH0/EOS. The channels spanning over 700 nm -1400 nm and 1400 nm - 2700 nm are henceforth referenced to as CH1 and CH2 accordingly. Spectral coverage of the individual channels is presented in Fig. 5.2b. The CH1 and CH2 are designed for the

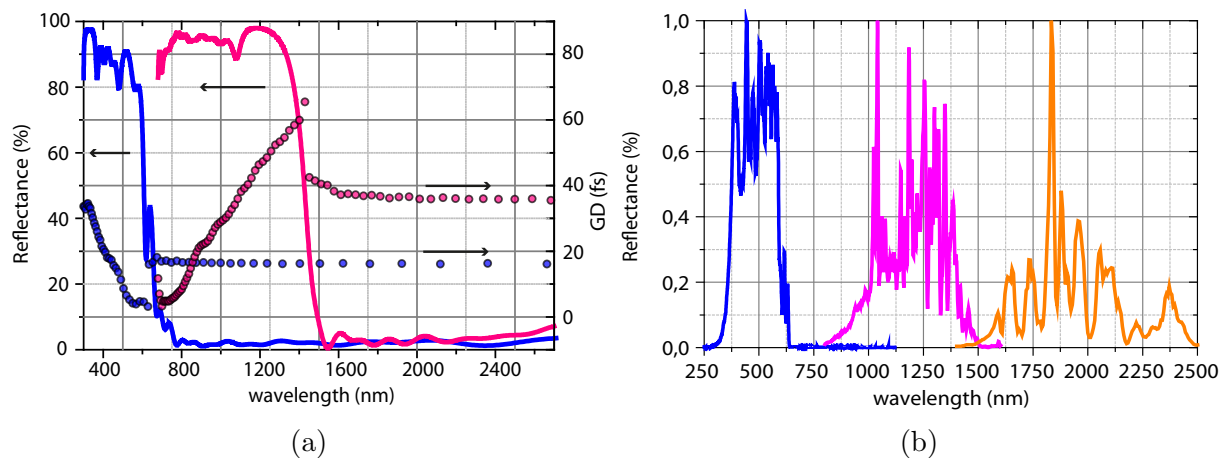


Figure 5.2: Spectral coverage of the multi-color source. (a) Beam splitters employed for the spectral subdivision; (b) spectral coverage of the individual channels, the spectral intensity of each channel is independently normalized.

study of a nonlinear polarization dynamics in the dielectric and semiconductor materials of interest.

The individual wavepackets of the CH1 and CH2 were characterized with the second- and third-harmonic frequency-resolved optical gating (TH-FROG)[63] respectively. We had a possibility to reliably characterize spectral/temporal phases of CH1 and CH2 right after the exit of the hollow-core fiber, since at this point in the system the emerging spectrally broadened pulse remains relatively compressed and pulse energy is sufficient to produce a nonlinear signal with good signal to noise ratio. The recorded traces and reconstructed wavepackets are demonstrated in Fig. 5.3. Due to a very low nonlinear signal generated in the CH0/EOS, which suffers from much higher dispersion in transmissive optics, we had no opportunity to reliably characterize its wavepacket before the compression.

As it can be seen from Figs. 5.3c, 5.3f, while the spectral phase of the CH2 is rather flat, the spectral phase of the CH1 has a well defined surge at the short-wavelength side of the spectral range. In addition, there is a leakage of the infrared frequencies from the CH2 to CH1.

## 5.2.2 Spectral phase control in the individual channels

Compression of broadband wavepackets comprising the individual channels to the transform limit (FTL) requires a precise control over their spectral/temporal phase. The aim of the control in this context is to compensate for the variations in a spectral phase. Therefore, the precise knowledge of a phase to compensate for is a major prerequisite. The known spectral phase is then used either as an input parameter for the Dazzler or, in our case, as a target for the development of the dispersive mirrors.

Several techniques for the characterization of spectral and temporal phase of ultrafast pulses have been developed [63, 62, 64]. Unfortunately, they are still suffering from a range

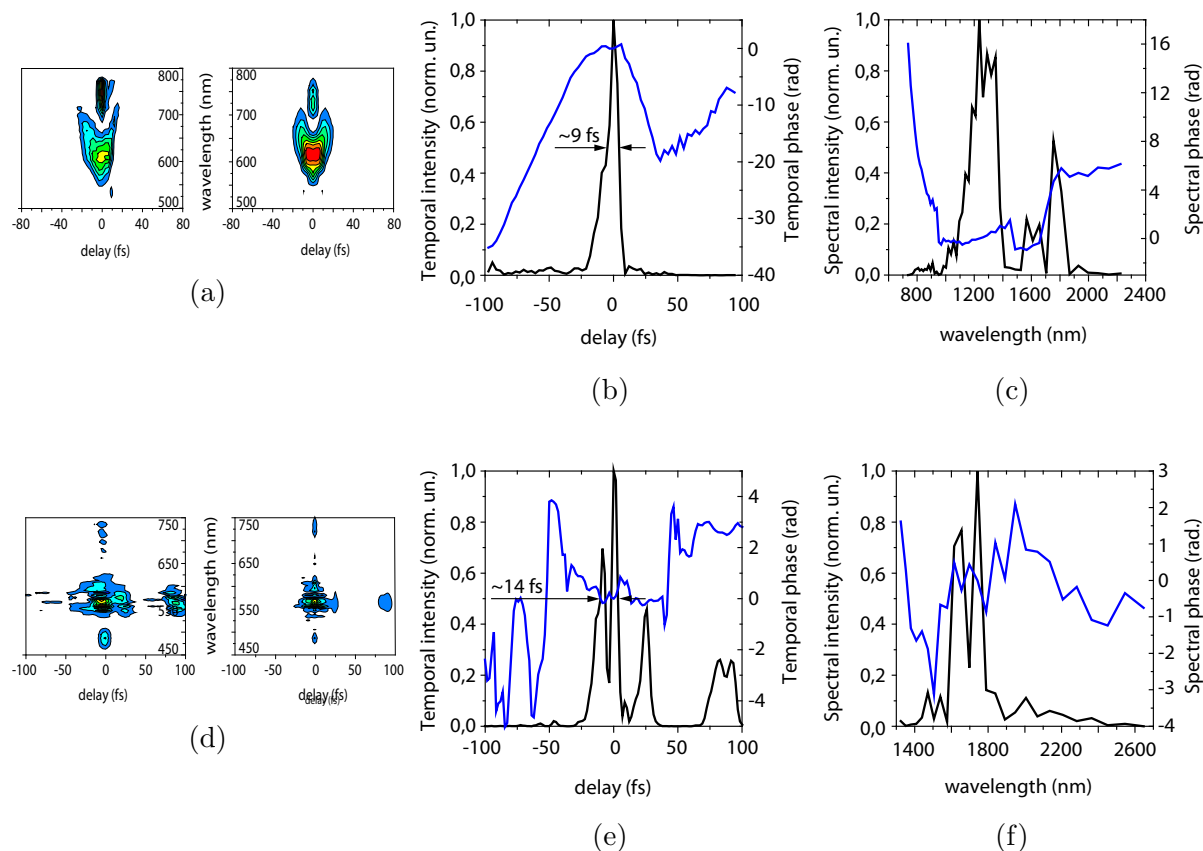


Figure 5.3: Spectra-temporal characterization of the individual channels after the exit from the hollow-core fiber. (a) Recorded and reconstructed SH-FROG spectrogram; (b) reconstructed temporal profile (black) and temporal (blue) phase; (c) reconstructed spectral profile (black) and spectral phase (blue) of the CH1; (d) recorded and reconstructed TH-FROG spectrogram; (e) reconstructed temporal profile (black) and temporal phase (blue); (f) reconstructed spectral profile (black) and spectral phase (blue) of the CH2.

of ambiguities and limitations [118, 150] especially when dealing with nearly single cycle pulses and pulses that are substantially chirped. As a result, the phase retrievals often appear to be inconsistent or not accurate enough to be used as targets for development of dispersive multilayer optics. Under these circumstances, there are alternative approaches in existence.

In particular, compensation for the accumulated material dispersion only is often a method of choice. Following this approach the spectral phase is approximated to the amount of the material dispersion that the assumed FTL pulses accumulates upon its propagation to the point of the experiment. The dispersive optics is then designed to compensate for the total introduced spectral phase.

In [101] we proposed and proved a more advanced “hybrid” approach. In this method

the initial dispersion target is estimated with the material dispersion taken into account. However, after the initial set of optics is produced and the partially compressed pulse can be measured and fully characterized, the next set of optics that compensates for the residual phase is produced.

In the present system we have implemented material compensation and “hybrid” approaches for the design of the dispersive optics. As the pulse energy of the CH0/EOS was insufficient to make a reliable phase measurement over the entire spectral range covered by the channel, we have turned to the material compensation approach and estimated the accumulated dispersion knowing the amount of materials in the channel. This estimation was used as the dispersion target, Fig. 5.4a (inset). As the spectral phase of the CH2 had no significant features to be concerned about, its dispersive target was as well developed following the material compensation approach, Fig. 5.4c.

For the development of the optics for CH1 we turned to a modified “hybrid” approach. The spectral phase information of the CH1 (Fig. 5.3c) was used to calculate reference GD and group-delay dispersion (GDD) of an empty channel with high accuracy. At the second step, similar to the material compensation approach, we calculated the dispersion of the optical components later used in the channel and added the value to the measured one. The sum became the CH1 dispersion target, Fig. 5.4 (inset).

The mirrors for the CH0/EOS and CH1 were designed using a double-angle approach[113], sixteen bounces on the dispersive mirrors are needed for the compression in CH0/EOS and four in CH1. The mirrors of the CH2 are a complimentary pair [55], only one complimentary pair is used in CH2, Fig. 5.1b. Commercially available OptiLayer software [] was used for all designs. Designed reflectance and GD curves are presented in Fig. 5.4.

HfO<sub>2</sub>/SiO<sub>2</sub> material pair was used for the deposition of the CH0/EOS mirrors and Nb<sub>2</sub>O<sub>5</sub>/SiO<sub>2</sub> pair for the mirrors of CH1 and CH2. The coatings were deposited by magnetron sputtering(Helios plant, Leybold - Optics GmbH, Alzenau, Germany). The produced optics were characterized with spectrophotometer (Perkin Elmer Lambda-950) and home-built white light interferometer based on spectral interferometry. Measured GD of the produced and implemented components is presented in Fig. 5.4d.

### 5.3 Multi-color ultrafast source

The mechanical design of the source is presented in Fig. 5.1. In addition to the dispersive mirror, the fine tuning of the dispersion is performed by changing amount of the material in the channels with wedges and thin plane-parallel plates produced of MgF<sub>2</sub>, CaF<sub>2</sub> and ZnSe (not shown in the sketch).

The channels were temporally characterized using X-, SH - and TH-FROG.

The X-FROG was used to characterize the temporal profile of the pulse in CH0/EOS. For the reference pulse, a part of the supercontinuum was split and filtered through a narrow band filter centered at 1550 nm. The reference was independently characterized with the SHG FROG, Fig. 5.5c. The reconstructed pulse was later used for the X-FROG reconstruction of the CH0/EOS pulse, Fig. 5.5f. Reconstructed X-FROG trace shows

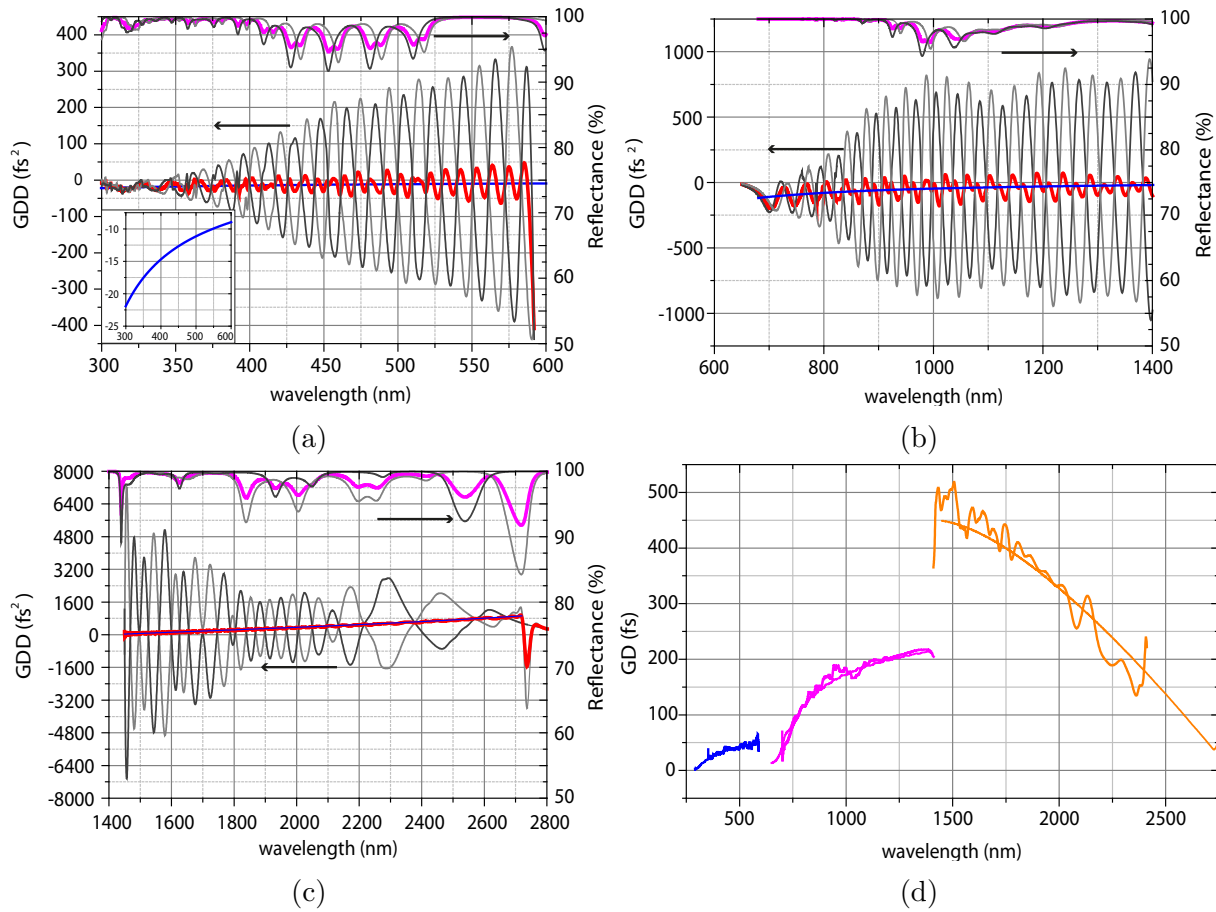


Figure 5.4: Dispersive optics of the multi-color source. (a) Dispersive mirror designed for CH0/EOS. Inset: zoomed in dispersive target of the CH)/EOS mirror; (b) dispersive mirror designed for the CH1: gray, dark gray curves - designed GDD and reflectance at 5° and 19° angles of incidences, solid red line - total GDD per pair, solid magenta line - total reflectance per pair, solid blue line - dispersion target; (c) dispersive mirror designed for the CH2: gray, dark gray curves - designed GDD and reflectance of the individual mirrors of the pair, solid red line - total GDD per pair, solid magenta line - total reflectance per pair, solid blue line - dispersion target; (d) measured group delay of the dispersive mirror pairs of the individual synthesizer channels.

compression for the CH0/EOS to  $\sim 2$  fs - nearly the transform-limited pulse duration (FTL  $\sim 1.9$  fs). Reconstructed spectrum confirms the presence of all frequency components and corresponds well to the one measured with the grating spectrometer, Fig. 5.2b, thus assuring the reliability of the measurement.

SH- and TH-FROG were used to characterize CH1 and CH2 accordingly. The measured traces and reconstructed spectral and temporal profiles are presented in Fig. 5.6.

The CH2 is as well compressed to nearly the transform limit -  $\sim 13$  fs vs.  $\sim 12$  fs FTL, again showing a close correspondence between reconstructed and recorded spectra.

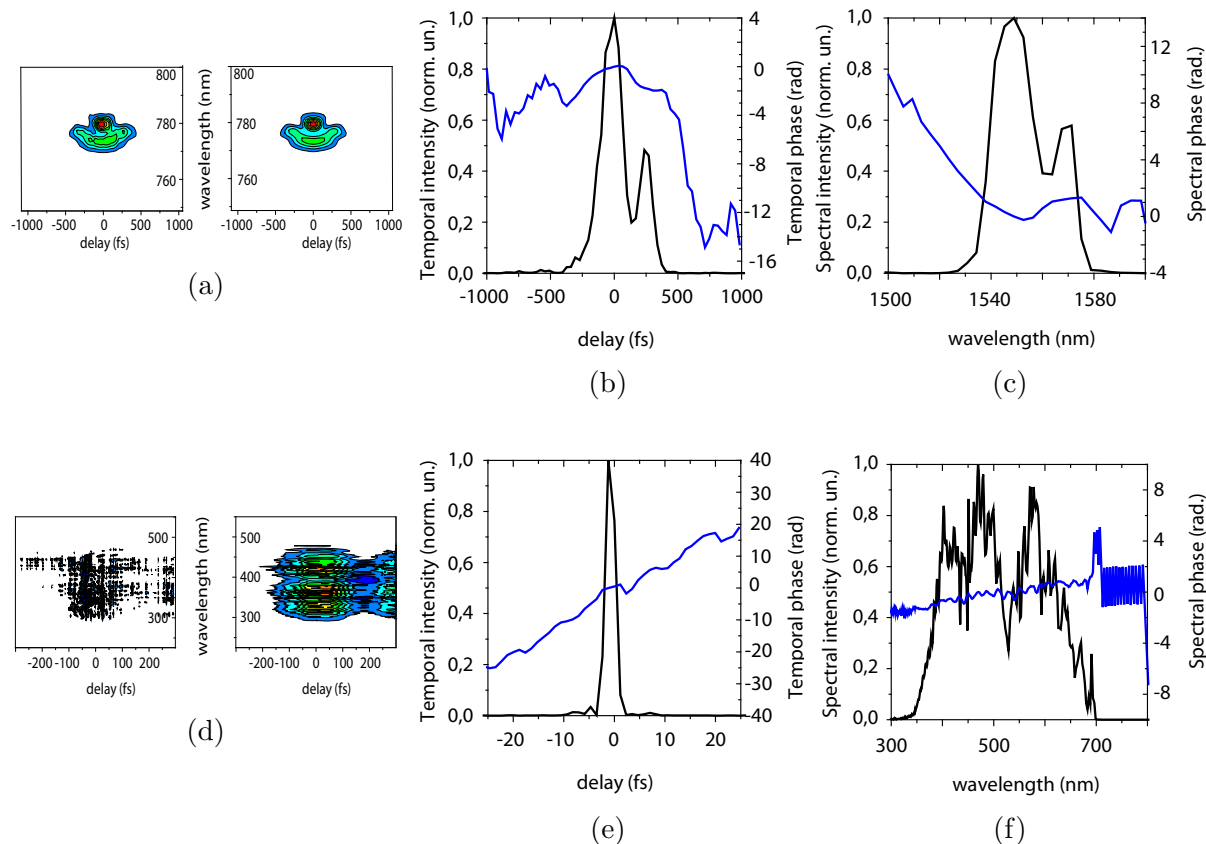


Figure 5.5: Spectra-temporal characterization of the CH0/EOS. (a) Recorded and reconstructed SH-FROG spectrogram of the 1550 nm reference pulse later used for X-FROG; (b) reconstructed temporal profile (black) and temporal (blue) phase; (c) reconstructed spectral profile (black) and spectral phase (blue) of the 1550 nm reference pulse; (d) recorded and reconstructed X-FROG spectrogram; (e) reconstructed temporal profile (black) and temporal phase (blue); (f) reconstructed spectral profile (black) and spectral phase (blue) of the CH0/EOS.

The CH1 is compressed to  $\sim 8$  fs – noticeably longer than supported FTL of 6.2 fs. However, due to the limited reflectance bandwidth of the dispersive mirrors, the lower frequency components that were present in the channel right after the exit of the hollow-core fiber, Fig. 5.3c, are now filtered out. Reconstructed spectrum, Fig. 5.6c, corresponds well to the one measured with the grating spectrometer, Fig. 5.2b, indicating the reliability of the measurement. The reconstructed spectral phase of the CH1 (Fig. 5.6c) shows a residual high order spectral phase in the short wavelength region. Peculiarly, the absolute value of the residual phase is identical to the one that was measured right after the entrance of the hollow-core fiber. An additional adjustment step will be needed to correct for this residual phase with the hybrid approach.

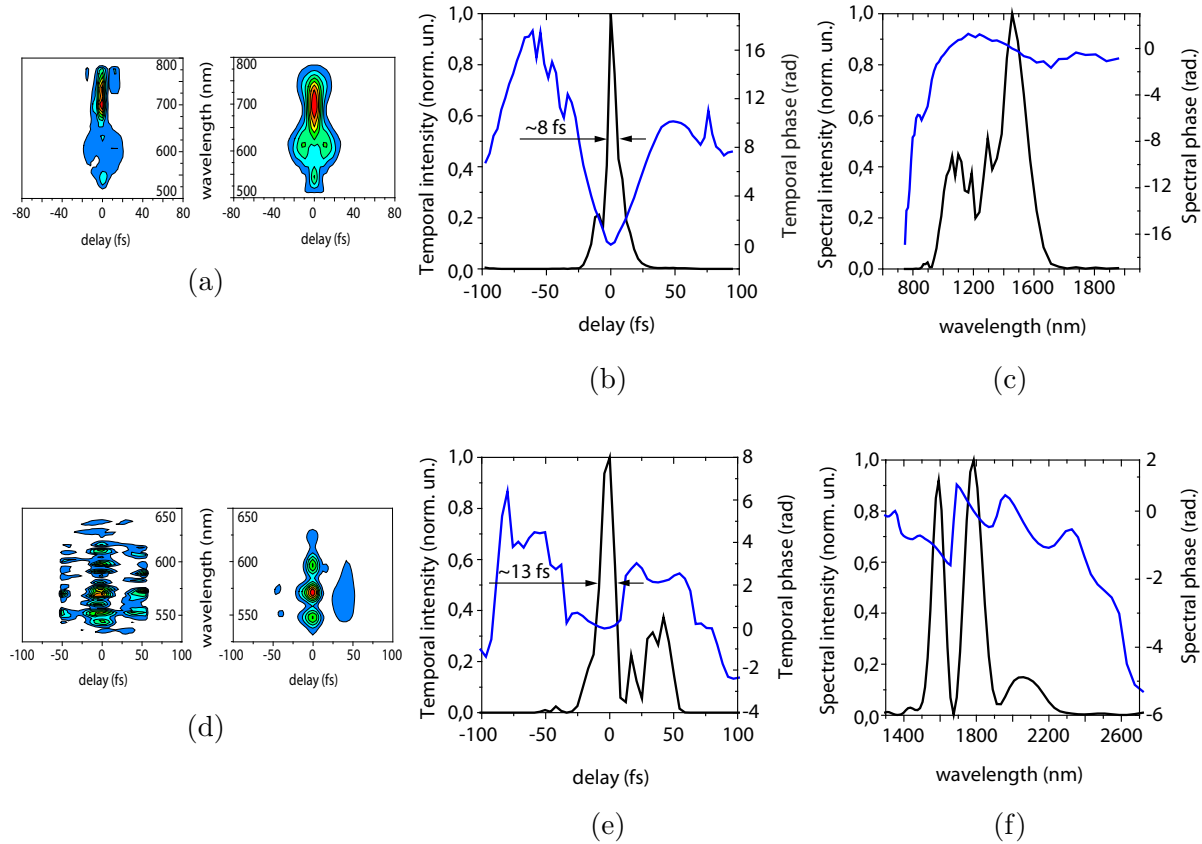


Figure 5.6: Spectra-temporal characterization of the individual channels after compression. (a) Recorded and reconstructed SH-FROG spectrogram; (b) reconstructed temporal profile (black) and temporal (blue) phase; (c) reconstructed spectral profile (black) and spectral phase (blue) of the CH1; (d) recorded and reconstructed TH-FROG spectrogram; (e) reconstructed temporal profile (black) and temporal phase (blue); (f) reconstructed spectral profile (black) and spectral phase (blue) of the CH2.

## 5.4 Conclusions of Chapter 5

Here we presented development of the multi-color multi-channel ultra broadband light source with the spectral coverage exceeding three optical octaves. The source comprises three color channels each of which delivers a sub-two cycle pulse. CH1 and CH2 can be used either together, or individually to look at the carrier dynamics in different photon energy regions. CH1 and CH2 combined support synthesis of a 3.3 fs pulse – a sub-cycle transient at a central wavelength of  $\sim 1.8 \mu\text{m}$ . CH0/EOS is developed to become a probe pulse for the electro-optic sampling detection scheme. In general, CH0/EOS can also be added into the synthesis. If so, the three channels combined enable synthesis of  $\sim 1.55$  fs pulses. Nonetheless, this is outside of our interests at the moment.



# Chapter 6

## Electro–optic sampling of near–infrared and visible waveforms

This chapter presents a proof–of–principle experiment demonstrating the feasibility of measuring near infrared and visible waveforms with high–frequency broadband electro–optic sampling technique.

Here we develop a high–frequency broadband electro–optic sampling scheme for a direct recording of optical waveforms with frequencies up to 500 THz (600 nm) – well into near–infrared and visible range. For the first time, the technique that is otherwise used in the terahertz (THz) range enters optical frequencies.

### 6.1 Introduction to the topic

Attosecond science empowers observation and control of electron motion. In particular measurement techniques [40, 12], the crucial information is extracted from the imprint that the process being observed leaves on the transmitted/reflected electric field. For this reason the exact knowledge of the electric field evolution, including amplitude and phase, is of a crucial importance.

Time–domain, field–resolved measurements are common in the THz spectral range. One of the potent techniques that is well–recognized in the community is electro–optical sampling (EOS) [67, 68, 151]. It offers broadband detection, flat spectral response and straight forward interpretation of the experimental results all in elegant, compact and cost efficient apparatus. The functionality is based on the exploitation of the linear optical (Pockels) effect between a terahertz field and a substantially shorter well–polarized sampling pulse. Upon propagation in the electro–optical crystal the terahertz field induces birefringence that affects the polarization ellipticity of the sampling pulse. The ellipticity modulation of the sampling beam can then be analyzed to provide information on both the amplitude and phase of the applied electric field.

As the sampling pulse should typically be substantially shorter than the half cycle of the test field, the electro–optic sampling is limited to the frequencies of 135 THz (2.2  $\mu\text{m}$ )

and below.

The direct recording of the visible and near infrared frequencies has been hitherto available via the attosecond streaking camera [65, 66, 152] and petahertz optical oscilloscope [153]. However, both techniques rely on generation and detection of extreme ultraviolet radiation, are rather complex and require cumbersome vacuum apparatus, that is both expensive and technologically demanding. A promising new addition is a recording of the electric field evolution via generation of photo-induced currents in dielectrics [10, 154], however, the exact transfer function between the recorded currents and the driving electric field is not well-defined yet.

Recently, a novel high-frequency broadband EOS detection scheme that is taking advantage of a delicate spectral filtering allowed to dramatically shift the detection limits of EOS to as high as 220 THz ( $1.2 \mu\text{m}$ ) [69].

This impressive shift in the paradigm originates in the fact that the mechanism of the polarization rotation in high-frequency (broadband) EOS differs from the standard picture of the quasi-static Pockels effect, where the sampling pulse should be significantly shorter than a half-period of the oscillation to be observed. The method doesn't directly utilize the interaction between the terahertz test waveform and the typically near-infrared sampling pulse. Instead, upon propagation the interacting test electric field and the sampling broadband pulse generate a nonlinear signal that is frequency up-shifted (in the case of sum frequency generation (SFG)) or down-shifted (in case of the DFG) relatively to the sampling pulse in such a way, that there is a spectral overlap between the nonlinear signal and the part of the sampling pulse's spectrum. The presence of the nonlinear signal then produces the polarization rotation of the sampling pulse. This polarization rotation is primarily confined to the outer edges of the sampling pulse's spectrum in the case of high frequency test fields, and can be therefore isolated by appropriate spectral filtering implemented before the polarimeter [155]. Consequently, the limitation for the maximal pulse duration of the sampling pulse is eased and it is possible to reliably record the test waveforms which half cycle is up to 2.3 shorter than the sampling pulse. Unlike in the case of the standard EOS, the recorded signal is no longer an intuitive cross-correlation between the test and the sampling pulses. An additional interference process is involved, thus making the interpretation of the results more elaborate, yet not less accurate.

A further expansion of the detection limits into the near-infrared/visible is viable, yet necessitates availability of a broadband sampling pulses with significant spectral content in the ultraviolet spectral range in order to enable the detection of the SFG signal generated by the visible components of the spectrum. In this chapter I present development of a high-frequency broadband EOS set up, that enables direct recording of near-infrared and visible light fields.

## 6.2 Experimental set up

The experimental set-up of the developed broadband EOS is depicted in Fig. 6.1. After the final re-combination DBS, Fig. 5.1b, the test near-infrared/visible waveforms belonging

to the channels CH1, CH2 or CH1 and CH2 combined are co-propagating with the probe pulse emerging from CH0/EOS. The pulses are polarization-filtered and consequently co-focused via an off-axis aluminum parabolic mirror ( $f = 150$  mm) into the  $100 \mu\text{m}$  type-I BBO crystal. The incident electric fields are polarized along the ordinary (o) axis of the crystal. A SFG signal is then generated along the extraordinary (e) axis of the crystal. The generated SFG has a spectral and temporal overlap with the high frequency edge of the sampling's CH0/EOS pulse spectrum. The generated SFG signal induces polarization rotation onto the sampling pulse, that is later detected with Wollaston prism and balanced photo diode.

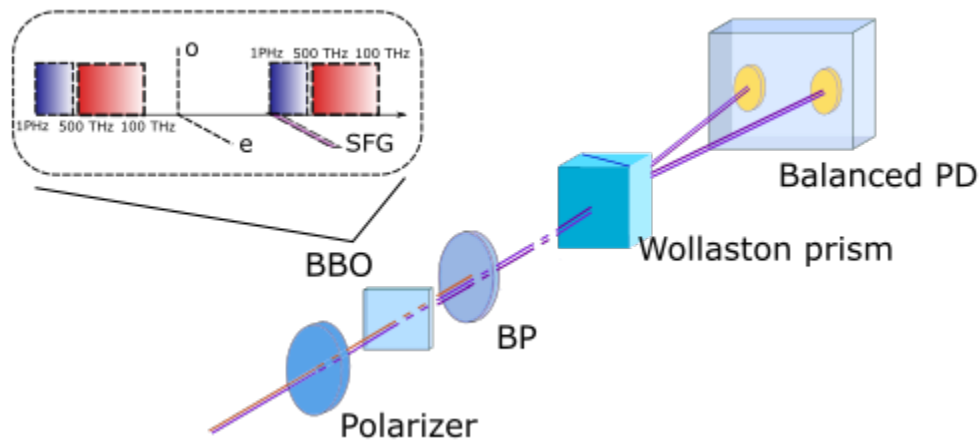


Figure 6.1: High-frequency broadband electro-optic sampling. The set up. BBO –  $100 \mu\text{m}$  type-I BBO crystal. BP - band-pass filter, cut of at  $320 \text{ nm}$ ,  $\lambda/4$  - quarter-wave plate, Balanced PD – balanced photo diode.

In order to unambiguously detect the frequencies in the  $500 \text{ THz}$  ( $600 \text{ nm}$ ) to  $100 \text{ THz}$  ( $3 \mu\text{m}$ ) range, the SFG signal produced by mixing of those components with the sampling pulse has to have no spectral overlap with the test pulse itself. Thus, the lower frequency edge of the sampling pulse should start at about the  $500 \text{ THz}$  mark. On the other hand, in order to be able to sample the highest frequencies of the test pulse, the produced SFG signal has to still have a spectral overlap with the sampling pulse. That means that the highest frequency of the sampling pulse should be at around and beyond  $1 \text{ PHz}$  ( $300 \text{ nm}$ ). Thus, the sampling spectral bandwidth that is required for a clean detection of visible and near-infrared waveforms is  $500 \text{ THz}$  to  $1 \text{ PHz}$ . **We have to note that the detection is reliable only in case when all signal contributions add coherently, implying a requirement for a minimal group delay dispersion over the above mentioned formidable sampling spectrum.** This nontrivial challenge was successfully solved in Chapter 5 by generation of  $\sim 2 \text{ fs}$  CH0/EOS sample pulse, thus, essentially enabling the operation of the detecting scheme.

As it is the shortest wavelengths that are required for the detection of the highest frequencies in the test waveform, the detection bandwidth along with the signal-to-noise ratio can be drastically improved by a proper filtering [155]. The spectral range of the

sampling pulse is presented in the Fig. 5.2b. The spectral region between 300 nm and 320 nm ( THz to THz) is vital for detection of the 500 THz spectral cut off of the two-channel synthesizer. We introduced several bandpass filters centered at around 315 nm for enhancing the EOS's spectral response in that range, Fig. 6.1.

### 6.3 Experimental results

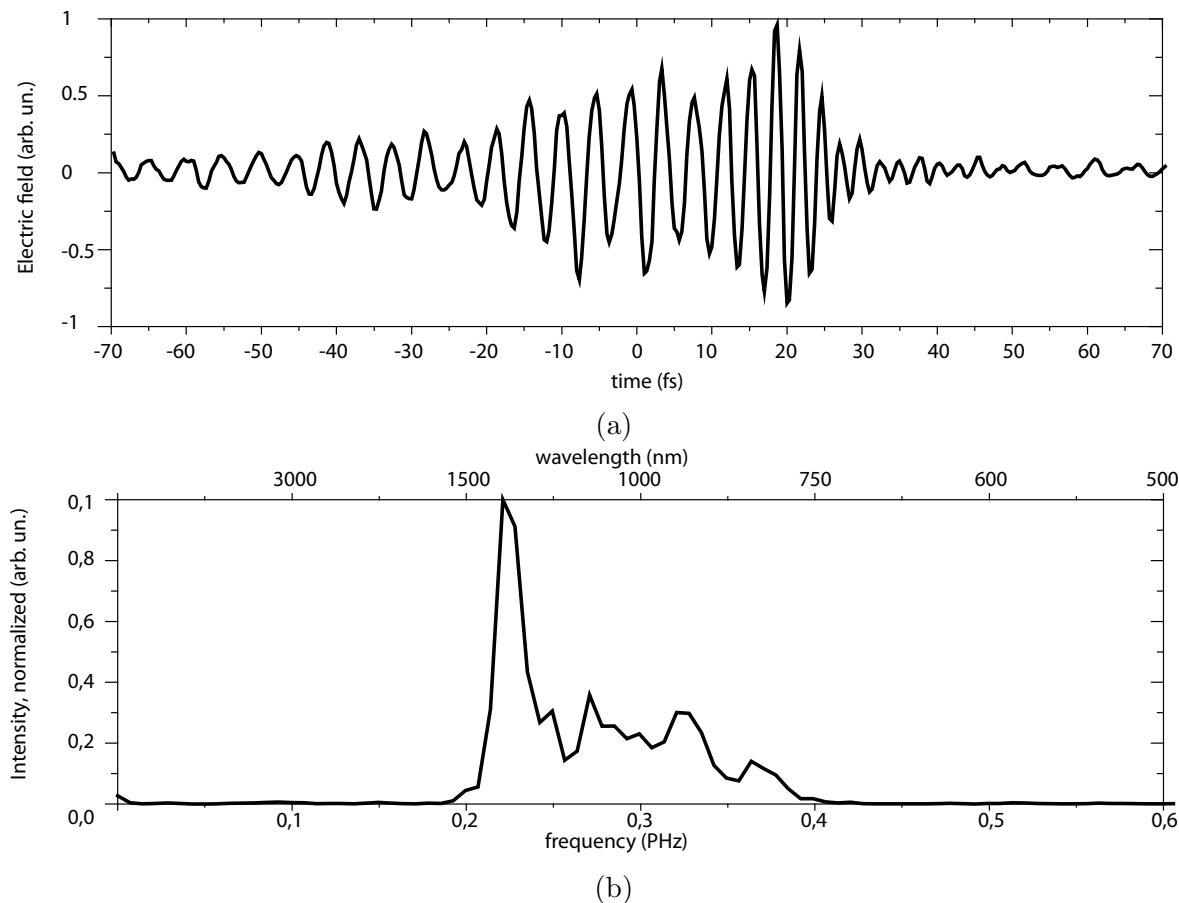


Figure 6.2: Electro-optic sampling of visible-near-infrared waveforms. (a) Recorded EOS trace of the waveform in CH1; (b) spectrum reconstructed from the recorded EOS trace.

Using the described apparatus, we have sampled waveforms delivered by the CH1 and CH2. For the recording of the EOS traces we use the temporal delays installed in the corresponding channels, Fig. 5.1, while the temporal position of the sampling CH0/EOS pulse remains fixed. Temporal overlap between the test and the sampling pulse is found and set to the point where the SFG signal between the two, that is observed with the grating spectrometer (Ocean Optics, Maya Pro), is maximized. Spatial overlap is set by finding an optimizing interferometric fringe pattern between the generated SFG signal and

the sampled pulse. The recorded electric field vs. time EOS traces are presented in Figs. 6.2a, 6.3a.

From the recorded EOS-traces the spectra are obtained by taking the squared modulus of the Fourier transformation of the sampled electric field. The reconstructed spectra confirm presence of all the required frequency components contained in the original spectra, Figs. 5.2b. However, a precise interpretation of the recorded waveforms, comparison of the reconstructed spectra with the spectra recorded via grating spectrometers and with the acquired FROG traces requires a definite knowledge of the EOS response function and is an ongoing work.

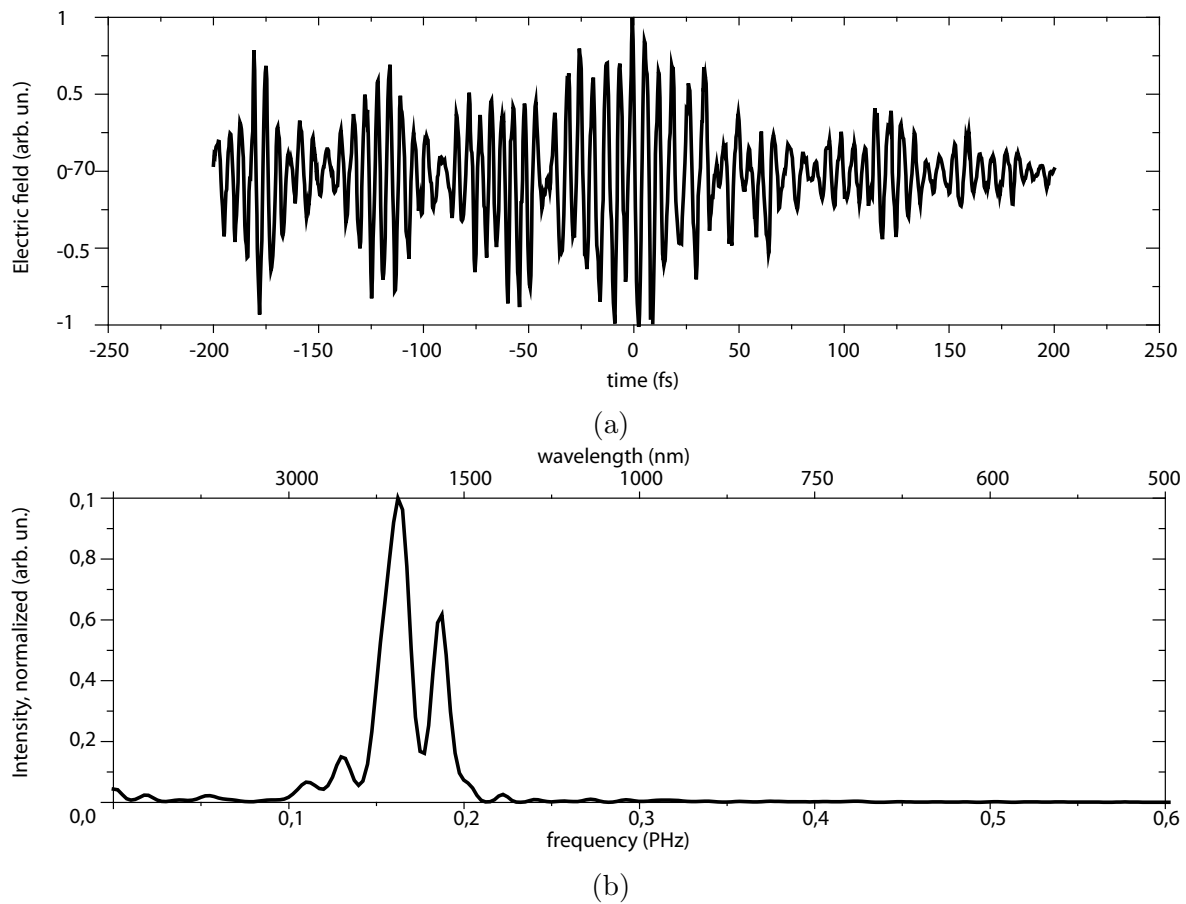


Figure 6.3: Electro-optic sampling of near-infrared waveforms. (a) Recorded EOS trace of the waveform in CH2; (b) spectrum reconstructed from the recorded EOS trace.

After confirming the functionality of the newly developed broadband high-frequency EOS in the frequency ranges covered by the individual channels, we have attempted to record a waveform that is produced by a coherent re-combination (synthesis) of CH1 and CH2.

The temporal and spacial overlap between the CH1 and CH2, and CH0/EOS was

found following the procedure of generating the SFG signal and optimizing the contrast of the interferometric fringe patterns described a couple of paragraphs above. Synthesis of the waveforms that incorporate the entire spectral bandwidths requires well balanced contributions from the individual spectral components. As in our case only about 13% of the supercontinuum energy is re-distributed into the CH1, the energy contribution of the CH2 has to be substantially reduced in order to balance the CH1 and ,thus, enable the synthesis of the ultimate waveform covering the entire CH1 + CH2 range. The CH2 beam is limited with an iris.

Unlike in the case of the individual channels, in the case of the synthesized waveforms the temporal delay of the CH0/EOS is scanned in order to record the EOS trace. The recorded electric field vs. time trace acquired by our novel broadband high-frequency EOS is presented in Fig. 6.4a.

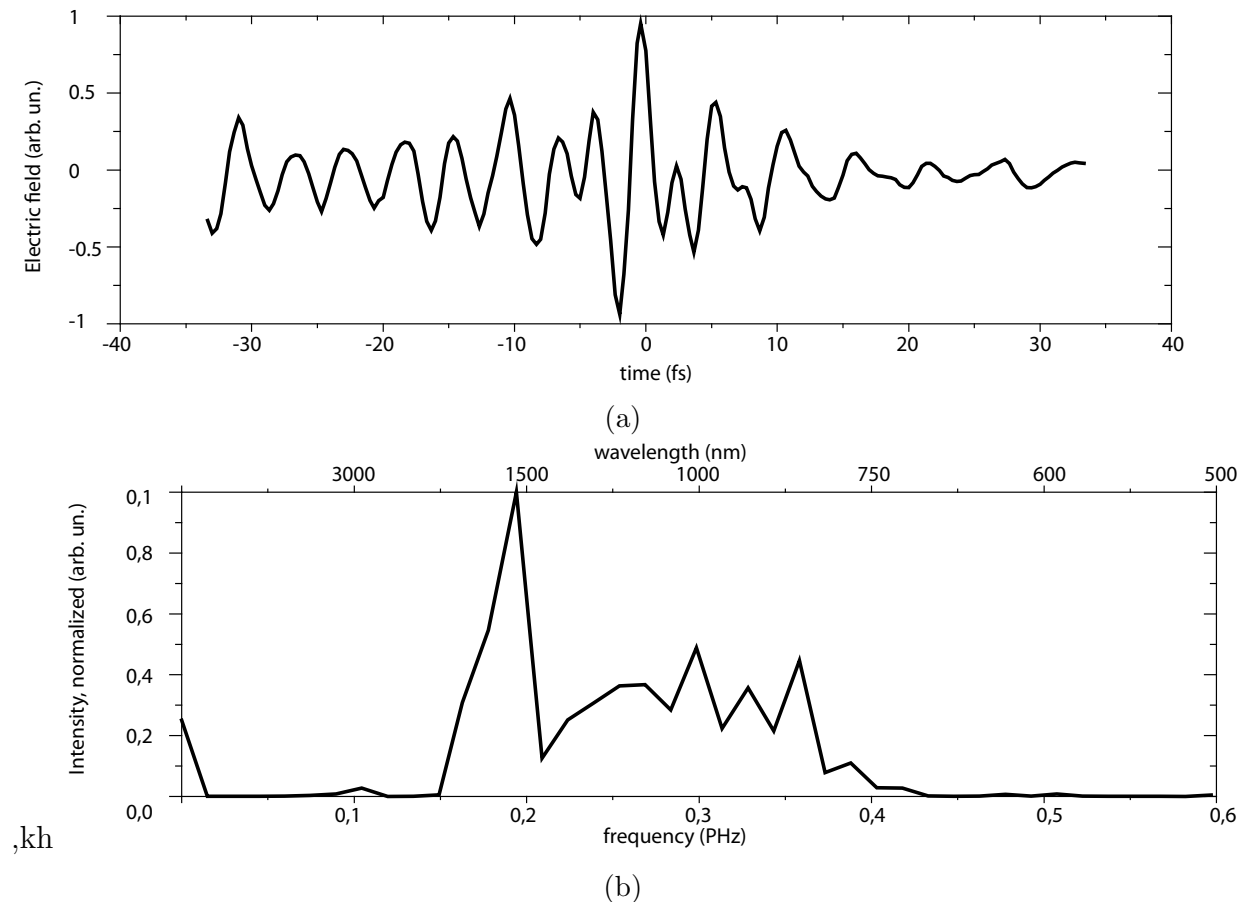


Figure 6.4: Electro-optic sampling of visible-infrared waveforms. (a) The electric field. vs time EOS trace of the waveform synthesized by coherent re-combination of the CH1 and CH2; (b) spectrum reconstructed from the recorded EOS trace.

The recorded trace reveals synthesis of a waveform that comprises less than one oscil-

lation of the electric field under the envelope. The high-frequency cut off is at as high as 430 THz (700 nm) which corresponds well to the high-frequency edge of the CH1. Yet, we stress that a precise interpretation of the recorded waveforms is only possible with a precise knowledge of the EOS response function.

Unfortunately, the detection scheme is not sensitive in the frequency range between 430 THz and 500 THz. However, that should be attributed to the fact that the dispersive optics implemented for the dispersion compensation in the CH1 has spectral coverage till 430 THz only. Outside this frequency range the dispersion is no longer rendered, thus, the requirement for the coherency of the contributions from both test and sampling pulses, Com. 6.2, is violated, consequently causing the loss of the technique's detection capabilities.

## 6.4 Conclusions of the Chapter 6

We have demonstrated a benchmarking development of a broadband high-frequency EOS apparatus capable of unambiguously detecting the frequency components as high as 430 THz (700 nm). The apparatus marks a scientific and technological milestone when a measurement technique, otherwise used in the THz range, allows direct recording of the electric field of visible light. The apparatus offers a unique ability for a complete characterization of the infrared, near-infrared and visible waveforms with retrieving information about spectral amplitude, spectral phase and absolute CEP in a compact, simple and free-space set up without the need for a cumbersome vacuum apparatus. With a foreseeable expansion of the detection limits to up to 500 THz, the apparatus will cover a working range of most commonly used Ti:Sapphire based drivers that are currently applied in the experiments of attosecond science, challenging the attosecond streak camera and becoming a tool of paramount importance for the future experiments in attosecond and strong-field physics.



# Conclusions

In the view of the anticipated dawn of silicon electronics, light-based signal processing became one of the major topics of current scientific interest. While light-based communication is a well-developed technology, light-based signal processing requires an availability of a major building block – an optical transistor. Consequently, large scientific and technologically efforts are now focused onto investigation of passive all-optical switching and all-optical logic.

Recent work of A. Sommer and colleagues has uncovered a viable physical mechanism that could potentially allow for optical switching at up to PHz clock rates while simultaneously assuring nearly zero heat emission. The dynamics was observed in fused silica – a wide band gap dielectric under the irradiance with intense near-infrared sub-two-cycle light fields. However, it is of fundamental character and is expected to be common for other materials, including silicon. Yet, the similar investigations of silicon, the most technologically relevant material up-to-date, would require usage of intense ultrafast sources covering near-infrared and infrared spectral ranges along with a technique capable of a complete characterization of those intense fields.

This dissertation presents development of an intense ultrafast multi-color multi-channel coherent phase-stable source spanning over visible, entire near-infrared and infrared ranges and introduces a valuable measurement technique that potentially enables full temporal characterization of the produced light fields.

The developed source is built following the concept of the parallel optical waveform synthesis that enables generation of arbitrary waveforms via a coherent recombination of several spatially and temporally confined wavepackets at different central frequencies. The essential component for such an apparatus is the availability of an ultra broadband, coherent, and phase-stable supercontinuum spanning over several optical octaves. Generation of the required supercontinuum is a formidable challenge on its own.

In order to generate the necessary spectrum, a substantial upgrade of the pre-existing set up has been performed. A novel hybrid degenerate/nondegenerate optical-parametric amplification stage based on the combination of two amplification crystals has been implemented. The combination of type-I and type-II barium borate crystals(BBO) has allowed to circumvent the power and bandwidths limitations of the pre-existing set up based on the bulk lithium niobate, ultimately yielding energetic (1.3 mJ) sub-two-cycle pulses ( $\sim 11$  fs) at a central wavelength of  $\sim 2.1 \mu\text{m}$ .

These pulses were used to generate an ultra broadband mJ-level supercontinuum span-

ning over three optical octaves from  $\sim 280$  nm to beyond  $\sim 2.5$   $\mu\text{m}$  – an unprecedented spectral bandwidth. The good phase-stability of the generated supercontinuum ( $\sim 200$  mrad) enables exploitation of the developed sources for the purposes of ultrafast pump-probe spectroscopy, electro-optical imaging and other experiments relying on the time-resolved analysis of the evolution of the electric field.

Along the lines of the waveform synthesis concept, the generated phase-stable spectrum was subdivided into three dispersive-delay lines (channels). The wavepackets in each channel were temporally compressed to about the Fourier-transform-limited pulse durations via implementation of advanced multilayer thin-film dispersive optics, delivering sub-two-cycle pulses at central wavelengths of  $\sim 450$  nm,  $\sim 1.2$   $\mu\text{m}$  and  $\sim 2.1$   $\mu\text{m}$ . If coherently combined, the three channels together would ultimately allow to synthesize sub-cycle-transients at a central wavelength of  $\sim 1.8$   $\mu\text{m}$  – unique tool for time-resolved investigation of the electron and band gap dynamics in semiconductor materials. At the present state, the ultraviolet channel is, however, used for diagnostics purposes only. Meanwhile, the near-infrared and infrared channels support a nearly-single cycle transient at  $\sim 1.8$   $\mu\text{m}$  if coherently combined, while still providing a sub-two-cycle pulses at the carrier wavelengths in the spectral regions that are of the most interest in application to common semiconductors.

Special care was taken for the design of the dispersive optics for the channel covering ultraviolet region of the spectrum. In the course of the work it was found that a specific distribution of the electric field created within the thin-film structure of the dispersive optics creates a significant enhancement of the internal electric field. The enhancement becomes substantial to trigger the appearance of the nonlinear effects, that are not observed in the case of bulk materials. Namely, we have found a strong enhancement of the two-photon absorption that causes significant losses. Luckily, it is possible to modify the initial multilayer structures in the way that the enhancement is largely suppressed, while maintaining the dispersive properties of the developed component unaffected. These findings assisted in efficient compression of the ultraviolet synthesizer channel.

A new efficient approach for the development of the dispersive optics for visible spectral range was proposed and verified and first steps were made in the development of infrared dispersive mirrors.

The wave packets delivered by the ultraviolet channel of the synthesizer became enabling force for a novel high-frequency electro-optic sampling diagnostics tool. Based on the induced polarization rotation the technique allowed to resolve and directly record electric fields with the frequency content as high as 430 THz – a paramount achievement for the approach that is typically used in the infrared spectral range. Implementing the technique, visible transients were directly recorded for the first time in an all-optical, free space apparatus.

Overall, the developed source together with the high-frequency electro-optic sampling diagnostics becomes a unique package for the fine time-resolved studies of band gap and electron dynamics in a wide range of dielectric and, most importantly, semiconductor materials. With this tools, acquiring the knowledge necessary for the development of the fast, efficient, all-optical electronics is hopefully closer than we could ever fancy.

# Appendix A

## Data archiving

The experimental raw data, evaluation files, and original figures can be found on the Data Archive Server of the Laboratory for Attosecond Physics at the Max Planck Institute of Quantum Optics: [//AFS/ipp-garching.mpg.de/mpq/lap/publication\\_archive](http://AFS/ipp-garching.mpg.de/mpq/lap/publication_archive). For each chapter of the thesis, there is a dedicated folder. In case the figure is produced by some data processing, there is a separate folder containing the .opj projects used to evaluate the data and create original images.

Each figure is present in editable .ai or .emf formats in addition to the final .pdf, .jpg or .png figure. Each chapter folder contains a readme file for further explanations and instructions. An overview of the figures and how they are produced is given in the following table.

<b>Introduction</b>	please view the corresponding folder
Fig. 1	reprint from the doctoral thesis of A.M. Sommer, [13]
Fig. 2	schematic plot of the set up .svg and .png
<b>Chapter 1</b>	please view the corresponding folder
Fig. 1.1	schematic plot .emf,, .ai, .pdf
Fig. 1.2	schematic plot .emf,, .ai, .pdf
Fig. 1.3	schematic plot .emf,, .ai, .pdf
Fig. 1.4	schematic plot .emf,, .ai, .pdf
Fig. 1.5	schematic plot .emf,, .ai, .pdf
Fig. 1.6	schematic plot .emf,, .ai, .pdf
<b>Chapter 2</b>	please view the corresponding folder
Fig. 2.1a, Fig. 2.1b	.ai .pdf, raw data and plotting .opj
Fig. 2.2a	schematic plot .svg, .pdf
Fig. 2.2b, 2.3, 2.5	.ai, .pdf. raw data and plotting .opj
Fig. 2.4	screen shots .ai, .pdf.

**Chapter 3**

Fig. 3.1a

Fig. 3.1b, 3.2

Fig. 3.3

please view the corresponding folder

reprint from the doctoral thesis of Dr. A.H. Schwarz, [156]

.ai, .pdf, raw data, processing and plotting .opj

.ai, .pdf., raw data and plotting .opj

**Chapter 4****Chapter 5**

Fig. 5.1a

Fig. 5.1b

Fig. 5.2a

Fig. 5.2b

Fig. 5.3

Fig. 5.4

Fig. 5.5

Fig. 5.6

the entire chapter uses reprints from [101] and [123]

please view the corresponding folder

uses data of the Fig. 3.2, .ai, .pdf

schematic plot .emf, .pdf

.ai, .pdf, raw data and plotting .opj

**Chapter 6**

Fig. 6.1

Fig. 6.2

Fig. 6.2

Fig. 6.2

please view the corresponding folder

schematic plot, .ai, .svg

.ai, .pdf, raw data, processing and plotting .opj

.ai, .pdf, raw data, processing and plotting .opj

.ai, .pdf, raw data, processing and plotting .opj

# Bibliography

- [1] Mark Schrope. Marine biology:Lights in the deep. *Nature*, pages 472–474, 2007.
- [2] H. John Caulfield and Shlomi Dolev. Why future supercomputing requires optics. *Nature Photonics*, 4(5):261–263, 2010.
- [3] Ferenc Krausz and Mark I. Stockman. Attosecond metrology: from electron capture to future signal processing. *Nature Photonics*, 8(3):205–213, February 2014.
- [4] WIKIPEDIA - Integrated circuit - [https://en.wikipedia.org/wiki/Integrated\\_circuit](https://en.wikipedia.org/wiki/Integrated_circuit).
- [5] WIKIPEDIA - Moor’s law - [https://en.wikipedia.org/wiki/Moore%27s\\_law](https://en.wikipedia.org/wiki/Moore%27s_law).
- [6] Naimish S. Patel, Katherine L. Hall, and Kristin A. Rauschenbach. Interferometric all-optical switches for ultrafast signal processing. *Applied Optics*, 37(14):2831–2842, May 1998.
- [7] R. Atanasov, A. Haché, J. L. P. Hughes, H. M. Van Driel, and J. E. Sipe. Coherent control of photocurrent generation in bulk semiconductors. *Physical review letters*, 76(10):1703, 1996.
- [8] D. H. Auston. Picosecond optoelectronic switching and gating in silicon. *Applied Physics Letters*, 26(3):101–103, February 1975.
- [9] G. Günter, A. A. Anappara, J. Hees, A. Sell, G. Biasiol, L. Sorba, S. De Liberato, C. Ciuti, A. Tredicucci, A. Leitenstorfer, and R. Huber. Sub-cycle switch-on of ultrastrong light–matter interaction. *Nature*, 458(7235):178–181, March 2009.
- [10] Agustin Schiffrin, Tim Paasch-Colberg, Nicholas Karpowicz, Vadym Apalkov, Daniel Gerster, Sascha Mühlbrandt, Michael Korbman, Joachim Reichert, Martin Schultze, Simon Holzner, Johannes V. Barth, Reinhard Kienberger, Ralph Ernstorfer, Vladislav S. Yakovlev, Mark I. Stockman, and Ferenc Krausz. Optical-field-induced current in dielectrics. *Nature*, 493(7430):70–74, December 2012.
- [11] Aseem Prakash Pati, Imam Setiawan Wahyutama, and Adrian Nikolaus Pfeiffer. Subcycle-resolved probe retardation in strong-field pumped dielectrics. *Nature Communications*, 6:7746, July 2015.

- [12] A. Sommer, E. M. Bothschafter, S. A. Sato, C. Jakubeit, T. Latka, O. Razskazovskaya, H. Fattahi, M. Jobst, W. Schweinberger, V. Shirvanyan, V. S. Yakovlev, R. Kienberger, K. Yabana, N. Karpowicz, M. Schultze, and F. Krausz. Attosecond nonlinear polarization and light–matter energy transfer in solids. *Nature*, 534(7605):86–90, May 2016.
- [13] Annkatrin Sommer. *Ultrafast strong field dynamics in dielectrics*. PhD thesis, lmu, 2015.
- [14] A. J. DeMaria. SELF MODE-LOCKING OF LASERS WITH SATURABLE ABSORBERS. *Applied Physics Letters*, 8(7):174, 1966.
- [15] E.P. Ippen. Passive mode locking of the cw dye laser. *Applied Physics Letters*, 21(8):348, 1972.
- [16] R. L. Fork. Generation of optical pulses shorter than 0.1 psec by colliding pulse mode locking. *Applied Physics Letters*, 38(9):671, 1981.
- [17] J. A. Valdmanis, Richard L. Fork, and James P. Gordon. Generation of optical pulses as short as 27 femtoseconds directly from a laser balancing self-phase modulation, group-velocity dispersion, saturable absorption, and saturable gain. *Optics letters*, 10(3):131–133, 1985.
- [18] David E. Spence, P. Np Kean, and Wilson Sibbett. 60-fsec pulse generation from a self-mode-locked Ti: sapphire laser. *Optics letters*, 16(1):42–44, 1991.
- [19] Chung-Po Huang, Howard Nathel, Melanie T. Asaki, Sterling Backus, Margaret M. Murnane, and Henry C. Kapteyn. 17-fs pulses from a self-mode-locked Ti: sapphire laser. *Optics letters*, 17(18):1289–1291, 1992.
- [20] Melanie T. Asaki, Chung-Po Huang, Dennis Garvey, Jianping Zhou, Henry C. Kapteyn, and Margaret M. Murnane. Generation of 11-fs pulses from a self-mode-locked Ti: sapphire laser. *Optics letters*, 18(12):977–979, 1993.
- [21] Andreas Stingl, Robert Szipöcs, Christian Spielmann, and Ferenc Krausz. Generation of 11-fs pulses from a Ti: sapphire laser without the use of prisms. *Optics letters*, 19(3):204–206, 1994.
- [22] Christian Spielmann, Peter F. Curley, Thomas Brabec, and Ferenc Krausz. Ultra-broadband femtosecond lasers. *Quantum Electronics, IEEE Journal of*, 30(4):1100–1114, 1994.
- [23] A. Stingl, R. Szipöcs, M. Lenzner, Ch Spielmann, and F. Krausz. Sub-10-fs mirror-dispersion-controlled Ti: sapphire laser. *Optics letters*, 20(6):602–604, 1995.
- [24] R. Fluck, I. D. Jung, G. Zhang, F. X. Kärtner, and U. Keller. Broadband saturable absorber for 10-fs pulse generation. *Optics letters*, 21(10):743–745, 1996.

- [25] I. D. Jung, F. X. Kärtner, Nl Matuschek, D. H. Sutter, F. Morier-Genoud, G. Zhang, U. Keller, V. Scheuer, M. Tilsch, and T. Tschudi. Self-starting 6.5-fs pulses from a Ti: sapphire laser. *Optics letters*, 22(13):1009–1011, 1997.
- [26] Uwe Morgner, F. X. Kärtner, Seong-Ho Cho, Yanbei Chen, Hermann A. Haus, James G. Fujimoto, Erich P. Ippen, V. Scheuer, Gregor Angelow, and Theo Tschudi. Sub-two-cycle pulses from a Kerr-lens mode-locked Ti: sapphire laser. *Optics letters*, 24(6):411–413, 1999.
- [27] Dirk H. Sutter, Günter Steinmeyer, Lukas Gallmann, Nicolai Matuschek, François Morier-Genoud, Ursula Keller, V. Scheuer, Gregor Angelow, and Theo Tschudi. Semiconductor saturable-absorber mirror-assisted Kerr-lens mode-locked Ti: sapphire laser producing pulses in the two-cycle regime. *Optics letters*, 24(9):631–633, 1999.
- [28] Richard Ell, Uwe Morgner, F. X. Kärtner, James G. Fujimoto, Erich P. Ippen, V. Scheuer, Gregor Angelow, Theo Tschudi, Max J. Lederer, Alex Boiko, and others. Generation of 5-fs pulses and octave-spanning spectra directly from a Ti: sapphire laser. *Optics letters*, 26(6):373–375, 2001.
- [29] M. Nisoli, S. De Silvestri, G. Valiulis, and A. Varanavicius. Fivefold femtosecond pulse compression by sum frequency generation. *Applied Physics Letters*, 68(25):3540, 1996.
- [30] Mauro Nisoli, S. De Silvestri, O. Svelto, R. Szipöcs, K. Ferencz, Ch Spielmann, S. Sartania, and Ferenc Krausz. Compression of high-energy laser pulses below 5 fs. *Optics letters*, 22(8):522–524, 1997.
- [31] Robert Szipöcs, Christian Spielmann, Ferenc Krausz, and Kárpát Ferencz. Chirped multilayer coatings for broadband dispersion control in femtosecond lasers. *Optics Letters*, 19(3):201–203, 1994.
- [32] Volodymyr Pervak. Recent development and new ideas in the field of dispersive multilayer optics. *Applied optics*, 50(9):C55–C61, 2011.
- [33] A.J. Verhoef, J. Seres, K. Schmid, Y. Nomura, G. Tempea, L. Veisz, and F. Krausz. Compression of the pulses of a Ti:sapphire laser system to 5 femtoseconds at 0.2 terawatt level. *Applied Physics B*, 82(4):513–517, February 2006.
- [34] Eiichi Matsubara, Keisaku Yamane, Taro Sekikawa, and Mikio Yamashita. Generation of 2.6 fs optical pulses using induced-phase modulation in a gas-filled hollow fiber. *JOSA B*, 24(4):985–989, 2007.
- [35] Wolfgang Schweinberger, Annkatrin Sommer, Elisabeth Bothschafter, Jiang Li, Ferenc Krausz, Reinhard Kienberger, and Martin Schultze. Waveform-controlled near-single-cycle milli-joule laser pulses generate sub-10 nm extreme ultraviolet continua. *Optics letters*, 37(17):3573–3575, 2012.

- [36] P.M. Paul, E.S. Toma, P Breger, G Mullot, F Auge, Ph Balcou, H.G. Muller, and P Agostini. Observation of a Train of Attosecond Pulses from High Harmonic Generation. *Science*, 292(5522):1689–1692, June 2001.
- [37] M. Hentschel, R. Kienberger, Ch Spielmann, Georg A. Reider, N. Milosevic, Thomas Brabec, Paul Corkum, Ulrich Heinzmann, Markus Drescher, and Ferenc Krausz. Attosecond metrology. *Nature*, 414(6863):509–513, 2001.
- [38] G. Sansone, E. Benedetti, F. Calegari, C. Vozzi, L. Avaldi, R. Flammini, L. Poletto, P. Villoresi, C. Altucci, R. Velotta, S. Stagira, S. De Silvestri, and M. Nisoli. Isolated Single-Cycle Attosecond Pulses. *Science*, 314(5798):443–446, October 2006.
- [39] Markus Drescher, Michael Hentschel, R. Kienberger, Matthias Uiberacker, Vladislav Yakovlev, Armin Scrinzi, Th Westerwalbesloh, U. Kleineberg, Ulrich Heinzmann, and Ferenc Krausz. Time-resolved atomic inner-shell spectroscopy. *Nature*, 419(6909):803–807, 2002.
- [40] Martin Schultze, Elisabeth M. Bothschafter, Annkatrin Sommer, Simon Holzner, Wolfgang Schweinberger, Markus Fiess, Michael Hofstetter, Reinhard Kienberger, Vadym Apalkov, Vladislav S. Yakovlev, Mark I. Stockman, and Ferenc Krausz. Controlling dielectrics with the electric field of light. *Nature*, 493(7430):75–78, December 2012.
- [41] Olga Smirnova, Yann Mairesse, Serguei Patchkovskii, Nirit Dudovich, David Villeneuve, Paul Corkum, and Misha Yu. Ivanov. High harmonic interferometry of multi-electron dynamics in molecules. *Nature*, 460(7258):972–977, August 2009.
- [42] Ferenc Krausz and Misha Ivanov. Attosecond physics. *Reviews of Modern Physics*, 81(1):163–234, February 2009.
- [43] Shang-Ru Tsai and Michael R. Hamblin. Biological effects and medical applications of infrared radiation. *Journal of Photochemistry and Photobiology B: Biology*, 170:197–207, May 2017.
- [44] Jérôme Kasparian, Miguel Rodríguez, Guillaume Méjean, Jin Yu, Estelle Salmon, H. Wille, R. Bourayou, S. Frey, Y.-B. André, André Mysyrowicz, and others. White-light filaments for atmospheric analysis. *Science*, 301(5629):61–64, 2003.
- [45] A. V. Mitrofanov, A. A. Voronin, D. A. Sidorov-Biryukov, A. Pugžlys, E. A. Stepanov, G. Andriukaitis, T. Flöry, S. Ališauskas, A. B. Fedotov, A. Baltuška, and A. M. Zheltikov. Mid-infrared laser filaments in the atmosphere. *Scientific Reports*, 5(1), July 2015.
- [46] Giulio Cerullo and Sandro De Silvestri. Ultrafast optical parametric amplifiers. *Review of Scientific Instruments*, 74(1):1, 2003.

- [47] Daniil Kartashov, Skirmantas Ališauskas, Audrius Pugžlys, Alexander Voronin, Aleksei Zheltikov, Massimo Petrarca, Pierre B ejot, J er ome Kasparian, Jean-Pierre Wolf, and Andrius Baltuška. White light generation over three octaves by femtosecond filament at 3.9  $\mu\text{m}$  in argon. *Optics letters*, 37(16):3456–3458, 2012.
- [48] C. P. Hauri, Rodrigo B. Lopez-Martens, C. I. Blaga, K. D. Schultz, J. Cryan, R. Chirila, P. Colosimo, G. Doumy, A. M. March, C. Roedig, and others. Intense self-compressed, self-phase-stabilized few-cycle pulses at 2  $\mu\text{m}$  from an optical filament. *Optics letters*, 32(7):868–870, 2007.
- [49] F. Silva, D.R. Austin, A. Thai, M. Baudisch, M. Hemmer, D. Faccio, A. Couairon, and J. Biegert. Multi-octave supercontinuum generation from mid-infrared filamentation in a bulk crystal. *Nature Communications*, 3:807, May 2012.
- [50] Pierre Tournois. Acousto-optic programmable dispersive filter for adaptive compensation of group delay time dispersion in laser systems. *Optics communications*, 140(4):245–249, 1997.
- [51] Andrew M. Weiner, Daniel E. Leaird, Jay S. Patel, and John R. Wullert. Programmable femtosecond pulse shaping by use of a multielement liquid-crystal phase modulator. *Optics letters*, 15(6):326–328, 1990.
- [52] R. L. Fork, O. E. Martinez, and J. P. Gordon. Negative dispersion using pairs of prisms. *Optics letters*, 9(5):150–152, 1984.
- [53] R. Szip ocs, A. K oh azi-Kis, S. Lak o, P. Apai, A.P. Kov acs, G. DeBell, L. Mott, A.W. Louderback, A.V. Tikhonravov, and M.K. Trubetskov. Negative dispersion mirrors for dispersion control in femtosecond lasers: chirped dielectric mirrors and multicavity Gires–Tournois interferometers. *Applied Physics B*, 70(S1):S51–S57, June 2000.
- [54] F. X. K artner, N. Matuschek, T. Schibli, U. Keller, H. A. Haus, C. Heine, R. Morf, V. Scheuer, M. Tilsch, and T. Tschudi. Design and fabrication of double-chirped mirrors. *Optics letters*, 22(11):831–833, 1997.
- [55] F. X. K artner, U. Morgner, R. Ell, T. Schibli, J. G. Fujimoto, E. P. Ippen, V. Scheuer, G. Angelow, and T. Tschudi. Ultrabroadband double-chirped mirror pairs for generation of octave spectra. *JOSA B*, 18(6):882–885, 2001.
- [56] A. Wirth, M. T. Hassan, I. Grguras, J. Gagnon, A. Moulet, T. T. Luu, S. Pabst, R. Santra, Z. A. Alahmed, A. M. Azzeer, V. S. Yakovlev, V. Pervak, F. Krausz, and E. Goulielmakis. Synthesized Light Transients. *Science*, 334(6053):195–200, October 2011.
- [57] M. Th. Hassan, A. Wirth, I. Grguraš, A. Moulet, T. T. Luu, J. Gagnon, V. Pervak, and E. Goulielmakis. Invited Article: Attosecond photonics: Synthesis and control of light transients. *Review of Scientific Instruments*, 83(11):111301, 2012.

- [58] Cristian Manzoni, Oliver D. Mücke, Giovanni Cirimi, Shaobo Fang, Jeffrey Moses, Shu-Wei Huang, Kyung-Han Hong, Giulio Cerullo, and Franz X. Kärtner. Coherent pulse synthesis: towards sub-cycle optical waveforms: Coherent pulse synthesis: towards sub-cycle optical waveforms. *Laser & Photonics Reviews*, 9(2):129–171, March 2015.
- [59] Günther Krauss, Sebastian Lohss, Tobias Hanke, Alexander Sell, Stefan Eggert, Rupert Huber, and Alfred Leitenstorfer. Synthesis of a single cycle of light with compact erbium-doped fibre technology. *Nature Photonics*, 4(1):33–36, January 2010.
- [60] Oliver D. Mücke, Shaobo Fang, Giovanni Cirimi, Giulio Maria Rossi, Shih-Hsuan Chia, Hong Ye, Yudong Yang, Roland Mainz, Cristian Manzoni, Paolo Farinello, Giulio Cerullo, and Franz X. Kartner. Toward Waveform Nonlinear Optics Using Multimillijoule Sub-Cycle Waveform Synthesizers. *IEEE Journal of Selected Topics in Quantum Electronics*, 21(5):1–12, September 2015.
- [61] Hanieh Fattahi, Helena G. Barros, Martin Gorjan, Thomas Nubbemeyer, Bidoor Alsaif, Catherine Y. Teisset, Marcel Schultze, Stephan Prinz, Matthias Haefner, Moritz Ueffing, Ayman Alismail, Lénárd Vámos, Alexander Schwarz, Oleg Pronin, Jonathan Brons, Xiao Tao Geng, Gunnar Arisholm, Marcelo Ciappina, Vladislav S. Yakovlev, Dong-Eon Kim, Abdallah M. Azzeer, Nicholas Karpowicz, Dirk Sutter, Zsuzsanna Major, Thomas Metzger, and Ferenc Krausz. Third-generation femtosecond technology. *Optica*, 1(1):45, July 2014.
- [62] C Iaconis and I.A. Walmsley. Spectral phase interferometry for direct electric-field reconstruction of ultrashort optical pulses. *Optics Letters*, 23(10):792, May 1998.
- [63] Rick Trebino, Kenneth W. DeLong, David N. Fittinghoff, John N. Sweetser, Marco A. Krumbügel, Bruce A. Richman, and Daniel J. Kane. Measuring ultrashort laser pulses in the time-frequency domain using frequency-resolved optical gating. *Review of Scientific Instruments*, 68(9):3277–3295, 1997.
- [64] Miguel Miranda, Cord Arnold, Thomas Fordell, F. Silva, Benjamin Alonso, Rosa Weigand, Anne L’Huillier, and Helder Crespo. Characterization of broadband few-cycle laser pulses with the d-scan technique. *Optics Express*, 20(17):18732–18743, August 2012.
- [65] J. Itatani, F. Quéré, G. L. Yudin, M. Yu. Ivanov, F. Krausz, and P. B. Corkum. Attosecond Streak Camera. *Physical Review Letters*, 88(17), April 2002.
- [66] Reinhard Kienberger, Eleftherios Goulielmakis, M Uiberacker, A. Baltuska, Vladislav Yakovlev, F Bammer, A Scrinzi, Th Westerwalbesloh, Ulf Kleineberg, Ulrich Heinzmann, Markus Drescher, and Ferenc Krausz. Atomic transient recorder. *Nature*, 427(6977):817–821, February 2004.

- [67] Q. Wu and X. C. Zhang. Free-space electro-optic sampling of terahertz beams. *Applied Physics Letters*, 67(24):3523–3525, December 1995.
- [68] A. Leitenstorfer, S. Hunsche, J. Shah, M. C. Nuss, and W. H. Knox. Detectors and sources for ultrabroadband electro-optic sampling: Experiment and theory. *Applied Physics Letters*, 74(11):1516–1518, March 1999.
- [69] Sabine Keiber, Shawn Sederberg, Alexander Schwarz, Michael Trubetskov, Volodymyr Pervak, Ferenc Krausz, and Nicholas Karpowicz. Electro-optic sampling of near-infrared waveforms. *Nature Photonics*, 10(3):159–162, January 2016.
- [70] Theodore H. Maiman. Stimulated Optical Radiation in Ruby. *Nature*, 187:493–494, August 1960.
- [71] eg PA Franken, Alan E. Hill, CW el Peters, and G. Weinreich. Generation of optical harmonics. *Physical Review Letters*, 7(4):118, 1961.
- [72] Nicolaas Bloembergen and P. S. Pershan. Light waves at the boundary of nonlinear media. *Physical Review*, 128(2):606, 1962.
- [73] Robert W. Boyd. *Nonlinear Optics*. Burlington: Academic Press, 3rd edition edition, 2008.
- [74] H. A. Macleod. Thin-film Optical filter. In E. Roy Pike and Robert G. W. Brown, editors, *Thin-film optical filter, fourth edition*. CRC Press, Boca Raton, FL, 2010.
- [75] Philippe Antoine, Anne L’huillier, and Maciej Lewenstein. Attosecond pulse trains using high-order harmonics. *Physical Review Letters*, 77(7):1234, 1996.
- [76] Pascal Salières and Maciej Lewenstein. Generation of ultrashort coherent XUV pulses by harmonic conversion of intense laser pulses in gases: towards attosecond pulses. *Measurement Science and Technology*, 12(11):1818, 2001.
- [77] Maciej Lewenstein, Ph Balcou, M. Yu Ivanov, Anne L’huillier, and Paul B. Corkum. Theory of high-harmonic generation by low-frequency laser fields. *Physical Review A*, 49(3):2117, 1994.
- [78] Pierre Agostini and Louis F DiMauro. The physics of attosecond light pulses. *Reports on Progress in Physics*, 67(6):813–855, June 2004.
- [79] Jeffrey L. Krause, Kenneth J. Schafer, and Kenneth K. Kulander. High-Order Harmonic Generation from Atoms and Ions in the High Intensity Regime. *Physical Review Letters*, 68(24), June 1992.
- [80] Ch Spielmann, N. H. Burnett, S. Sartania, R. Koppitsch, M. Schnürer, C. Kan, M. Lenzner, P. Wobrauschek, and F. Krausz. Generation of coherent X-rays in the water window using 5-femtosecond laser pulses. *Science*, 278(5338):661–664, 1997.

- [81] T. Popmintchev, M.-C. Chen, D. Popmintchev, P. Arpin, S. Brown, S. Alisauskas, G. Andriukaitis, T. Balciunas, O. D. Mücke, A. Pugzlys, A. Baltuska, B. Shim, S. E. Schrauth, A. Gaeta, C. Hernandez-Garcia, L. Plaja, A. Becker, A. Jaron-Becker, M. M. Murnane, and H. C. Kapteyn. Bright Coherent Ultrahigh Harmonics in the keV X-ray Regime from Mid-Infrared Femtosecond Lasers. *Science*, 336(6086):1287–1291, June 2012.
- [82] M.-C. Chen, C. Mancuso, C. Hernandez-Garcia, F. Dollar, B. Galloway, D. Popmintchev, P.-C. Huang, B. Walker, L. Plaja, A. A. Jaro-Becker, A. Becker, M. M. Murnane, H. C. Kapteyn, and T. Popmintchev. Generation of bright isolated attosecond soft X-ray pulses driven by multicycle midinfrared lasers. *Proceedings of the National Academy of Sciences*, 111(23):E2361–E2367, June 2014.
- [83] Nobuhisa Ishii, Keisuke Kaneshima, Kenta Kitano, Teruto Kanai, Shuntaro Watanabe, and Jiro Itatani. Carrier-envelope phase-dependent high harmonic generation in the water window using few-cycle infrared pulses. *Nature Communications*, 5, February 2014.
- [84] C. Vozzi, G. Cerullo, C. Manzoni, E. Benedetti, F. Calegari, G. Sansone, S. De Silvestri, M. Nisoli, and G. Cerullo. High-energy, few-optical-cycle pulses at 1.5  $\mu\text{m}$  with passive carrier-envelope phase stabilization. *Optics Express*, 14(21):10109–10116, 2006.
- [85] G. Cerullo, A. Baltuška, O.D. Mücke, and C. Vozzi. Few-optical-cycle light pulses with passive carrier-envelope phase stabilization. *Laser & Photonics Reviews*, 5(3):323–351, May 2011.
- [86] Xun Gu, Gilad Marcus, Yunpei Deng, Thomas Metzger, Catherine Teisset, Nobuhisa Ishii, Takao Fuji, Andrius Baltuska, Rytis Butkus, Volodymyr Pervak, and others. Generation of carrier-envelope-phase-stable 2-cycle 740- $\mu\text{J}$  pulses at 2.1- $\mu\text{m}$  carrier wavelength. *Optics express*, 17(1):62–69, 2009.
- [87] Yunpei Deng, Alexander Schwarz, Hanieh Fattahi, Moritz Ueffing, Xun Gu, Marcus Ossiander, Thomas Metzger, Volodymyr Pervak, Hideki Ishizuki, Takunori Taira, and others. Carrier-envelope-phase-stable, 1.2 mJ, 1.5 cycle laser pulses at 2.1  $\mu\text{m}$ . *Optics letters*, 37(23):4973–4975, 2012.
- [88] Alexander Schwarz, Moritz Ueffing, Yunpei Deng, Xun Gu, Hanieh Fattahi, Thomas Metzger, Marcus Ossiander, Ferenc Krausz, and Reinhard Kienberger. Active stabilization for optically synchronized optical parametric chirped pulse amplification. *Optics Letters*, 20(5), 2012.
- [89] Ahmed H. Zewail. Femtochemistry: Atomic-Scale Dynamics of the Chemical Bond <sup>†</sup>. *The Journal of Physical Chemistry A*, 104(24):5660–5694, June 2000.
- [90] P. B. Corkum and Ferenc Krausz. Attosecond science. *Nature Physics*, 3(6):381–387, 2007.

- [91] M. Nisoli, S. De Silvestri, and O. Svelto. Generation of high energy 10 fs pulses by a new pulse compression technique. *Applied Physics Letters*, 68(20):2793, 1996.
- [92] Takayoshi Kobayashi and Andrius Baltuska. Sub-5 fs pulse generation from a noncollinear optical parametric amplifier. *Measurement Science and Technology*, 13(11):1671, 2002.
- [93] Andrius Baltuška, Maxim S. Pshenichnikov, and Douwe A. Wiersma. Amplitude and phase characterization of 4.5-fs pulses by frequency-resolved optical gating. *Optics Letters*, 23(18):1474–1476, 1998.
- [94] Hanieh Fattahi, Haochuan Wang, Ayman Alismail, Gunnar Arisholm, Vladimir Pervak, Abdallah M. Azzeer, and Ferenc Krausz. Near-PHz-bandwidth, phase-stable continua generated from a Yb:YAG thin-disk amplifier. *Optics Express*, 24(21):24337, October 2016.
- [95] O.D. Mücke, S. Alisauskas, A.J. Verhoef, A. Pugžlys, A Baltuška, Valerius Smilgevičius, Jonas Pocius, L. Gininas, R. Danielius, and Nicolas Forget. Self-compression of millijoule 1.5 mJ pulses. *Optics Letters*, 34(16):2498–2500, August 2009.
- [96] Bruno E. Schmidt, Pierre Béjot, Mathieu Giguère, Andrew D. Shiner, Carlos Trallero-Herrero, Éric Bisson, Jérôme Kasparian, Jean-Pierre Wolf, David M. Villeneuve, Jean-Claude Kieffer, Paul B. Corkum, and François Légaré. Compression of 1.8  $\mu\text{m}$  laser pulses to sub two optical cycles with bulk material. *Applied Physics Letters*, 96(12):121109, 2010.
- [97] Guangyu Fan, Tadas Balciunas, Tsuneto Kanai, Giedrius Andriukaitis, Bruno E. Schmidt, François Légaré, and Andrius Baltuska. Hollow-Core-Waveguide Compression of Multi-mJ CEP-Stable 3.2- $\mu\text{m}$  Pulses. In *International Conference on Ultrafast Phenomena*, pages UTu2A–4. Optical Society of America, 2016.
- [98] Mathieu Giguère, Bruno E. Schmidt, Andrew D. Shiner, Marie-Andrée Houle, Heidi C. Bandulet, Gabriel Tempea, David M. Villeneuve, Jean-Claude Kieffer, and François Légaré. Pulse compression of submillijoule few-optical-cycle infrared laser pulses using chirped mirrors. *Optics letters*, 34(12):1894–1896, 2009.
- [99] Marco Cassataro, David Novoa, Mehmet Can Günendi, Nitin Edavalath, Michael H. Frosz, John C. Travers, and Philip S. Russell. Deep-Ultraviolet to Mid-Infrared Supercontinuum in Single-Ring Hollow-Core Photonic Crystal Fiber. In *International Conference on Ultrafast Phenomena*, pages UW4A–34. Optical Society of America, 2016.
- [100] Vladimir Pervak, Olga Razskazovskaya, Ivan B. Angelov, Konstantin L. Vodopyanov, and Michael Trubetskov. Dispersive mirror technology for ultrafast lasers in the range 220–4500 nm. *Advanced Optical Technologies*, 3(1), January 2014.

- [101] O. Razskazovskaya, F. Krausz, and V. Pervak. Multilayer coatings for femto- and attosecond technology. *Optica*, 4(1):129, January 2017.
- [102] Jianping Zhou, Ivan P. Christov, Greg Taft, Chung-Po Huang, Margaret M. Murnane, and Henry C. Kapteyn. Pulse evolution in a broad-bandwidth Ti: sapphire laser. *Optics letters*, 19(15):1149–1151, 1994.
- [103] E.B. Treacy. Optical pulse compression with diffraction gratings. QE-5(9), September 1969.
- [104] B. Golubovic, R. R. Austin, M. K. Steiner-Shepard, M. K. Reed, Scott A. Diddams, D. J. Jones, and Amelia G. Van Engen. Double Gires—Tournois interferometer negative-dispersion mirrors for use in tunable mode-locked lasers. *Optics letters*, 25(4):275–277, 2000.
- [105] Shih-Hsuan Chia, Giovanni Cirmi, Shaobo Fang, Giulio M. Rossi, Oliver D. Mücke, and Franz X. Kärtner. Two-octave-spanning dispersion-controlled precision optics for sub-optical-cycle waveform synthesizers. *Optica*, 1(5):315, November 2014.
- [106] M. Th. Hassan, T. T. Luu, A. Moulet, O. Raskazovskaya, P. Zhokhov, M. Garg, N. Karpowicz, A. M. Zheltikov, V. Pervak, F. Krausz, and E. Goulielmakis. Optical attosecond pulses and tracking the nonlinear response of bound electrons. *Nature*, 530(7588):66–70, February 2016.
- [107] Gabriel Tempea, Ferenc Krausz, Christian Spielmann, and Kárpát Ferencz. Dispersion control over 150 THz with chirped dielectric mirrors. *Selected Topics in Quantum Electronics, IEEE Journal of*, 4(2):193–196, 1998.
- [108] Robert Szipöcs. Dispersive properties of dielectric laser mirrors and their use in femtosecond pulse lasers. 2000.
- [109] N. Matuschek, L. Gallmann, D.H. Sutter, G. Steinmeyer, and U. Keller. Back-side-coated chirped mirrors with ultra-smooth broadband dispersion characteristics. *Applied Physics B: Lasers and Optics*, 71(4):509–522, October 2000.
- [110] Gabriel Tempea, Vladislav Yakovlev, Biljana Bacovic, Ferenc Krausz, and Kárpát Ferencz. Tilted-front-interface chirped mirrors. *JOSA B*, 18(11):1747–1750, 2001.
- [111] Nicolai Matuschek, Franz X. Kartner, and Ursula Keller. Analytical design of double-chirped mirrors with custom-tailored dispersion characteristics. *Quantum Electronics, IEEE Journal of*, 35(2):129–137, 1999.
- [112] Nicolai Matuschek, Franz X. Kärtner, and Ursula Keller. Theory of double-chirped mirrors. *Selected Topics in Quantum Electronics, IEEE Journal of*, 4(2):197–208, 1998.

- [113] V. Pervak, I. Ahmad, M. K. Trubetskov, A. V. Tikhonravov, and F. Krausz. Double-angle multilayer mirrors with smooth dispersion characteristics. *Optics express*, 17(10):7943–7951, 2009.
- [114] Alexander V. Tikhonravov, Michael K. Trubetskov, and Gary W. DeBell. Application of the needle optimization technique to the design of optical coatings. *Applied optics*, 35(28):5493–5508, 1996.
- [115] A. V. Tikhonravov, M. K. Trubetskov, and G. W. DeBell. Optical coating design approaches based on the needle optimization technique. *Applied optics*, 46(5):704–710, 2007.
- [116] Alexander V. Tikhonravov and Michael K. Trubetskov. Modern design tools and a new paradigm in optical coating design. *Applied optics*, 51(30):7319–7332, 2012.
- [117] V. Pervak, A.V. Tikhonravov, M.K. Trubetskov, S. Naumov, F. Krausz, and A. Apolonski. 1.5-octave chirped mirror for pulse compression down to sub-3 fs. *Applied Physics B*, 87(1):5–12, March 2007.
- [118] Michelle Rhodes, Günter Steinmeyer, and Rick Trebino. Standards for ultrashort-laser-pulse-measurement techniques and their consideration for self-referenced spectral interferometry. *Applied Optics*, 53(16):D1, June 2014.
- [119] Frederic Verluise, Vincent Laude, Z. Cheng, Ch Spielmann, and Pierre Tournois. Amplitude and phase control of ultrashort pulses by use of an acousto-optic programmable dispersive filter: pulse compression and shaping. *Optics Letters*, 25(8):575–577, 2000.
- [120] M.N. Polyanskiy. Polyanskiy, M.N. - <http://refractiveindex.info>.
- [121] Christopher A. Rivera, Stephen E. Bradforth, and Gabriel Tempea. Gires-Tournois interferometer type negative dispersion mirrors for deep ultraviolet pulse compression. *Optics express*, 18(18):18615–18624, 2010.
- [122] V. Pervak, F. Krausz, and A. Apolonski. Hafnium oxide thin films deposited by reactive middle-frequency dual-magnetron sputtering. *Thin Solid Films*, 515(20-21):7984–7989, July 2007.
- [123] O. Razskazovskaya, T. T. Luu, M. Trubetskov, E. Goulielmakis, and V. Pervak. Nonlinear absorbance in dielectric multilayers. *Optica*, 2(9):803, September 2015.
- [124] Thomas Brabec and Ferenc Krausz. Intense few-cycle laser fields: Frontiers of nonlinear optics. *Reviews of Modern Physics*, 72(2):545, 2000.
- [125] Michael Scalora, Jonathan P. Dowling, Charles M. Bowden, and Mark J. Bloemer. Optical limiting and switching of ultrashort pulses in nonlinear photonic band gap materials. *Physical review letters*, 73(10):1368, 1994.

- [126] Marin Soljačić and John D. Joannopoulos. Enhancement of nonlinear effects using photonic crystals. *Nature materials*, 3(4):211–219, 2004.
- [127] Robert W. Boyd and John E. Sipe. Nonlinear optical susceptibilities of layered composite materials. *JOSA B*, 11(2):297–303, 1994.
- [128] Zi-Ming Meng, Fei Qin, and Zhi-Yuan Li. Ultrafast all-optical switching in one-dimensional semiconductor–polymer hybrid nonlinear photonic crystals with relaxing Kerr nonlinearity. *Journal of Optics*, 14(6):065003, June 2012.
- [129] Nick Lepeshkin, Aaron Schweinsberg, Giovanni Piredda, Ryan Bennink, and Robert Boyd. Enhanced Nonlinear Optical Response of One-Dimensional Metal-Dielectric Photonic Crystals. *Physical Review Letters*, 93(12), September 2004.
- [130] George L. Fischer, Robert W. Boyd, Russell J. Gehr, Samson A. Jenekhe, John A. Osaheni, J. E. Sipe, and Laura A. Weller-Brophy. Enhanced nonlinear optical response of composite materials. *Physical review letters*, 74(10):1871, 1995.
- [131] Richard Lepkowicz. Nonlinear photonic crystals for passive switches. *SPIE Newsroom*, 2008.
- [132] Eva Franke, C. L. Trimble, M. J. DeVries, J. A. Woollam, M. Schubert, and F. Frost. Dielectric function of amorphous tantalum oxide from the far infrared to the deep ultraviolet spectral region measured by spectroscopic ellipsometry. *Journal of Applied Physics*, 88(9):5166, 2000.
- [133] O. Anderson. Silicon Oxides. In H. Bach and D. Krause, editors, *Thin films on glass*. Springer, Berlin Heidelberg, 1997.
- [134] V. Pervak, V. Fedorov, Yu. A. Pervak, and M. Trubetskov. Empirical study of the group delay dispersion achievable with multilayer mirrors. *Optics Express*, 21(15):18311, July 2013.
- [135] Chao-Yi Tai. Waveguide using Self-Phase Modulation.
- [136] M. Sheik-Bahae, D. J. Hagan, and E. W. Van Stryland. Dispersion and band-gap scaling of the electronic Kerr effect in solids associated with two-photon absorption. *Physical review letters*, 65(1):96, 1990.
- [137] Mansoor Sheik-Bahae, D. C. Hutchings, D. J. Hagan, and E. W. Van Stryland. Dispersion of bound electronic nonlinear refraction in solids. *IEEE Journal of Quantum Electronics*, 27(6):1296–1309, June 1991.
- [138] D. C. Hutchings, M. Sheik-Bahae, D. J. Hagan, and E. W. Van Stryland. Kramers-Krönig relations in nonlinear optics. *Optical and Quantum Electronics*, 24(1):1–30, 1992.

- [139] S. A. Furman & A. V. Tikhonravov. Basics of Optics of Multilayer systems. In xxx, editor, *Basics of Optics of Multilayer systems*. Editions Frontieres, xxxL, 1992.
- [140] Richard DeSalvo, Ali A. Said, David J. Hagan, Eric W. Van Stryland, and Mansoor Sheik-Bahae. Infrared to ultraviolet measurements of two-photon absorption and  $n_2$  in wide bandgap solids. *Quantum Electronics, IEEE Journal of*, 32(8):1324–1333, 1996.
- [141] Richard Lee Sutherland. *Handbook of nonlinear optics*. Number 82 in Optical engineering. Marcel Dekker, New York, 2nd ed., rev. and expanded edition, 2003.
- [142] John N. Sweetser, David N. Fittinghoff, and Rick Trebino. Transient-grating frequency-resolved optical gating. *Optics letters*, 22(8):519–521, 1997.
- [143] N. Demirdöven, M. Khalil, O. Golonzka, and A. Tokmakoff. Dispersion compensation with optical materials for compression of intense sub-100-fs mid-infrared pulses. *Optics letters*, 27(6):433–435, 2002.
- [144] Julie A. Gruetzmacher and Norbert F. Scherer. Few-cycle mid-infrared pulse generation, characterization, and coherent propagation in optically dense media. *Review of Scientific Instruments*, 73(6):2227, 2002.
- [145] Martin Friz and Friedrich Waibel. Coating materials. In *Optical interference coatings*, pages 105–130. Springer, 2003.
- [146] Andrius Baltuska, Th. Udem, M Uiberacker, M. Hentschel, Eleftherios Goulielmakis, Ch Gohle, Ronald Holzwarth, V. S. Yakovlev, A Scrinzi, T.W. Haensch, and F Krausz. Attosecond control of electronic processes by intense light fields. *Nature*, 421(6923):611–615, February 2003.
- [147] E. Goulielmakis, M. Schultze, M. Hofstetter, V. S. Yakovlev, J. Gagnon, M. Uiberacker, A. L. Aquila, E. M. Gullikson, D. T. Attwood, R. Kienberger, F. Krausz, and U. Kleineberg. Single-Cycle Nonlinear Optics. *Science*, 320(5883):1614–1617, June 2008.
- [148] S. E. Harris and A. V. Sokolov. Subfemtosecond pulse generation by molecular modulation. *Physical review letters*, 81(14):2894, 1998.
- [149] Robert K. Shelton, Long-Sheng Ma, Henry C. Kapteyn, Margaret M. Murnane, John L. Hall, and Jun Ye. Phase-coherent optical pulse synthesis from separate femtosecond lasers. *Science*, 293(5533):1286–1289, 2001.
- [150] L. Gallmann, D.H. Sutter, N. Matuschek, G. Steinmeyer, and U. Keller. Techniques for the characterization of sub-10-fs optical pulses: a comparison:. *Applied Physics B*, 70(S1):S67–S75, June 2000.

- 
- [151] Alexander Sell, Rüdiger Scheu, Alfred Leitenstorfer, and Rupert Huber. Field-resolved detection of phase-locked infrared transients from a compact Er: fiber system tunable between 55 and 107 THz. *Applied Physics Letters*, 93(25):251107, December 2008.
- [152] Eleftherios Goulielmakis, Matthias Uiberacker, Reinhard Kienberger, Andrius Baltuska, Vladislav Yakovlev, Armin Scrinzi, Th Westerwalbesloh, U. Kleineberg, Ulrich Heinzmann, Markus Drescher, and others. Direct measurement of light waves. *Science*, 305(5688):1267–1269, 2004.
- [153] Kyung Taec Kim, Chunmei Zhang, Andrew D. Shiner, Bruno E. Schmidt, François Légaré, D. M. Villeneuve, and P. B. Corkum. Petahertz optical oscilloscope. *Nature Photonics*, 7(12):958–962, November 2013.
- [154] Tim Paasch-Colberg, Agustin Schiffrin, Nicholas Karpowicz, Stanislav Kruchinin, Özge Sağlam, Sabine Keiber, Olga Razskazovskaya, Sascha Mühlbrandt, Ali Alnaser, Matthias Kübel, Vadym Apalkov, Daniel Gerster, Joachim Reichert, Tibor Wittmann, Johannes V. Barth, Mark I. Stockman, Ralph Ernstorfer, Vladislav S. Yakovlev, Reinhard Kienberger, and Ferenc Krausz. Solid-state light-phase detector. *Nature Photonics*, 8(3):214–218, January 2014.
- [155] Michael Porer, Jean-Michel Ménard, and Rupert Huber. Shot noise reduced terahertz detection via spectrally postfiltered electro-optic sampling. *Optics Letters*, 39(8):2435, April 2014.
- [156] Alexander Schwarz. *Few-cycle phase-stable infrared OPCPA*. PhD thesis.

## And the thank you goes to...

Well, after so many years in MPQ and in Munich there are truly many names that come up when I think of all the good years spent here, I hope I won't forget anyone or at least no one who has even a slight chance or interest in reading this :)

First of all, I should thank Prof. Dr. Ferenc Krausz for taking me on board of his group and providing an opportunity to work with all the wonderful people, I've worked with. A great thanks to the group's and institute's administration and IT represented by Frau Wild, Simone Mann, Franziska Hoss, Klaus Franke, Chantal Lavaglio, Karolina Schneider, Monika Priebe and Mr. Grotte that were always very friendly and helpful. I sincerely appreciate this.

From my time in LMU, of course, I remember with a warm smile our office 201 squat of Ivan, Simon (who didn't like Lena's ear rings) and Daniel (who was able to sell snow in winter to an eskimo). That was a great time we had together. Can't forget the skiing buddies group made of Henning, Kellie and occasionally Waldemar too. Our bus trips to Alps were always so fun and our Oktoberfests and Starkbierfests together with Matt, Lena and Lamia even funner :D I promise to keep all the videos and pictures securely stored forever ;)

Generally, the LMU guys: Lord Lahme, Niko, Tobi, Dominik, Alex and Casey, Andrey, Oleg, Marcus, Jonathan - thank you for the beer o'clocks and the funny memories we made together.

Vielen Dank zu den Reinraum Technikern Bernd und Sigi für die Unterstützung und Mithilfe mit der Helios Anlage. Das hat mich immer gefreut mit euch im Labor zu arbeiten. Special thanks to Tobias Kleinheiz and Martin Triphan for their support on the MPQ side.

A huge hug to the ATLAS duo of Johannes and Kostja, you are the best! Not much more I can say here.

From the MPQ time, I of course foremost thank the "Lunch with the cool kids" table members: Matt, Clemens, Dima, Shawn and Vlad for a great team spirit, good time in the Lab and outside of it.

I may not forget the attosecond gentlemen and a lady: Martin, Marcus, Flo, Tobi and Annka. Gentlemen, you always treated me like a lady and I always loved it. Martin bugged me so much with my missing articles, but I have to say honestly that in the end I really started to pay more attention to them, so I hope Martin is at least a little bit proud of me. A big hug to Marcus for translating the "Abstract" into German for me. No cakes or ponies of the world are enough to pay you back ;)

I'd also say thank you to the cafeteria people Julia and Co. The food might not always have been great, but their Borsh soup revived me many times (I truly recommend it) and they are always friendly.

Cheers to Mathias, Andy and Alex K. for being excellent buddies and colleagues and to Rivas and Alex G. for being the awesomest office-mates ever. A special love goes to DC, it is impossible to not love him :)

A hug to the "bonsai WG" members: Nico, Henrik, Ruben and Andresh for proving that the theory guys are not all nerds and for providing me an occasional shelter.

A very special thank you to Sabine. Her great spirit, persistence and incredible hard working were always so motivating to me.

A thank you from all my heart to Nick, Dr. Hani, Amu, Ivan, Guido, Amy Lin, Trung and Vladimir - the colleagues who became my beloved and most cherished friends. I am so happy that those years brought you in my life.

Thank you, Nick and Vladimir, for all the work we have accomplished. Without you there, I wouldn't be able.

My heart is always with the "Stone age community" members of Hortensienstr. 2 WG: Stefania, Tobi, Luca, Christoph, Emilie, Antoine, Antonin and Agustin. For two years we were the family that one can only dream of!

To my all beloved friends and colleagues, thank you, these years with you were so incredible! That is why this thesis took me 7 years to accomplish, you gave me so much motivation to stick around :p

Vielen herzlichen und lieben dank an den Familien Droste und Harms/Uben. Danke daß ihr mich so einfach und mit so viel Freude und Liebe angenommen habt. Danke für die Unterstützung aller Art durch allen vergangenen Jahren. Ich werde das nie vergessen.

Большое спасибо моей семье, особенно дедушке и папе. Вы всегда были и будете моим примером людей науки. Большое спасибо Марине за неотступную дружескую поддержку. Владюха, ты следующий :p

Большое спасибо дяде Коле за беззвучную,но непоколебимую поддержку и моей маме - благодаря тебе я тот человек, кем являюсь.

# CURRICULUM VITAE

## PERSONAL INFORMATION

Name OLGA, Razskazovskaya  
Adresse Rue des Brevards 9  
Neuchâtel, 2000, Switzerland  
Telephone +41-5446656  
E-Mail olga.razskazovskaya@unine.ch  
Nationality Russian  
Date of birth 23.11.1984



## PROFESSION

- ▷ Current occupation Scientific collaborator
- Period 08.2017–present
- Employer **University of Neuchâtel, Faculty of Science**  
Avenue de Bellevaux 51, Neuchâtel, 2000, Switzerland  
Advanced multilayer thin-film coatings • THz sources
- Project

## EDUCATION

- ▷ Period 2010–2017
- Acquired qualification **Ph.D. in Physics**
- University Ludwig Maximilian University of Munich
- ▷ Period 2005–2007
- Acquired qualification **M.Sc. in Engineering**
- University Moscow State Technological University named after N.E. Baumann
- ▷ Period 2001–2005
- Acquired qualification **B.Sc. in Engineering**
- University Moscow State Technological University named after N.E. Baumann

## RESEARCH

- ▷ Research Interests Multilayer coatings for ultrafast optics, femto- and attosecond applications: design and manufacturing • Pulse compression • Waveform synthesis
- ▷ Research projects Advanced broadband multilayer dispersive optics • THz sources and spectroscopy

## PUBLICATIONS



- **O. Razskazovskaya**, M. Ossiander, F. Siegrist, V. Pervak and M. Schultze, "Carrier frequency tuning of few-cycle light pulses by Broadband Attenuating Mirrors (BAM)", Applied Optics, accepted.
- T. Latka, V. Shirvanyan, M. Ossiander, **O. Razskazovskaya**, A. Guggenmos, M. Jobst, M. Fiess, S. Holzner, A. Sommer, M. Schultze, C. Jakubeit, J. Riemensberger, B. Bernhardt, W. Helml, F. Gatti, B. Lasorne, D. Lauvergnat, P. Decleva, G. J. Halasz, A. Vibok, R. Kienberger, "Few-Femtosecond Wave Packet Revivals in Ozone", Nature Physics, submitted.
- Rivas, D. E. and Borot, A. and Cardenas, D. E. and Marcus, G. and Gu, X. and Herrmann, D. and Xu, J. and Tan, J. and Kormin, D. and Ma, G. and Dallari, W. and Tsakiris, G. D. and Földes, I. B. and Chou, S.-w. and Weidman, M. and Bergues, B. and Wittmann, T. and Schröder, H. and Tzallas, P. and Charalambidis, D. and **Razskazovskaya, O.** and Pervak, V. and Krausz, F. and Veisz, L, "Next Generation Driver for Attosecond and Laser-plasma Physics", Scientific Reports 7, 1 (2017).
- **O. Razskazovskaya**, F. Krausz, and V. Pervak, "Multilayer coatings for femto- and attosecond technology," Optica 4, 129 (2017).
- **O. Razskazovskaya**, M. T. Hassan, T. Luu, E. Goulielmakis, and V. Pervak, "Efficient broadband highly dispersive HfO<sub>2</sub>/SiO<sub>2</sub> multilayer mirror for pulse compression in near ultraviolet," Optics Express 24, 13628 (2016).
- A. Sommer, E. M. Bothschafter, S. A. Sato, C. Jakubeit, T. Latka, **O. Razskazovskaya**, H. Fattahi, M. Jobst, W. Schweinberger, V. Shirvanyan, V. S. Yakovlev, R. Kienberger, K. Yabana, N. Karpowicz, M. Schultze, and F. Krausz, "Attosecond nonlinear polarization and light-matter energy transfer in solids," Nature 534, 86–90 (2016).
- M. T. Hassan, T. T. Luu, A. Moulet, **O. Raskazovskaya**, P. Zhokhov, M. Garg, N. Karpowicz, A. M. Zheltikov, V. Pervak, F. Krausz, and E. Goulielmakis, "Optical attosecond pulses and tracking the nonlinear response of bound electrons," Nature 530, 66–70 (2016).
- **O. Razskazovskaya**, T. T. Luu, M. Trubetskov, E. Goulielmakis, and V. Pervak, "Nonlinear absorbance in dielectric multilayers," Optica 2, 803 (2015).
- **O. Razskazovskaya**, T. T. Luu, M. K. Trubetskov, E. Goulielmakis, and V. Pervak, "Nonlinear behavior and damage of dispersive multilayer optical coatings induced by two-photon absorption," (2014), SPIE Proceedings p. 92370L.
- T. Paasch-Colberg, A. Schiffrin, N. Karpowicz, S. Kruchinin, Saglam, S. Keiber, **O. Razskazovskaya**, S. Mühlbrandt, A. Alnaser, M. Kübel, V. Apalkov, D. Gerster, J. Reichert, T. Wittmann, J. V. Barth, M. I. Stockman, R. Ernstorfer, V. S. Yakovlev, R. Kienberger, and F. Krausz, "Solid–state lightphase detector," Nature Photonics 8, 214–218 (2014).
- V. Pervak, **O. Razskazovskaya**, I. B. Angelov, K. L. Vodopyanov, and M. Trubetskov, "Dispersive mirror technology for ultrafast lasers in the range 220–4500 nm," Advanced Optical Technologies 3 (2014).

- ▷ • T. V. Amotchkina, M. K. Trubetskov, A. V. Tikhonravov, V. Janicki, J. Sancho-Parramon, **O. Razskazovskaya**, and V. Pervak, "Oscillations in spectral behavior of total losses (1 – R – T) in thin dielectric films," Optics express 20, 16129–16144 (2012).
- Pervak, V., Pronin, O., **Razskazovskaya, O.**, Brons, J., Angelov, I. B., Trubetskov, M. K., Tikhonravov, A. V. and Krausz, F., High-dispersive mirrors for high power applications," Optics express 20, 4503–4508 (2012).

## CONFERENCES

- ▷ • "Nonlinear behavior and damage of dispersive multilayer optical coatings induced by two-photon absorption", oral presentation, SPIE Laser Damage 2014, Boulder, CO, September 2014.
- "Efficient broadband highly dispersive HfO<sub>2</sub>/SiO<sub>2</sub> multilayer mirror for pulse compression in near ultraviolet," poster presentation, XVIII Ultrafast Phenomena 2012, Lausanne, Switzerland, July 2012.

## TRAINING

- ▷ Summer schools
  - Summer School of Ultrafast Laser Science and Applications, Menorca, Spain, June 2012.
  - Summer School New Frontiers in Optical Technologies, Tampere, Finland, August 2015.

## AWARDS

- ▷ • Best Oral presentation "Nonlinear behavior and damage of dispersive multilayer optical coatings induced by two-photon absorption", SPIE Laser Damage 2014.

## JOBS

- ▷ Period 2009–2010
  - Employer **Coherent Inc.**, Santa Clara / USA
  - Employment Internship
  - Main responsibilities Development of Nd:YLF high-power solid-state oscillators of Evolution family
- ▷ Period 2008–2009
  - Employer **Laser export Ltd.**, Moscow / Russia
  - Employment R&D engineer
  - Main responsibilities Development of Nd:YLF solid-state oscillators for biomedical and microscopy applications

## LANGUAGES

FIRST LANGUAGE  
OTHER LANGUAGES

**Russian**

English – C2 • German–B2 • French - A1.1

## ABILITIES

SOCIAL SKILLS

Sociable and outgoing intravert

HOBBIES

Snowboarding • Hiking • All things hand-made

Neuchâtel, Switzerland, February 13, 2018